Clustering and Lagrangian Statistics of Bubbles

Julián Martínez Mercado

Samenstelling promotiecommissie:

Prof. dr. Gerard van der Steenhoven (voorzitter)	Universiteit Twente
Prof. dr. Detlef Lohse (promotor)	Universiteit Twente
dr. Chao Sun (assistent promotor)	Universiteit Twente
Prof. dr. it. Theo van der Meer	Universiteit Twente
Prof. dr. Martin van Sint Annaland	Technische Universiteit Eindhoven
Prof. dr. Herman Clercx	Technische Universiteit Eindhoven
Prof. dr. Frédéric Risso	Institute de Mécanique des Fluides, Toulouse
Prof. dr. Roberto Zenit Camacho	National Autonomous University of Mexico.

The work in this thesis was carried out at the Physics of Fluids group of the Faculty of Science and Technology of the University of Twente. It is part of the industrial partnership programme: *Fundamentals of heterogeneous bubbly flows* of the Foundation for Fundamental Research on Matter (FOM) and the industrial partners AkzoNobel, DSM, Shell, Tata Steel. FOM is financially supported by the Dutch Organization for Scientific Research (NWO), .

Nederlandse titel:
Clusteren en Lagrangiaanse Statistieken van Bellen

Publisher:
Julián Martínez Mercado, Physics of Fluids, University of Twente,
P.O. Box 217, 7500 AE Enschede, The Netherlands
pof.tnw.utwente.nl

Cover design: Julián Martínez Mercado
Print: Gildeprint, Enschede.

ISBN: 978-90-365-3220-4

CLUSTERING AND LAGRANGIAN STATISTICS OF BUBBLES

PROEFSCHRIFT

ter verkrijging van
de graad van doctor aan de Universiteit Twente,
op gezag van de rector magnificus,
Prof. dr. H. Brinksma,
volgens besluit van het College voor Promoties
in het openbaar te verdedigen
op vrijdag 15 Juli 2011 om 16.45 uur

door

Julián Martínez Mercado
geboren op 27.10.1979
te Mexico-Stad

Dit proefschrift is goedgekeurd door de promotor:

Prof. dr. rer. nat. Detlef Lohse

en de assistent-promotor:

Dr. Chao Sun

There is an expanding frontier of ignorance...
...things must be learned only to be
unlearned again or, more likely, to be corrected.
R.P. Feynman

The mistake we made was in thinking
that the earth belonged to us,
when the fact of the matter is
that we are the ones who belong to the earth.
Nicanor Parra.

A mis padres,
el origen de mis días.
A Gaby y a Edgar,
a Matías.

Contents

1

Introduction

If someone asks to give examples of flows that come automatically to the mind, there is a high probability that the answers would be either flows that appear in nature (e.g. the flow of a river, the flow of air in the atmosphere, the oceanic currents) or flows that occur at home (e.g. the jet of water coming out from the tap).

The first type of flows have common characteristics. They are multi-phase — it is not only a single fluid but a mixture of phases (gas-liquid-solid) — and they are turbulent — they are “random” flows. Multiphase turbulent flows are omnipresent in nature (e.g. hurricanes, sediments transported by a river, cloud formation), and in industry (e.g. bubble columns in the chemical and petrochemical industries). This work focuses on a particular case of multiphase flows: bubbly flows, and studies them in two different flow conditions:

- In the first one, the liquid is quiescent and bubbles rise due to buoyancy inducing agitation to the liquid phase.
- In the second one, micro-bubbles are dispersed in a homogeneous isotropic turbulent flow, and they interact with the turbulent structures.

1.1 Turbulence

Turbulence refers to the disordered, irregular, random and to some extent unpredictable motion of fluids. A definition of turbulence is much more easier if we list the main characteristics of these type of flows:

- It is random in time and space. The state of a turbulent flow (i.e. the velocity, pressure, and temperature fields) can not be predicted as for the laminar case.

- It is a multi-scale phenomenon. Eddies with different length- and timescales interact closely with each other. The higher the turbulence, the wider the range of sizes of co-existing eddies.

- It is highly dissipative. Without an external energy input, dissipative effects would laminarise the turbulence.

- It is intermittent. Strong non-Gaussian fluctuations occur more often than for a Gaussian statistical process. Consequently, the probability of these rare violent events are higher and increases as the flow becomes more turbulent [1].

Although turbulent flows are daily phenomena occurring everywhere (e.g. the flow surrounding a car, the motion of the atmosphere, water flowing inside a pipe, the smoke of a cigarette), scientists started to study them thoroughly just in the last two hundred years. The reason for the "late" start of turbulent research is its inherent complexity. Even today, as Feynman pointed out [2], turbulence still remains an unresolved problem in classical physics.

Turbulence is mathematically described with the Navier-Stokes equations, but until now there is not a complete theory to describe turbulence yet [3]. However, big steps towards its understanding have been taken. In 1822, Osborne Reynolds carried out experiments to determine the conditions at which laminar flows in a pipe become turbulent, and showed that the different regimes (either laminar or turbulent) are determined by the value of a dimensionless quantity (nowadays the Reynolds number):

$$Re = VD/\nu,$$

where V is the fluid velocity, D the diameter of the pipe, and ν the kinematic viscosity of the fluid.

He also proposed to study turbulent flows from a statistical point of view, by decomposing the velocity $\mathbf{V}$ into the sum of the mean $\mathbf{U}$ and a fluctuating part $\mathbf{u}$. This decomposition into a mean motion and the fluctuation was already contemplated some centuries before by Leonardo da Vinci. He described in one of his drawings a turbulent stream resembling the way hair falls (mean motion) and its curls (fluctuations), see his notes *On hair falling down in curls* in [4].

But it was until the last century when the conceptual framework of modern turbulence was introduced by Andreii Kolmogorov [5, 6](known nowadays as K41 theory). Some years before, in 1922, Richardson envisioned a qualitative description of how the energy is transferred in turbulence. He proposed that the largest eddies, of size similar to that of the system, break up into smaller eddies, which once again break up into even smaller ones. The break up mechanism repeats successively until a critical, sufficiently small, Re is reached. At these scales, the smallest eddies are stable and they are dissipated by viscosity. Hence, an energy cascade takes place where the energy is transferred down from large to small scales.

Following Richardson's idea Kolmogorov assumed that in flows with high Re, the large scale anisotropy can eventually vanish at sufficient small scales as a result of the energy cascade mechanism. At these small scales turbulence is thus statistically homogenous and isotropic, and it is only determined by the mean flux of energy $\langle\varepsilon\rangle$, yielding to an universal state independent of how it was generated. The range of scales where this universal regime holds is called inertial subrange. At the smallest scales viscosity effects become important and dissipation is the dominant mechanism. This final stage of the cascade is called the dissipation range and is determined by the fluid viscosity ν and $\langle\varepsilon\rangle$.

1.2 Pseudo-turbulence

Before considering the movement of particles in turbulence, we focus on a simpler system: particles either rising or falling in a liquid at rest. In this case, the particle motion is the only energy input, and liquid fluctuations are induced. The nature of these fluctuations is thus different compared to the single-phase shear induced turbulence. These disturbances are mainly a result of the hydrodynamic interactions of the wakes and their heterogenous distribution. This phenomenon is also referred as to pseudo-turbulence, and it is widespread used in the bio- and petrochemical industries to enhance mixing, mass and heat transfer. Bubble columns fall within this category.

Several scientific research has been carried out to understand the nature of the induced agitation [7–11]. The characteristics of the induced fluctuations are reflected in their energy spectrum, and actually it still remains an open question. The results on energy spectrum on pseudo-turbulence have been contradictory [see e.g. 9]. Lance *et al.* [12] were the first that reported a $-8/3$ scaling of the energy spectrum of liquid fluctuations in bubbly flows, but there are some other investigations that have measured the typical turbulent power law decay of $-5/3$ in pseudo-turbulence [13].

In this work, we study further this issue by performing experiments using a novel technique phase-sensitive constant-temperature anemometry (CTA), which allows the direct detection of the bubble collisions onto the hot-film probe. Discarding the bubble information in the time-series of the CTA measurements is crucial for the determination of the spectrum of liquid fluctuations, and provides a reliable result.

Additionally we are also interested in studying the statistics of the bubble velocity and bubble clustering in pseudo-turbulence. To achieve this, we implement a three-dimensional particle tracking velocimetry (PTV) system to obtain experimentally the position and velocity of bubbles. One major advantage of this technique is its non-intrusiveness. On the other hand, it is limited to dilute bubbly systems where single bubbles can be detected and they are not merged as two-dimensional blobs.

Previous experimental works on the clustering of bubbles in pseudo-turbulence [11] have stdueid it by either analyzing two-dimensional images or by looking at time-series of the bubble collisions obtained by optical or hot-film probes [14, 15]. Three-dimensional information of the bubble position is fundamental for a correct quantification of the clustering. Direct numerical simulations (DNS) can provide such detailed information, but with some limitations like the number of simulated bubbles and the imposed periodic boundary conditions in order to reduce the simulation time [7, 16].

Probability density functions (PDFs) of bubble velocities provide important information for effective force correlations which are used in bubbly flow models in industry. Experimental PDFs of bubble velocity have been measured using intrusive techniques such as impedance probes [11, 17]. As this technique relies on the bubble collision, the number of data points used for the PDFs is not sufficient for obtaining well-converged statistics.

By employing three-dimensional PTV, we report for the first time on experimental well-converged PDFs of bubble velocities and clustering.

1.3 Bubbles in turbulence and clustering

The turbulent flows that are found in daily experience are not as ‘simple’ as the ideal homogeneous isotropic turbulence though. For instance they can transport particles, thus increasing their complexity. Most of the times the particles behave differently as fluid tracers as they have finite sizes and their densities can be different from that of the carrier fluid. Our understanding of the dynamics of particles (light, neutral or heavy) in turbulent flows is far from complete. However, in recent years results of numerical and experimental investigations have enormously contributed to its understanding . Particularly, Lagrangian studies—an ideal approach due to the inherent mixing and transport characteristics of turbulence—have attracted much attention [18]. The challenge and big interest to comprehend more the Lagrangian statistics remains, e.g. Do these statistics also exhibit a K41 scaling? How intermittent are they? Moreover, how do these statistics depend on particle size and density? There are numerous studies that have dealt with fluid and heavy particles in turbulence [19–21]. In contrast, there is little experimental research for bubbles (light particles) [22, 23].

Another important issue in turbulent multi-phase flows is clustering. The dispersion of particles within a flow is a result of the hydrodynamic interactions of particles with the flow structures (e.g. eddies). Particles with a different density and size to those of the carrier fluid distribute inhomogeneously. This phenomenon is known as preferential concentration or inertial clustering. The study of inertial clustering is of big interest as the particles' distribution plays an important role in numerous phenomena (e.g. drop formation and break up in cloud dynamics [24], in the interaction of plankton species [25], combustion etc.). There are several mathematical tools available for quantifying clustering, ranging from pair correlation [26], counting box methods [27], Lyapunov exponents [28], Voronoï diagrams [29] or Minkowski functionals[30].

In the present work, we study experimentally the Lagrangian statistics of microbubbles in homogeneous isotropic turbulence and its clustering. We employ also three-dimensional PTV to obtain the position, velocity and acceleration of microbubbles in a turbulent flow. Probability Density Functions of bubble velocity and acceleration as well as their autocorrelation functions are calculated. We compare the bubbles statistics with the cases of neutral and heavy particles. Clustering effect of bubbles in turbulence are investigated using a Voronoï analysis.

1.4 A guide through this thesis

The first part of this thesis is dedicated to bubbly pseudo-turbulence, where bubbles with diameters $d_b \approx$ 4-5 mm are injected in the Twente Water Tunnel. In chapter 2, the experimental results of the energy spectra of liquid fluctuations, the velocity statistics of bubbles and the bubble clustering are reported. To accomplish this, we use novel experimental techniques, such as three-dimensional PTV and phase-sensitive CTA. We explain the details of both techniques together with the advantages and disadvantages when used in bubbly flows. We also compare in chapter 3 the results of front-tracking DNS with experiments, and investigate further the power law scaling of the energy spectrum and the PDFs of bubble velocities. The big advantage of front-tracking simulations is that the bubble-liquid interface is resolved accounting for bubble wake phenomena. Here we show that a different $-5/3$ scaling of the energy spectrum in bubbly pseudo-turbulence indeed exists, and that wake phenomena produce it.

The second part of the thesis addresses the motion of micro-bubbles in homogeneous isotropic turbulence. Experiments with micro-bubbles are carried out in the turbulent Twente Water Tunnel. Micro-bubbles with size similar to the turbulent Kolmogorov's lengthscale τ_η are dispersed and advected by the mean flow. A three-dimensional PTV system allow us to obtain the micro-bubbles' positions. By means of a tracking algorithm, the micro-bubble trajectories are reconstructed, allowing us to obtain micro-bubble velocity and acceleration along the trajectories. In chapter 4, we discuss the Lagrangian statistics of micro-bubbles. We show that the micro-bubble velocity PDFs of all components have a Gaussian distribution, whereas the PDFs of micro-bubble acceleration exhibit high intermittent tails. Details on the analysis method are given. Similarities and differences of the Lagrangian statistics of micro-bubbles, heavy particles and tracers are commented. Finally, in chapter 5 the clustering behavior of heavy, neutral and light particles is studied applying a Voronoï approach. Both, experimental data and point-particle DNS are used for this analysis. We show that Voronoï diagrams can be used to quantify the clustering of particles, with the standard deviation of the normalized Voronoï volumes as an indicator of clustering. Furthermore, we study the temporal evolution of the Voronoï cells in a Lagrangian manner. The summary and conclusions of our work are given in chapter 6, followed with an outlook for future work.

References

[1] S. Pope, *Turbulent flows*, first edition (Cambridge University Press) (2000).

[2] R. Feynman, L. R.B., and M. Sands, *The Feynman lectures on physics, Vol. 1* (Addison-Wesley) (1963).

[3] L. Landau and E. Lifshitz, *Fluid Mechanics*, volume 6, second edition (Butterworth Heinemann) (2000).

[4] Project Gutenberg, "The notebooks of Leonardo da Vinci-Complete", Website (2011), `http://www.gutenberg.org/cache/epub/5000/pg5000.html`.

[5] A. Kolmogorov, "The local structure of turbulence in incompressible viscous fluid for very large Reynolds number", Proc. R. Soc. Lond. A **434**, 9–13 (1991).

[6] A. Kolmogorov, "Dissipation of energy in the locally isotropic turbulence", Proc. R. Soc. Lond. A **434**, 15–17 (1991).

[7] B. Bunner and G. Tryggvason, "Dynamics of homogeneous bubbly flows. Part 1. Rise velocity and microstructure of the bubbles", J. Fluid Mech. **466**, 17–52 (2002).

[8] F. Risso and K. Ellingsen, "Velocity fluctuations in a homogeneous dilute dispersion of high-Reynolds-number rising bubbles", J. Fluid Mech. **453**, 395–410 (2002).

[9] J. Rensen, S. Luther, and D. Lohse, "The effects of bubbles on developed turbulence", J. Fluid Mech. **538**, 153–187 (2005).

[10] W. Dijkhuizen, I. Roghair, M. Van Sint Annaland, and J. Kuipers, “DNS of gas bubbles behaviour using an improved 3D front tracking model–drag force on isolated bubbles and comparison with experiments”, Chem. Eng. Sci. **65**, 1415–1426 (2010).

[11] R. Zenit, D. Koch, and A. Sangani, “Measurements of the average properties of a suspension of bubbles rising in a vertical channel”, J. Fluid Mech. **429**, 307–342 (2001).

[12] M. Lance and J. Bataille, “Turbulence in the liquid phase of a uniform bubbly air–water flow”, J. Fluid Mech. **222**, 95–118 (1991).

[13] R. Mudde, J. Groen, and H. van der Akker, “Liquid velocity field in a bubble column: LDA experiments”, Chem. Eng. Sci. **52**, 4217 (1997).

[14] A. Cartellier and N. Rivière, “Bubble-induced agitation and microstructure in uniform bubbly flows at small to moderate particle Reynolds number”, Phys. Fluids **13** (2001).

[15] E. Calzavarini, T. van der Berg, F. Toschi, and D. Lohse, “Quantifying microbubble clustering in turbulent flow from single-point measurements”, Phys. Fluids **20**, 040702 (2008).

[16] A. Esmaeeli and G. Tryggvason, “A direct numerical simulation study of the buoyant rise of bubbles at O(100) Reynolds number”, Phys. Fluids **17**, 093303 (2005).

[17] J. Martínez Mercado, C. Palacios Morales, and R. Zenit, “Measurements of pseudoturbulence intensity in monodispersed bubbly liquids for $10<\mathrm{Re}<500$”, Phys. Fluids **19**, 103302 (2007).

[18] F. Toschi and E. Bodenschatz, “Lagrangian properties of particles in turbulence”, Annu. Rev. Fluid Mech. **41**, 375–404 (2009).

[19] G. Voth, A. La Porta, A. M. Crawford, J. Alexander, and E. Bodenschatz, “Measurement of particle accelerations in fully developed turbulence”, J. Fluid Mech. **469**, 121–160 (2002).

[20] N. Mordant, A. M. Crawford, and E. Bodenschatz, “Experimental lagrangian acceleration probability density function measurement”, Physica D **193**, 245–251 (2004).

[21] L. Biferale, G. Boffetta, A. Celani, B. J. Devenish, A. Lanotte, and F. Toschi, “Multifractal statistics of lagrangian velocity and acceleration in turbulence”, Phys. Rev. Lett. **93**, 064502 (2004).

[22] R. Volk, E. Calzavarini, G. Verhille, D. Lohse, N. Mordant, J.-F. Pinton, and F. Toschi, “Acceleration of heavy and light particles in turbulence: Comparison between experiments and direct numerical simulations”, Physica D **237**, 2084 – 2089 (2008).

[23] R. Volk, N. Mordant, G. Verhille, and J.-F. Pinton, “Laser doppler measurement of inertial particle and bubble accelerations in turbulence”, EPL **81**, 34002 (2008).

[24] E. Bodenschatz, S. P. Malinowski, R. A. Shaw, and F. Stratmann, “Can we understand clouds without turbulence?”, Science **327**, 970–971 (2010).

[25] F. Schmitt and L. Seuront, “Intermittent turbulence and copepod dynamics: increase in encounter rates through preferential concentration”, J. Mar. Syst. **70**, 263–272 (2008).

[26] E. Saw, R. Shaw, S. Ayyalasomayajula, P. Chuang, and A. Gylfason, “Inertial clustering of particles in high-Reynolds-number turbulence”, Phys. Rev. Lett. **100**, 214501 (2008).

[27] A. Aliseda, A. Cartellier, F. Hainaus, and J. Lasheras, “Effect of preferential concentration on the settling velocity of heavy particles in homogeneous isotropic turbulence”, J. Fluid Mech. **468**, 77–105 (2002).

[28] J. Bec, L. Biferale, G. Boffetta, M. Cencini, S. Musacchio, and F. Toschi, “Lyapunov exponents of heavy particles in turbulence”, Phys. Fluids **18**, 091702 (2006).

[29] R. Monchaux, M. Bourgoin, and A. Cartellier, “Preferential concentration of heavy particles: A voronoi analysis”, Phys. Fluids **22**, 103304 (2010).

[30] E. Calzavarini, M. Kerscher, D. Lohse, and F. Toschi, “Dimensionality and morphology of particle and bubble clusters in turbulent flow”, J. Fluid Mech. **607**, 13–24 (2008).

2

Bubble clustering and energy spectra in pseudo-turbulence [*]

Three-dimensional particle tracking velocimetry (PTV) and phase-sensitive constant temperature anemometry in pseudo-turbulence—i.e. flow solely driven by rising bubbles— were performed to investigate bubble clustering and to obtain the mean bubble rise velocity, distributions of bubble velocities, and energy spectra at dilute gas concentrations ($\alpha \leq 2.2\%$). To characterize the clustering the pair correlation function $G(r, \theta)$ was calculated. The deformable bubbles with equivalent bubble diameter $d_b = 4 - 5$ mm were found to cluster within a radial distance of a few bubble radii with a preferred vertical orientation. This vertical alignment was present at both small and large scales. For small distances also some horizontal clustering was found. The large number of data-points and the non intrusiveness of PTV allowed to obtain well-converged Probability Density Functions (PDFs) of the bubble velocity. The PDFs had a non-Gaussian form for all velocity components and intermittency effects could be observed. The energy spectrum of the liquid velocity fluctuations decayed with a power law of -3.2, different from the $\approx -5/3$ found for homogeneous isotropic turbulence, but close to the prediction -3 by Lance et al. *[1] for pseudo-turbulence.*

---

[*] Published as: J. Martínez Mercado, D. Chehata Gómez, D.P.M. van Gils, C. Sun, and D. Lohse, On bubble clustering and energy spectra in pseudo-turbulence, J. Fluid Mech. **650** 287-306.

2.1 Introduction

Bubbly pseudo-turbulence—i.e. a flow solely driven by rising bubbles—is relevant from an application point of view due to the omnipresence of bubble columns, e.g. in the chemical industry, in water treatment plants, and in the steel industry [2]. A better understanding of the involved phenomena is necessary for scaling-up industrial devices and for optimization and performance prediction. This work wants to provide experimental data on pseudo-turbulence by means of novel experimental techniques. The main questions to be addressed in this chapter are:

(i) What is the preferential range and the orientation of bubble clustering in pseudo-turbulence?

(ii) What is the mean bubble rise velocity and what kind of probability distribution does the bubble velocity have?

(iii) What is the shape of the energy spectrum of pseudo-turbulence?

2.1.1 Bubble clustering

In dispersed flows, the hydrodynamic interaction between the two-phases and the particle inertia result in an inhomogeneous distribution of both particles and bubbles (see e.g. experimentally [3–5] and numerically [6–8] and [9] for a general recent review). Bubble clustering in *pseudo-turbulence* has been studied numerically [10–13] and experimentally [14–17]. The numerical work by Smereka [10] and by Sangani *et al.*[11] and theoretical work by Wijngaarden [18, 19] and Kok [20] suggest that, when assuming potential flow, rising bubbles form horizontally aligned rafts. Three-dimensional direct numerical simulations (DNS), which also solve the motion of the gas-liquid interface at the bubble's surface, have become available in the last few years. The works by Bunner *et al.* [21, 22] suggest that the deformability effect plays a crucial role in determining the orientation of the clustering. For spherical non-deformable bubbles these authors simulated up to 216 bubbles with Reynolds numbers in the range of $12-30$ and void fraction α up to 24%, and Weber number of about 1. For the deformable case, they simulated 27 bubbles with Reynolds number of 26, Weber number of 3.7 and $\alpha = 6\%$. The authors found that the orientation of bubble clusters is strongly influenced by the deformability of the bubbles: spherical pairs of bubbles have a high probability to align horizontally, forming rafts, whereas the non-spherical ones preferentially align in the vertical orientation. In a later investigation, where inertial effects were more pronounced, Esmaeeli *et al.* [23] studied both cases for bubble Reynolds number of order 100. In this case only a weak vertical cluster was observed in a swarm of 14 deformable bubbles. Their explanation for the weaker vertical clustering was that the wobbly bubble motion, enhanced by the larger Reynolds number, produces perturbations which do not allow the bubbles to align vertically and accelerate the break up in case some of them cluster.

In spite of numerous experimental studies on pseudo-turbulence, bubble clustering has not yet been fully quantitatively analysed experimentally. Zenit *et al.* [16] found a mild horizontal clustering using two-dimensional imaging techniques for bubbles with particulate Reynolds number higher than 100. Cartellier *et al.* [14] studied the microstructure of homogeneous bubbly flows for Reynolds number of order 10. They found a moderate horizontal accumulation using pair density measurements with two optical probes. Their results showed a higher probability of the pair density in the horizontal plane and a reduced bubble density behind the wake of a test bubble. Risso *et al.* [15] performed experiments with a swarm of deformable bubbles (d_b=2.5 mm), aspect ratio around 2 and Reynolds number of 800. They did not find clustering and suggested that in this low void fraction regime ($\alpha < 1.05\%$) there was a weak influence of hydrodynamic interaction between bubbles.

2.1.2 Mean bubble rise velocity and statistics of bubble velocity

The mean bubble rise velocity in bubbly flows is found to decrease with increasing bubble concentration whereas the normalized vertical fluctuation $V_{z,rms}/\overline{V}_z$ increases [16, 22, 24]. The interpretation is that when increasing the concentration the bubble-induced counterflow becomes more important and in addition the hydrodynamic interactions between bubbles become more frequent and hinder the upward movement of bubbles, provoking at the same time, an increment of the bubble velocity fluctuations.

Next, Probability Density Functions (PDFs) of bubble velocities provide useful information for effective force correlations used in bubbly flow models in industry. PDFs in pseudo-turbulence have been obtained in the numerical studies of Bunner *et al.* [22, 25] and Esmaeeli *et al.* [23]. For non-deformable bubbles [25], the PDFs of velocity fluctuations have a Gaussian distribution. If deformability is considered [22], the PDF of only one horizontal component of the velocity keeps a Gaussian shape while the non-Gaussianity in the PDFs was stronger at the lowest concentration $\alpha = 2\%$, recovering a Gaussian distribution for $\alpha = 6\%$. However, in that numerical work only a limited number of bubbles ($N_b = 27$) could be considered and the different behavior in the two different horizontal directions reflects the lack of statistical convergence. Experimental PDFs of bubble velocities in pseudo-turbulence have been obtained by Zenit *et al.* [16] and by Martínez *et al.* [24]. In these studies the bubble velocity was measured intrusively using an impedance probe technique. The amount of data points used for the PDFs was not sufficient for good statistical convergence.

2.1.3 Liquid energy spectrum

In bubbly flows, one must distinguish between the energy input due to the bubbles and the energy input due to some external forcing—either of them can be predominant. Lance *et al.* [1] suggested the ratio of the bubble-induced kinetic energy and the kinetic energy of the flow without bubbles as appropriate dimensionless number to characterize the type of the bubbly flow. Rensen *et al.* [26] called this ratio the *bubblance* parameter b, defined as

$$b = \frac{1}{2}\frac{\alpha U_r^2}{u_0'^2}, \tag{2.1}$$

where α was already defined, U_r is the rise bubble velocity in still water, and u_0' is the typical turbulent vertical fluctuation in the absence of bubbles. Lance *et al.* [1] measured the liquid power spectrum in bubbly turbulence and observed a gradual change of the slope with increasing void fraction. At low concentrations the slope of the spectrum was close to the Kolmogorov turbulent value of $-5/3$. By increasing α, the principal driving mechanism changed—the forcing now more and more originated from the bubbles and not from some external driving. In that regime the slope was close to $-8/3$. Having in mind equation (2.1) one may expect different scaling behavior, depending on the nature of the energy input that is dominant, namely $b < 1$ for dominant turbulent fluctuations or $b > 1$ for dominant bubble-induced fluctuations. Indeed from table 1 of Rensen *et al.* [26] one may get the conclusion that the slope is around $-5/3$ for $b < 1$ and around $-8/3$ for $b > 1$. Also Riboux *et al.* [27] obtained a spectral slope of about -3 in the wake of a swarm of rising bubbles in still water ($b = \infty$). Moreover, in numerical simulations Sugiyama *et al.* [12] obtained the same spectral slope for the velocity fluctuations caused by up to 800 rising light particles, i.e. $b = \infty$, with finite diameter ($Re \approx 30$). However, there are also counterexamples: e.g., Mudde *et al.* [28], and Cui *et al.* [29] obtained around $-5/3$, though $b = \infty$. Therefore, in this paper we want to re-examine the issue of the spectral slope in pseudo-turbulence ($b = \infty$).

2.1.4 Outline of the chapter

This chapter is structured as follows: in section 2.2 the experimental apparatus is explained and particle tracking velocimetry technique, (PTV) and phase-sensitive constant temperature anemometry (CTA) are described. Section 2.3 is divided in three subsections: in the first part results on bubble clustering are shown, followed by the results on the mean bubble rise velocity and the bubble velocity distributions, and finally the power spectrum measurements are presented. A summary and an outlook on future work are presented in section 2.4.

Table 2.1: Typical experimental parameters: void fraction α, mean bubble diameter ($d_b = \sqrt[3]{d_l^2 d_s}$), where d_l and d_s are the long and short axes of a two-dimensional image of a given ellipsoidal bubble, mean rising velocity in still water $\overline{V}_z$, and Reynolds ($Re = d_b\overline{V}_z/\nu_f$), Weber ($We = \rho d_b \overline{V}_z^2/\sigma$), and Eötvos ($Eo = \rho_f g d_b^2/\sigma$) numbers. Here $\nu_f = 1\times10^{-6}\ m^2/s$ is the kinematic viscosity of water, $\sigma = 0.072\ N/m$ the surface tension at the air-water interface, and g the gravitational acceleration.

α(%)	d_b(mm)	$\overline{V}_z$(m/s)	Re	We	Eo
$0.28-0.74$	$4-5$	$0.16-0.22$	1000	$2-3$	$3-4$

2.2 Setup, tools, and methods

2.2.1 Twente water channel

The experimental apparatus consists of a vertical water tunnel with a 2 m long measurement section with 0.45 × 0.45 m^2 cross section. A sketch depicting the setup is shown in figure 2.1. The measurement section has three glass walls for optical access and illumination (see [26] for more details). The channel was filled with deionized water to the top of the measurement section. The level of the liquid column was 3.8 m above the place where bubbles were injected. We used three capillary islands in the lowest part of the channel to generate bubbles. Each island contains 69 capillaries with an inner diameter of 500 μm. Different bubble concentrations were achieved by varying the air flow through the capillary islands. We performed experiments with dilute bubbly flows with typical void fractions in the range $0.28\% \leq \alpha \leq 0.74\%$ for PTV and in the range $0.20\% \leq \alpha \leq 2.2\%$ for CTA. The void fraction α was determined using a U-tube manometer which measures the pressure difference between two points at different heights of the measurement section [see 26]. A mono-dispersed bubbly swarm with mean bubble diameter of $4-5$ mm was studied. Typical Reynolds numbers Re are of the order 10^3, the Weber number We is in the range $2-3$ (implying deformable bubbles) and the Eötvos number Eo is around $3-4$. Table 2.1 defines these various dimensionless numbers and summarizes the experimental conditions. In figure 2.2, the mean bubble diameter d_{eq} as a function of void fraction is shown. The values are within the range of 4-5 mm and show a slight increment with bubble concentration.

2.2.2 Particle Tracking Velocimetry

In the last few years three-dimensional PTV has become a powerful measurement technique in fluid mechanics. The rapid development of high-speed imaging has enabled a successful implementation of the technique in studies on turbulent motion

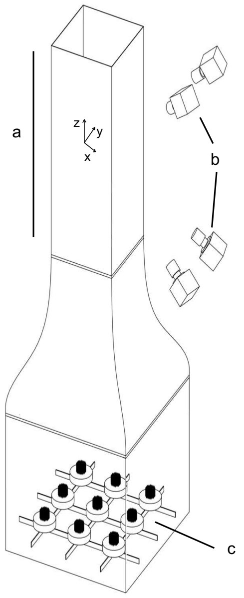

Figure 2.1: Experimental apparatus: a) Measurement section of length 2m, b) 4-camera PTV system, c) Capillary islands.

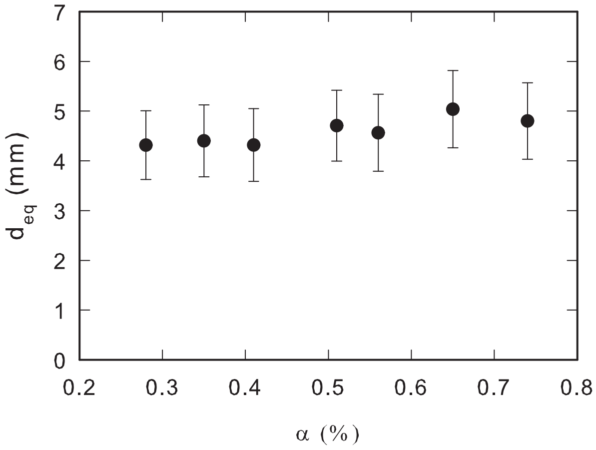

Figure 2.2: Equivalent bubble diameter d_{eq} as a function of void fraction α. Standard deviation as error bars. We measured the long d_l and short d_s axes of 400 bubbles per concentration from two-dimensional images. The equivalent diameter was obtained by assuming ellipsoidal bubbles with a volume equal to that of a spherical bubble, $d_{eq} = (d_s d_l^2)^{1/3}$

of particles [9, 30–34]. The measured three-dimensional spatial position of particles and time trajectories allow for a Lagrangian description which is the natural approach for transport mechanisms.

Figure 2.1 also sketches the positions of the four high-speed cameras (Photron 1024-PCI) which were used to image the bubbly flow. The four cameras were viewing from one side of the water channel and were focused in its central region, at a height of 2.8 m above the capillary islands. Lenses with 50 mm focal length were attached to the cameras. We had a depth of field of 6 cm. The image sampling frequency was 1000 Hz using a camera resolution of 1024×1024 pixel^2. The cameras were triggered externally in order to achieve a fully synchronized acquisition. We used the PTV software developed at IfU-ETH [35] for camera calibration and tracking algorithms. For a detailed description of this technique we refer to [35] and references therein. A three-dimensional solid target was used for calibration. Bubbles were detected within a volume of $16\times16\times6$ cm^3 with an accuracy of 400 μm. To illuminate the measuring volume, homogeneous back-light and a diffusive plate were used in order to get the bubble's contour imaged as a dark shadow. The image sequence was binarized after subtracting a sequence-averaged background; then these images were used along with the PTV software to get the three-dimensional positions of the bubbles. We acquired 6400 images per camera corresponding to 6.4 s of measurement (6.7 Gbyte image files).

For higher bubble concentration, many bubbles are imaged as merged blobs and can not be identified as individual objects. These merged bubbles images are not considered for the analysis. Therefore the number N_b of clearly identified individual bubbles goes down with increasing void fraction. For the most dilute case ($\alpha =$ 0.28%) around $N_b \approx 190$ bubbles were detected in each image. This quantity dropped to nearly 100 for the most concentrated cases ($\alpha = 0.65\%$ and $\alpha = 0.74\%$). If a bubble is tracked in at least 3 consecutive time-steps, we call it a linked bubble. Table 2.2 summarizes typical values of number of bubbles (N_b) and linked bubbles (N_{link}) per image.

2.2.3 Pair correlation function

Particle clustering can be quantified using different mathematical tools like pair correlation functions [21], Lyapunov exponents [36], Minkowski functionals [7], or PDFs of the distance of two consecutive bubbles in a time-series [6]. In this investigation the pair correlation function $G(r,\theta)$ is employed to understand how the bubbles are globally distributed. It is defined as follows:

$$G(r,\theta) = \frac{V}{N_b(N_b-1)}\left\langle \sum_{i=1}^{N_b} \sum_{j=1,i\neq j}^{N_b} \delta(\mathbf{r}-\mathbf{r}_{ij}) \right\rangle, \tag{2.2}$$

Table 2.2: Number of detected bubbles and linked bubbles per image for all concentration studied. For the highest void fractions there is a drop in the number of linked bubbles, since most bubbles are imaged as two-dimensional merged blobs, which are not considered in the analysis.

α	N_b	N_{link}	$N_{link}/N_b \cdot 100\%$
0.28%	≈190	≈50	27%
0.35%	≈190	≈50	27%
0.41%	≈170	≈40	24%
0.51%	≈140	≈30	21%
0.56%	≈140	≈30	21%
0.65%	≈110	≈20	18%
0.74%	≈110	≈15	14%

where V is the size of the calibrated volume, N_b is the number of bubbles within that volume, $\mathbf{r}_{ij}$ is the vector linking the centers of bubble i and bubble j, and $\mathbf{r}$ is a vector with magnitude r and orientation θ, defined as the angle between the vertical unit vector and the vector linking the centers of bubbles i and j, as shown in figure 2.3. From (2.2), the radial and angular pair probability functions can be derived. To obtain the radial pair probability distribution function $G(r)$ one must integrate over spherical shells of radius r and width Δr, whereas for the angular pair probability distribution function $G(\theta)$ an r-integration is performed.

We also checked that our numerical scripts for calculating the pair correlation function give $G(r) = 1$ and $G(\theta) = 1$ for a random distribution of particles. Therefore, we generated randomly positions of particles and applied the script to calculate both radial and angular correlations. We considered 2 sets of particles. Case A with a total number of particles $np_A = 1000$ at 100 'timesteps' $ts_A = 100$ and case B, where both the total number of particles and the number of 'timesteps' are closer to our experimental conditions $np_B = 500$ and $ts_B = 6000$. We applied the script to these two sets. Figure 2.4 shows the radial and angular correlation function for both sets. As we can see the functions reach a value of nearly 1 as it is expected for a randomly distributed set of particles.

2.2.4 Phase-sensitive constant-temperature anemometry

Hot-film measurements in bubbly flows impose considerable difficulty due to the fact that liquid and gas information is present in the signal. The challenge is to distinguish and classify the signal corresponding to each phase. The hot-film probe does not provide by itself means for a successful identification. Thus many parametric and non-parametric signal processing algorithms have been used to separate the informa-

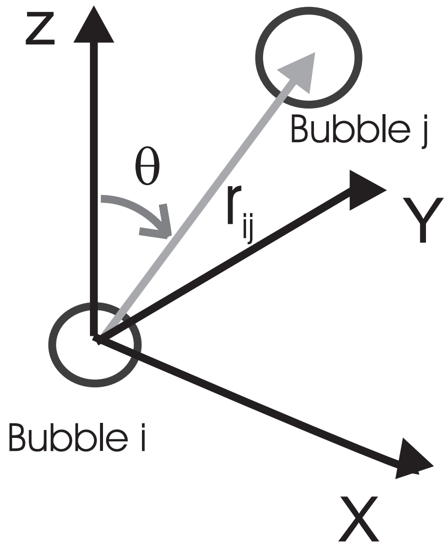

Figure 2.3: Definition of angle θ between a pair of neighboring bubbles.

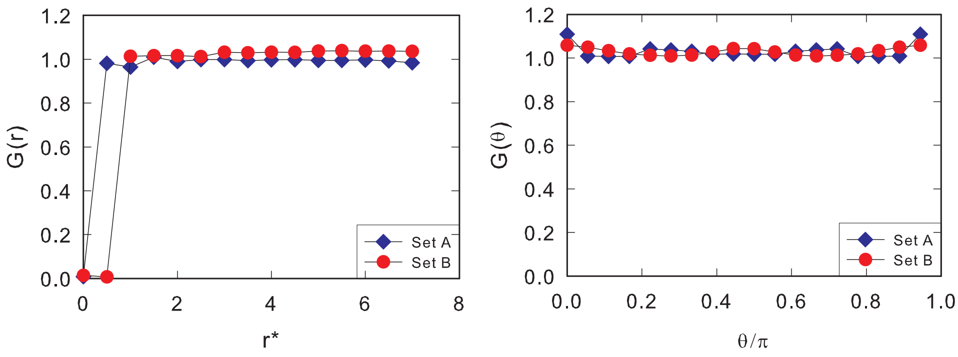

Figure 2.4: Radial and angular pair correlation for the two sets of randomly distributed particles. Set A: 1000 particles and 100 'time-steps', Set B: 500 particles and 6000 'time-steps'. In figure (a) $G(r) > 0$ for $r^* < 1$ in set A because the 'separation' between particle was less than the separation distance in set B which was used for both normalizations.

tion of both phases, i.e. thresholding [37] or pattern recognition methods [38]. The output of these algorithms is a constructed indicator function which labels the liquid and gas parts of the signal. We follow an alternative way and *measure* the indicator function, therefore avoiding uncertainties when computing it. This can be achieved by combining optical fibers for phase detection to the hot-film sensor [see 39, 40].

The device, called phase-sensitive CTA, was firstly developed by van den Berg *et al.* [41]. In this technique, an optical fiber is attached close to the hot-film probe so that when a bubble impinges onto the sensor it also interacts with the optical fiber. Its working principle is based on the different index of refraction of gas and liquid. A light source is coupled into the fiber. A photodiode measures the intensity of the light that is reflected from the fiber tip via a fiber coupler. The incident light leaves the tip of the fiber when immersed in water, but it is reflected back into the fiber when exposed to air, implying a sudden rise in the optical signal. Thus the intensity of the reflected light indicates the presence of either gas or liquid at the fiber's tip. In this way, if both signals are acquired simultaneously, the bubble collisions can straightforwardly be detected without the need of any signal-processing method. For the construction of the probe we used a DANTEC cylindrical probe (55R11) and attached two optical fibers to it (Thorlabs NA=0.22 and 200 μm diameter core). We used two fibers in order to assure the detection of all bubbles interacting with the probe. The fibers were glued and positioned at the side of the cylindrical hot-film, at a distance of about 1 mm from the hot-film. An illustration of the hot-film and fibers is shown in figure 2.5. The probe was put in the center of the measurement section positioning its supporting arm parallel to the vertical rising direction of the bubbles so that the axis of the optical probes are also aligned with the preferential direction of the flow, thus allowing for a better bubble-probe interaction and aiming to minimize the slow down of bubbles approaching the probe. Van den Berg *et al.* [41] measured flow velocity with and without the fiber being attached to the probe. They found that the presence of the fibers do not compromise the probe's bandwidth and that its influence on the power spectrum is negligible.

With the signal of each optical fiber a discretized phase indicator function $\xi = \{\xi_i\}_{i=1}^{N}$ can be constructed, whose definition follows [37], namely

$$\xi_i = \begin{cases} 1 & \text{liquid}, \\ 0 & \text{bubble}. \end{cases} \tag{2.3}$$

An unified phase indicator function is then obtained by multiplying the indicator functions of both fibers. A typical signal of phase-sensitive CTA with two consecutive bubble-probe interactions is shown in figure 2.6a. There is one adjustable parameter to construct the indicator functions of the fibers. As explained above the phase discrimination can be done by an intensity threshold of the optical fiber's signal. When the rising edge of the signal surpasses this threshold, the indicator function of the fiber must change from a value 1 to 0, as defined in equation 2.3. If the optical fiber

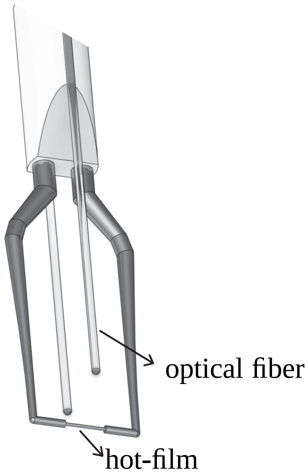

Figure 2.5: Phase Sensitive CTA probe with two attached optical fibers for bubble-probe detection.

was positioned at the same place of the hot-film probe, the rising edge of its signal would occur precisely at the time when the bubble interacts with the hot-film. However, there is a separation of about 1 mm between the fibers and the hot-film, so that the rising edge of the optical fibers' signal occurs actually with some delay. Therefore, to construct the phase indicator function of the optical fibers, one must account for this delay and define the beginning of the interaction not where the signal exceeds the intensity threshold but some time before. The time used for this shifting was obtained considering the vertical separation between the optical fibers and the hot-film probe and mean bubble velocities: in our experiment a bubble travels 1 mm in about 5—7 ms. We shifted the beginning of the collision 8 ms prior to the optical fibers' signal starts to rise from its base value. The shifting value was double checked by analyzing the histograms of the duration of bubble collisions. As it can be observed from figure 2.6b, with this shift sometimes part of the CTA signal when the bubbles is approaching the probe (< 10 ms) was lost, but we noticed no effect on the spectrum when varying the shift duration, provided the bubble spikes were still removed.

With the phase indicator function only pieces containing liquid information of the time series are used for further analysis— i.e. the part of the signal between the two bubble interactions shown in figure 2.6a. For each part of the time-series containing liquid information the spectrum was calculated. Then all spectra were averaged and the power spectrum for each bubble concentration was obtained. In this way neither an interpolation nor auto-regressive models for gapped time series were necessary. In our experiments the gas volume fractions varied from $0.2 \leq \alpha \leq 2.2\%$. The CTA was calibrated using a DANTEC LDA system (57N20 BSA). The calibration curve was

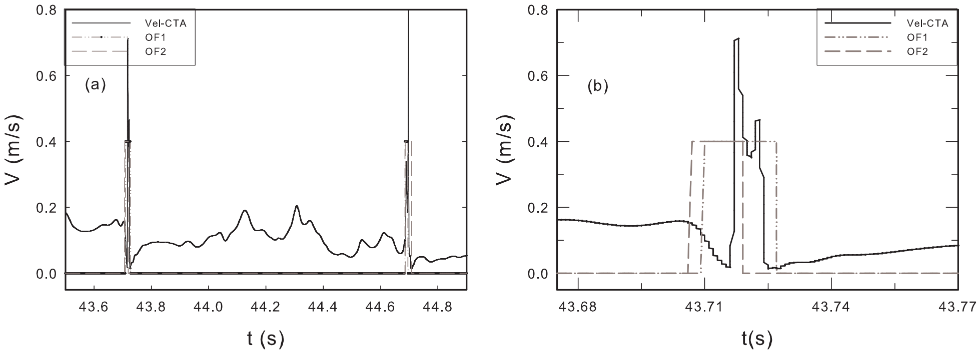

Figure 2.6: Typical phase Sensitive CTA signal already transformed into velocity. (a) two consecutive bubble-probe interactions for α=0.2%, (b) zoom in of a bubble collision.

obtained by fitting the data points to a fourth-order polynomial. The total measuring time was 1 h for each concentration and the sampling rate of the hot-film and optical fibers was 10 kHz.

2.3 Bubble clustering and distributions in pseudo-turbulence

2.3.1 Radial pair correlation

The radial pair correlation $G(r)$ was obtained for all bubble concentrations studied. Figure 2.8 shows $G(r)$ as a function of the normalized radius $r^* = r/a$, where a is a mean bubble radius. As shown in figure 2.2 the mean equivalent bubble diameter is within the range 4-5 mm. Therefore we can normalize with one mean bubble radius and we picked $a = 2$ mm for all concentrations. We observe in figure 2.8 that the highest probability to find a pair of bubbles lies in the range of few bubble radii $r^* \approx 4$ for all concentrations. The probability $G(r)$ of finding a pair of bubbles within this range increases slightly with increasing α. For values $r^* < 2$ one would expect that $G(r) = 0$. However, in our experiments we found $G(r) \neq 0$ for $r^* < 2$, due to the fact that the bubbles are ellipsoidal and deform and wobble when rising.

We now estimate the error bar in the correlation function $G(r)$, originating from incomplete bubble detection, as seen from table 2.2. With increasing α the fraction of detected bubbles decreases. For $\alpha = 0.28\%$ we detect $N_b \approx 200$ so one would expect for α=0.74% to detect $N_b \approx (0.74/0.28) \times 200 \approx 500$ but we are detecting only 110, ≈20% of them. In order to investigate the reliability of the pair correlation function due to this loss of bubble detection, we studied a set of randomly distributed

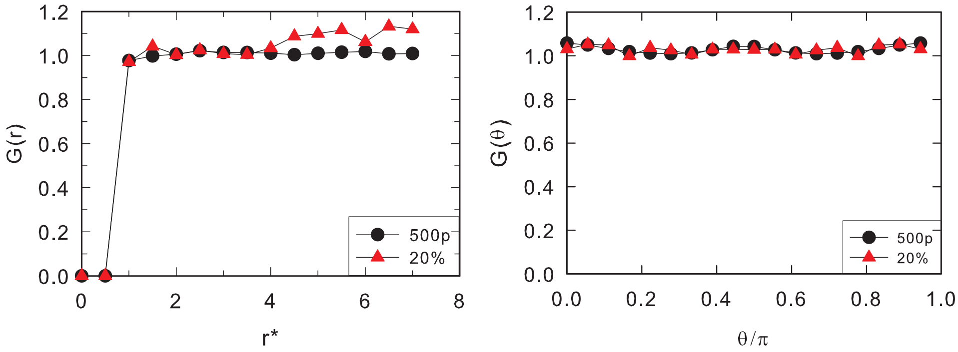

Figure 2.7: Effect of bubble loss detection on the radial and angular pair correlation. (a) $G(r)$ applied to 100%, and 20% of the particles in set B, (b)$G(\theta)$ with $r^* = 5$ applied to 100%, and 20% of the particles in set B .

particles. We generated 500 particles at 6000 timesteps and calculated the radial and angular pair correlation functions, obtaining $G(r) = 1$ and $G(\theta) = 1$ as expected for randomly distributed particles. Then we kept only 20% of the particles and recalculated the correlation functions to see how much they deviate from 1. We found that the maximum deviation was less than 0.1 for both the radial and the angular correlation functions. The results are shown in figures 2.7a and 2.7b for the radial and pair correlations, respectively. This is much smaller than the structure revealed in the $G(r)$ curve in figure 2.8. We therefore consider the clustering with the preferred distance of $r^* = 4$ as a robust feature of our data, in spite of incomplete bubble detection. In figure 2.8 this error bar corresponding to a maximum error of $G(r)$ at the most concentrated flow is also shown.

2.3.2 Angular pair correlation

The orientation of the bubble clustering was studied by means of the angular pair correlation $G(\theta)$ using different radii for the spherical sector over which neighboring bubbles are counted. Figures 2.9(a-c) show the results for r^*=40, 15 and 5, respectively. The plots were normalized so that the area under the curve is unity. For all radii and concentrations, pairs of bubbles cluster in the vertical direction, as one can see from the highest peaks at $\theta/\pi = 0$ and $\theta/\pi = 1$. The value of $\theta/\pi = 0$ means that the reference bubble (at which the spherical sector is centered) rises below the pairing one. For $\theta/\pi = 1$ the reference bubble rises above the pairing bubble (see figure 2.3). When decreasing the radius of the spherical sector, i.e. when probing the short range interactions between the bubbles, we observe that a peak of the angular probability near $\pi/2$ starts to develop. The enhanced probability at this angle range is

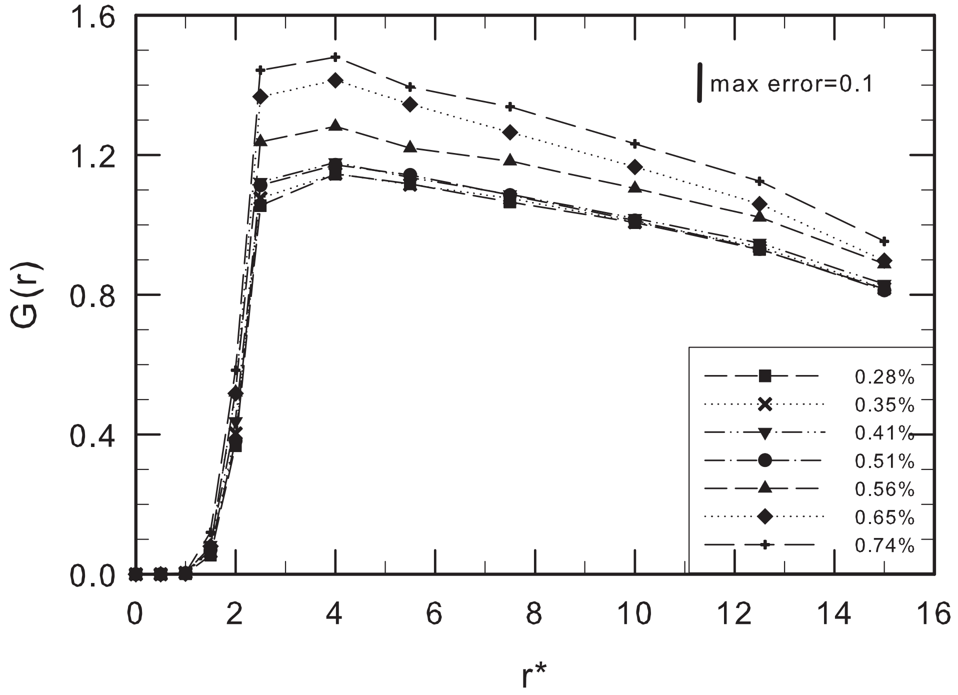

Figure 2.8: Radial pair probability $G(r)$ as a function of dimensionless radius r^*. The different curves are for different bubble volume concentrations α (given in percent).

even more pronounced in figure 2.9c where the peak of $G(\theta)$ for horizontally aligned bubbles is just slightly lower than that for vertical clustering. It is worthwhile to point out that the vertical alignment of the bubbles is very robust and is present from very large to small scales, as the angular correlation for different spherical sectors is always higher at values θ/π=0 and 1 than at value θ/π=0.5. The maximum error bar for the angular correlation for the most concentrated flow at $\alpha = 0.74\%$, when 20% of particles are detected, was 0.1 as explained above and is also shown in figure 2.9. It is much smaller than the structure of the signal.

For comparison, we consider again the work of Bunner *et al.* [22], who found that pairs of bubbles have a higher probability to align vertically, though for a much higher concentration ($\alpha = 6\%$) than employed here. Bunner *et al.* [22] found that the vertical alignment was not as robust as in our case, since with increasing r^* the angular correlation at 0 and π became less dominant. Another significant difference between the findings of our experimental work and their simulations is that horizontal alignment was more pronounced with larger radii of the spherical sector and not when decreasing r^*. Our experimental results clearly show the main drawback and today's limitation when solving the flow at the particle's interface: the simulations are still restricted to a small number of particles, which is not sufficient to reveal long-range correlations.

2.3.3 Interpretation of the clustering

What is the physical explanation for a preferred vertical alignment of pairs of bubbles in pseudo-turbulence? Through potential flow theory, the mutual attraction of rising bubbles can be predicted [42], the application of potential theory to our experiments remains questionable [18], as we are in a statistically stationary situation where bubbles have already created vorticity. Our findings are consistent with the idea that deformability effects and the inversion of the lift force acting on the bubbles are closely related to the clustering. Mazzitelli *et al.* [43] showed numerically that it was mainly the lift force acting on point-like bubbles that makes them drift to the downflow side of a vortex in the bubble wake[†]. Furthermore, when accounting for surface phenomena, Ervin *et al.* [44] showed that the sign of the lift force inverts for the case of deformable bubbles in shear flow so that a trailing bubble is pulled into the wake of a heading bubble rather than expelled from it. In such a manner vertical rafts can be formed. Experimentally some evidence of the lift force inversion has been observed by Tomiyama *et al.* [45] as lateral migration of bubbles under Poiseuille and Couette flow changed once the bubble size has become large enough. Numerical simulations of swarm of deformable bubbles without any flow predicted a vertical alignment [22]. An alternative interpretation of the results, due to Shu Takagi

---

[†] See figure 2 in [43] sketching the dynamics.

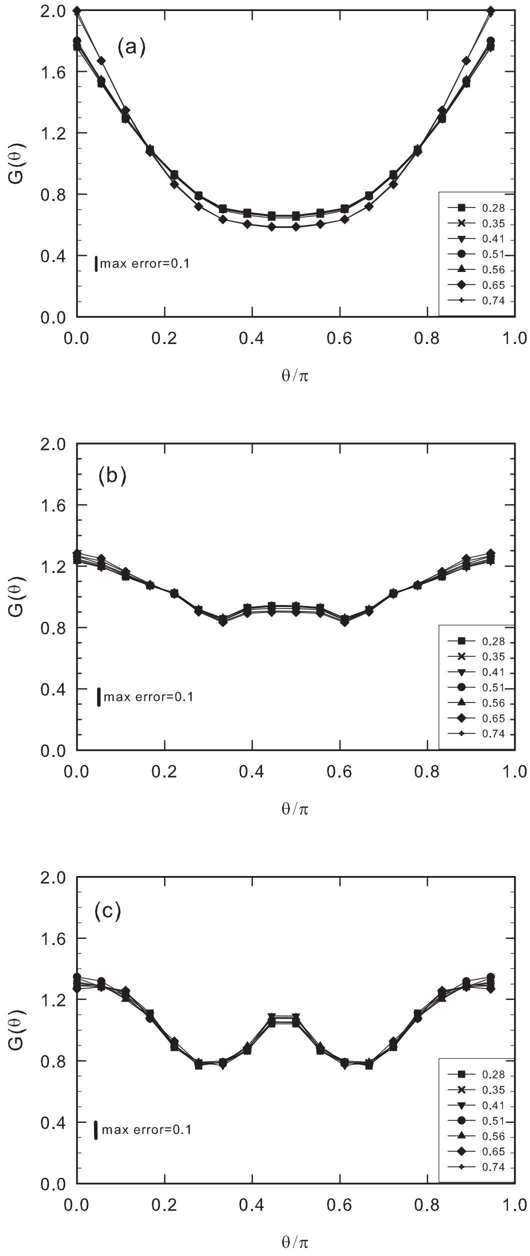

Figure 2.9: Normalized angular pair probability $G(\theta)$ as a function of angular position θ/π for various bubble concentrations α (see insets) and three different bubble-pair distances: (a) $r^* = 40$, (b) $r^* = 15$, and (c) $r^* = 5$. Maximum error bar for the angular correlation of 0.1 at α=0.74%.

(private communication 2009) goes as follows: small, pointwise, spherical bubbles have a small wake, allowing the application of potential flow. The bubbles then horizontally attract, leading to horizontal clustering. In contrast, large bubbles with their pronounced wake entrain neighboring bubbles in their wake due to the smaller pressure present in those flow regions, leading to vertical clustering. Further efforts are needed to identify and confirm the main mechanism—i.e. either lift or pressure reduction in the bubble wake— leading to a preferential vertical alignment, for example through experiments with small, spherical, non-deformable bubbles as achieved by Takagi *et al.* [46] through surfactants or with buoyant spherical particles.

2.3.4 Average bubble rise velocity

Bubble velocities were calculated by tracking the bubble positions which were linked in at least three consecutive images. The mean bubble rise velocity can thus be obtained as a function of the bubble concentration. Figure 2.10 shows the three components of the bubble velocity; the coordinate system corresponds to the one depicted in figure 2.1. The terminal rise velocity of a single bubble with $d_b = 3.9$ mm and with the same water-impurity condition is also shown in figure 2.10, it has a value of 0.26 m s^{-1}. A decrease in the mean bubble rise velocity with concentration is observed in our experiments within the experimental error showed in figure 2.10. The mean bubble rise velocity is 0.22 m s^{-1} for the most dilute case $\alpha = 0.28\%$ and decreases until a value of 0.16 m s^{-1} for $\alpha = 0.51\%$.

The interpretation of this finding is that in this parameter regime the velocity-reducing effect of the bubble-induced counterflow [see 47] and the scattering effect overwhelm the velocity-enhancing blob-effect (originally suggested for sedimenting particles in [48]), implying that a blob of rising bubbles rises faster than a single one. For values of $\alpha \geq 0.56\%$ the mean values are again larger, around 0.18 m s^{-1}. This increment of the mean rise velocity could be a result of our experimental error. As mentioned in section 2.2.2, the number of detected bubbles at higher concentrations decreases by a factor 3 as compared to the most dilute cases. To check whether this increment was coming from detection of blobs of bubbles rather than single ones, we did experiments with a single camera positioned perpendicularly to the flow. The two-dimensional images were used to track bubbles manually making sure that the trajectories indeed corresponded to single bubbles. In figure 2.10 the mean bubble rise velocities from the one-camera two-dimensional analysis are plotted. A similar behavior is observed, first a decrease with concentration, followed by a slight increase for the most concentrated flows, confirming the three-dimensional PTV results.

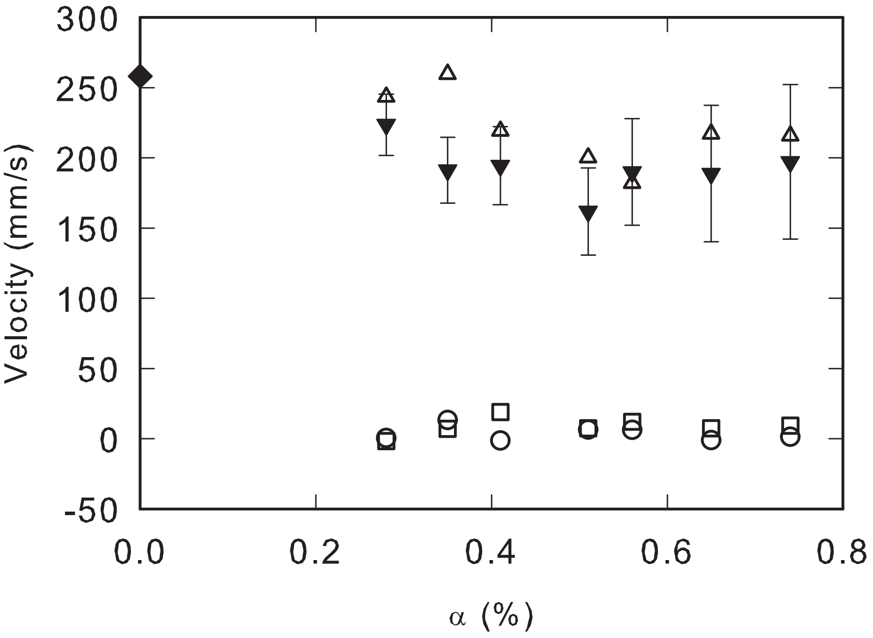

Figure 2.10: (a) Mean bubble velocity as a function of bubble concentration α. All three components are shown: ○ V_x; □ V_y; ▼ mean bubble rise velocity $\overline{V}_z$; △ mean bubble rise velocity obtained by particle tracking from single camera two-dimensional images; ⧫ terminal rise velocity for a single bubble with $d_b = 3.9$ mm. The error bars were obtained by estimating the 95% confidence interval for the mean.

2.3.5 Bubble velocity distributions

Figure 2.11 shows the PDF of all velocity components at the most dilute concentration ($\alpha = 0.28\%$). The number of data points used for calculating the PDFs was larger than 9×10^4 for the highest concentration α=0.7% and of order 3×10^5 for the most dilute case. Even for the most concentrated flow, the number of data points was large enough to assure the statistically convergence of the PDFs. All PDFs show non-Gaussian features, as nicely revealed in the semi-log plot of the PDFs (figure 2.12).

In order to quantify the non-Gaussianity of the PDFs, the flatness values of the distributions were calculated. Their values are shown in the inset of figure 2.11 and are within the range $6-13$. The flatness of the vertical component has always the highest values in the whole range of void fraction.

The effect of the concentration on the PDFs is also shown in figure 2.12. As in that figure, the PDFs are shown on a semi-logarithmic scale so that the deviation from the Gaussian-like shape become more visible, it is revealed that there is no substantial change in the shape of the distributions with increasing bubble concentration.

We would like to compare the non-Gaussianity of the PDFs ("intermittency") found here with a comparable system, namely Rayleigh-Bénard convection as the analogy between bouyancy-driven bubbly flows and free thermal convection is interesting [see 49]. In Rayleigh-Bénard convection a fluid between two parallel plates is heated from below and cooled from above (see [50] for a recent review). Prominent coherent structures in this system are thermal plumes, which are fluid particles either hotter or colder than the background fluid. Due to the density difference with the background fluid, hotter plumes ascend and colder ones descend. The system is solely buoyancy-driven. Particularly, for large Pr (defined as the ratio of kinematic viscosity and thermal diffusivity of the working fluid) the plumes keep their integrity thanks to the small thermal diffusivity, so that the similarity with pseudo-turbulence is appealing (we stress however that of course there are differences between the two systems which have been pointed out by Climent *et al.* [49]).

Do the statistics of the velocity fluctuations in Rayleigh-Bénard share a similar behavior with those of bubbles in pseudo-turbulence? In Rayleigh-Bénard convection, the PDF of the vertical velocity fluctuations of the background fluid—i.e. the central region of the cell—exhibits a Gaussian distribution [51]. Qiu *et al.* [52], and Sun *et al.* [53] measured the vertical velocity fluctuations in the region where the plumes abound, they found that the PDF still follows a Gaussian function. Those measurements, carried out for $Pr \approx 4$, indicate clearly that the PDF of the plume velocity fluctuations can be described by a Gaussian function, which differs significantly from the statistics of the bubble velocity in pseudo-turbulence. A possible reason of this difference could be that buoyancy in pseudo-turbulence is much stronger than that of the plumes in Rayleigh-Bénard system.

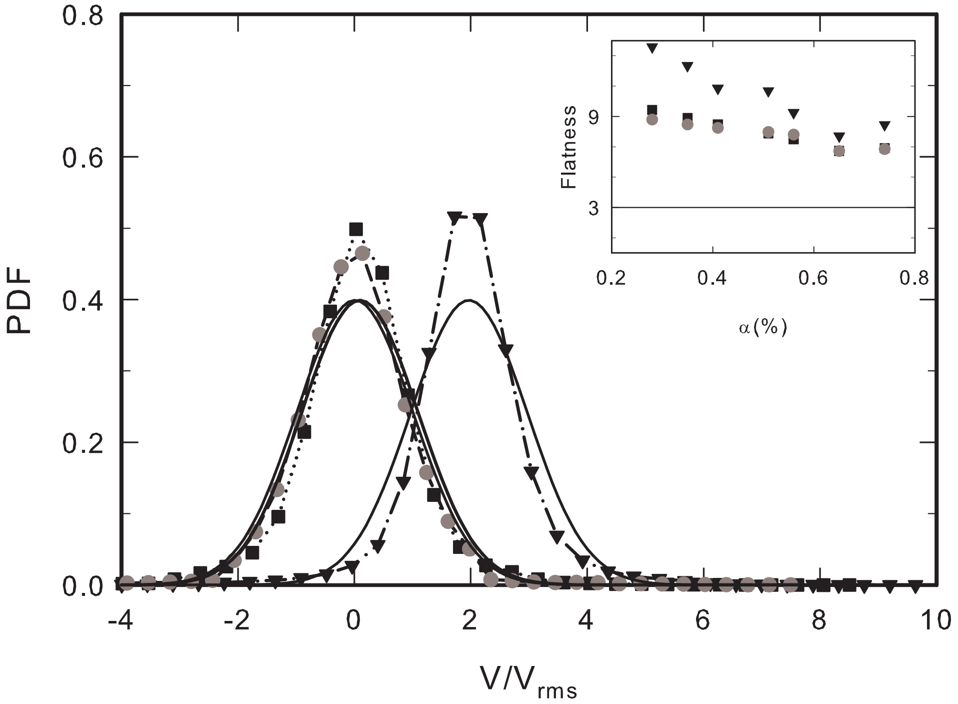

Figure 2.11: PDFs for the three bubble velocity components for $\alpha = 0.28\%$ normalized with the root mean square (r.m.s.) values of each component. V_x: dotted line with squares, V_y: dashed line with circles (both with V_{mean} velocities as expected), V_z: dotted-dashed line with triangles. The respective black solid lines (without symbols) show a Gaussian with the same mean and width as the measured distributions. The inset presents the flatness of the distribution as a function of the concentration α. The horizontal solid line in the inset represents the flatness for a normal distribution. Squares, triangles, and circles have the same meaning as in the main plot.

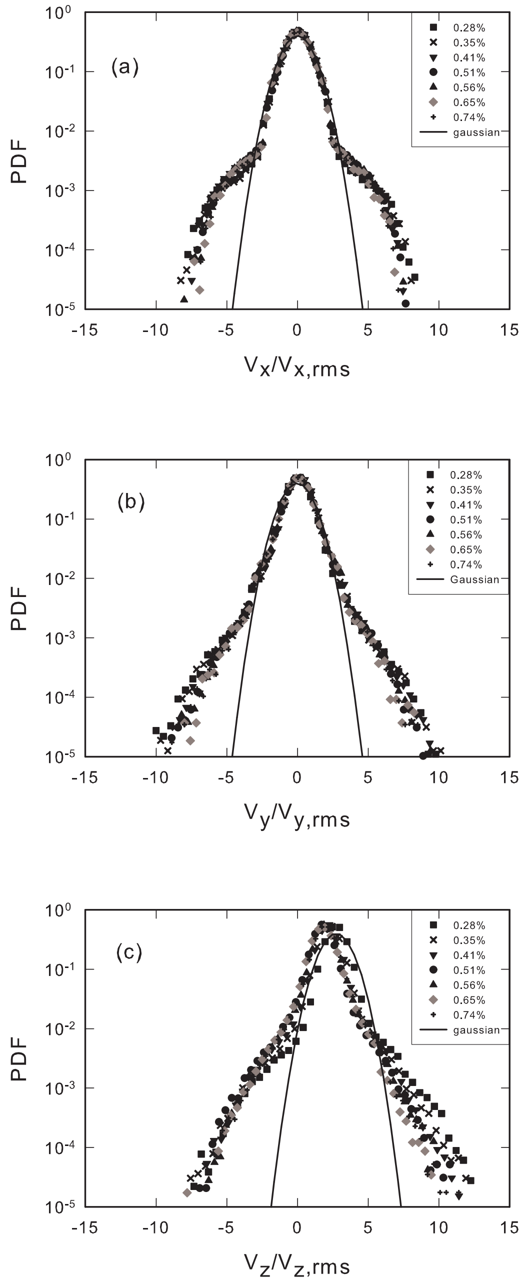

Figure 2.12: Same PDFs of the bubble velocity normalized with the r.m.s. values of each component as in figure 2.11, but now on a semi logarithmic scale to better reveal intermittency effects for various concentrations. As a reference, a Gaussian curve with the same mean and standard deviation as for the distribution with $\alpha = 0.28\%$ is plotted as a solid line.

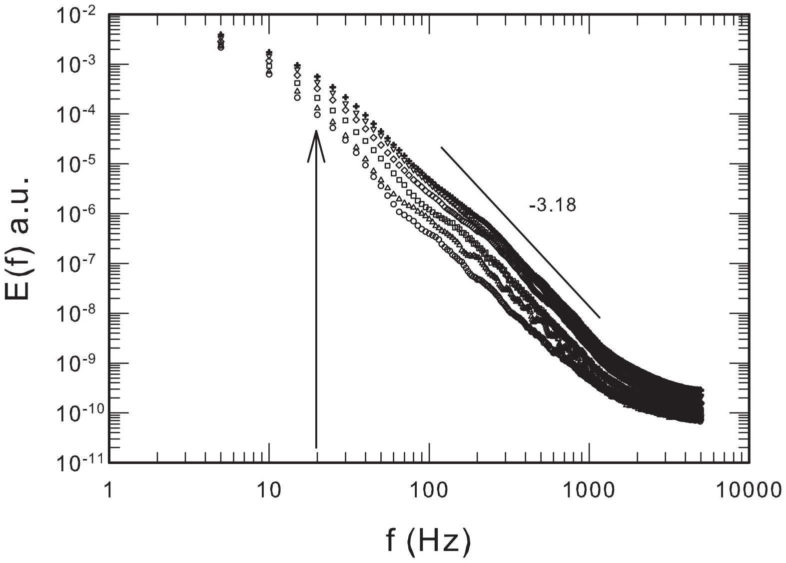

Figure 2.13: Liquid energy spectra for different void fractions. ○ α=0.2%, △ α=0.4%, □ α=0.8%, ◇ α=1.3%, ▽ α=1.7%, $+$ α=2.2%. The arrow shows the onset frequency of the scaling.

2.3.6 Energy spectra of pseudo-turbulence

Figure 3.4 shows the energy spectra for all gas fractions. As it can be seen, the slope of the energy spectrum hardly depends on the volume fraction—all curves show a slope of about -3.2. We stress that this scaling behavior is maintained for nearly two decades, much wider than it had been reported in prior observations of this steep slope of pseudo-turbulence spectra [1, 12, 27]. As it was mentioned in section 2.2.4, the way the power spectrum was calculated in this investigation differs from previous ones in two aspects: firstly, the indicator function has been measured by means of the optical fibers; and secondly, an energy spectrum has been calculated for all individual liquid segment, before the final spectrum is obtained through averaging.

One wonders whether the duration of our interrupted time series is large enough to resolve the low frequency part of the spectrum: if the duration of these segments is too short, then indeed the low frequencies in the power spectrum can not be resolved. On the other hand, if the duration of the liquid segments is large enough, then all frequencies in the spectrum are well resolved. Figure 2.14 shows the distribution of the logarithm of the non-interrupted time series duration for three different concentrations. For α=2.2% (the most concentrated bubbly flow with more bubble-probe interactions, thus shorter liquid segments) around 90% of the segments used to con-

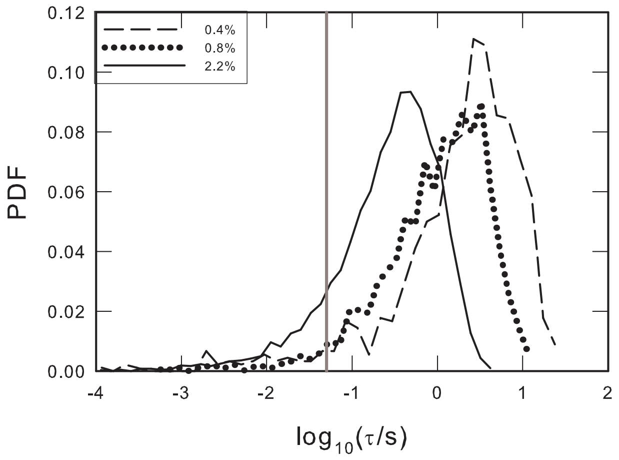

Figure 2.14: Distribution of the time duration of the parts containing liquid information in the CTA-signal used to calculate the spectrum for three different bubble concentrations. The solid vertical line corresponds to the onset frequency of the scaling in figure 3.4, see arrow in that plot.

struct the spectrum have a duration larger than 0.05 s. Comparing with figure 3.4, we can see that for frequencies higher than 20 Hz we have resolved the inertial range, where the slope is ≈ -3.2. Thus the measurement of the spectra is consistent.

Why does the slope differ from the Kolmogorov value $-5/3$? One might expect a different scaling in pseudo-turbulence, as the velocity fluctuations are caused by the rising bubbles and not by the Kolmogorov-Richardson energy cascade, initiated by some large scale motion. The difference between these two scalings is not yet completely understood, but there are some hypothesis on its origin. One possible explanation for the different scaling in pseudo-turbulence was given by Lance *et al.* [1]. They argued that eddies from the bubble wake are immediately dissipated before decaying towards smaller eddies, which would lead to the $-5/3$ scaling. They derived a -3 scaling, balancing the spectral energy, and assuming that the characteristic time of spectral energy transfer is larger than those of dissipation and production. More evidence that wake phenomena are related to the -3 scaling has been given by Risso *et al.* [54] and by Roig *et al.* [17]. They showed that bubbles' wakes decay faster in pseudo-turbulence than in the standard turbulent case with the same energy and integral length scale. They also proposed a spatial and temporal decomposition of the fluctuations in order to gain more insight into the different mechanisms. In their experiments they used a fixed array of spheres. Very recently, Riboux *et al.* [27] measured the spatial energy spectrum in pseudo-turbulence by means of PIV. They measured the spectrum just immediately after a bubble swarm has passed and obtained a -3 decay for wavelengths larger than the bubble diameter (2 mm $< l_c <$7 mm). For wavelengths smaller than the bubble diameter they found that the spectrum recovered the $-5/3$ scaling. Their findings showed that the scaling is independent on the bubble diameter and void fraction in their range of parameters investigated ($0.2\% \leq \alpha \leq 12\%$ and $d_b = 1.6-2.5$ mm), which we also find. Their conclusion is that the -3 scaling is only a result of the hydrodynamic interactions between the flow disturbances induced by the bubbles. Their arguments for this statement are that the scaling appears for wavelengths larger than the bubble diameter and that a different scaling was found for smaller wavelengths. It is worthwhile to emphasize that in our case, we measured *within* the swarm where production is still maintained and steady. The -3 scaling in our measurements is in the range of 8 mm down to hundreds of micrometers (estimated by considering the mean bubble rise velocity and the starting and ending frequencies of the scaling of the spectrum in figure 3.4), thus for lengths not only larger than d_b but also for those up to one order of magnitude smaller than it. This supports that the dissipation of the bubble wake is involved and still a valid explanation for the -3 scaling as proposed by Lance *et al.* [1]. In any case, previous works [12, 17, 27, 54] and the present one show that the -3 scaling is typical for pseudo-turbulence.

One further result supporting this idea is the one obtained by Mazzitelli *et al.* [13] who performed numerical simulations of micro-bubbles in pseudo-turbulence modeling them as point particles. Their DNS treated up to 288000 bubbles, where near-field interactions were neglected, thus wake mechanisms can not be accounted for, and effective-force models were used for the drag and lift forces. They obtained a slope of the power spectrum close to $-5/3$ typical for the turbulent case. This gives evidence that the bubble's wake—missing in the point particle approach— and its dissipation play a very important role for the -3 scaling of the energy spectrum in pseudo-turbulence.

2.4 Summary

We performed experiments on bubble clustering using three dimensional PTV. This is the first time that the technique is used to investigate bubbly flows in pseudo-turbulence in very dilute regimes ($\alpha < 1\%$). Bubble positions were determined to study bubble clustering and alignment. For that purpose the pair correlation function $G(r,\theta)$ was calculated. As the radial correlation $G(r)$ shows, pairs of bubbles cluster within few bubble radii $2.5 < r^* < 4$. Varying the bubble concentration does not have any effect on the clustering distance. The angular pair correlation $G(\theta)$ shows that a robust vertical alignment is present at both small and large scales, as it is observed when varying the radius of the spherical sector (r^*=40, 15, and 5). Decreasing the radius of the spherical sector shows that horizontal clustering also occurs, as the peak of the angular correlation around $\pi/2$ starts to grow with decreasing values of r^*.

PDFs of bubble velocity show that all components of bubble velocity behave differently from Gaussian. The implementation of this non-intrusive imaging technique assures enough data points to obtain convergence in the PDFs. The improvement achieved in the number of data-points, compared with previous experimental investigations, is of order 10^2. Furthermore, this allowed us to show the intermittent signature that bubble distributions have for all components. The flatness values for these velocity distributions are in the range of $6-13$. The distribution of the rise velocity showed the highest values of flatness, e.g. ≈ 13 at $\alpha = 0.28\%$. The non-Gaussianity can be a result of the cluster formation mechanism, where the rise velocity of single bubbles is affected by the faster collective motion of clusters. However further investigations are needed to fully understand its origin.

We have shown that the power spectrum in pseudo-turbulence ($b = \infty$) decays exponentially with a slope near -3 which is consistent with the theoretical scaling that Lance *et al.* [1] derived and supporting the hypothesis that bubble wake mechanisms are closely related to it. We have shown that the implementation of phase-sensitive CTA for studying bubbly flows is of great advantage, allowing a direct recognition and discarding of bubble-probe interactions.

The next step of our research will be to investigate bubble clustering for $b << 1$, where turbulent effects become dominant. Another line of research is to analyze pseudo-turbulence with smaller bubbles (e.g. achieved by surfactants Takagi *et al.* [46]), to study the effect of the length scale of the bubble on the spectra.

References

[1] M. Lance and J. Bataille, “Turbulence in the liquid phase of a uniform bubbly air–water flow”, J. Fluid Mech. **222**, 95–118 (1991).

[2] B. Deckwer, *Bubble column reactors*, first edition (Wiley) (1992).

[3] S. Ayyalasomayajula, A. Gylfason, L. R. Collins, E. Bodenschatz, and Z. Warhaft, “Lagrangian measurements of inertial particle accelerations in grid generated wind tunnel turbulence”, Phys. Rev. Lett. **97**, 144507 (2006).

[4] J. Salazar, J. de Jong, L. Cao, S. Woodward, H. Meng, and L. Collins, “Experimental and numerical investigation of inertial particle clustering in isotropic turbulence”, J. Fluid Mech. **600**, 245–256 (2008).

[5] E. Saw, R. Shaw, S. Ayyalasomayajula, P. Chuang, and A. Gylfason, “Inertial clustering of particles in high-Reynolds-number turbulence”, Phys. Rev. Lett. **100**, 214501 (2008).

[6] E. Calzavarini, T. van der Berg, F. Toschi, and D. Lohse, “Quantifying microbubble clustering in turbulent flow from single-point measurements”, Phys. Fluids **20**, 040702 (2008).

[7] E. Calzavarini, M. Kerscher, D. Lohse, and F. Toschi, “Dimensionality and morphology of particle and bubble clusters in turbulent flow”, J. Fluid Mech. **607**, 13–24 (2008).

[8] J. Bec, L. Biferale, G. Boffetta, A. Celani, M. Cencini, A. Lanotte, S. Musacchio, and F. Toschi, “Acceleration statistics of heavy particles in turbulence”, J. Fluid Mech. **550**, 349–358 (2006).

[9] F. Toschi and E. Bodenschatz, “Lagrangian properties of particles in turbulence”, Annu. Rev. Fluid Mech. **41**, 375–404 (2009).

[10] A. S. Smereka, “On the motion of bubbles in a peridic box”, J. Fluid Mech. **254**, 79–112 (1993).

[11] A. Sangani and A. Didwana, “Dynamic simulations of flows of bubbly liquids at large Reynolds numbers”, J. Fluid Mech. **250**, 307–337 (1993).

[12] K. Sugiyama, S. Takagi, and Y. Matsumoto, “Multi-scale analysis of bubbly flows”, Comp. Meth. in App. Mech. and Eng. **191**, 689 – 704 (2001).

[13] I. Mazzitelli and D. Lohse, “Evolution of energy in flow driven by rising bubbles”, Phys. Rev. E **79**, 066317 (2009).

[14] A. Cartellier and N. Rivière, “Bubble-induced agitation and microstructure in uniform bubbly flows at small to moderate particle Reynolds number”, Phys. Fluids **13** (2001).

[15] F. Risso and K. Ellingsen, “Velocity fluctuations in a homogeneous dilute dispersion of high-Reynolds-number rising bubbles”, J. Fluid Mech. **453**, 395–410 (2002).

[16] R. Zenit, D. Koch, and A. Sangani, “Measurements of the average properties of a suspension of bubbles rising in a vertical channel”, J. Fluid Mech. **429**, 307–342 (2001).

[17] V. Roig and L. de Tournemine, “Measurement of interstitial velocity of homogeneous bubbly flows at low to moderate void fraction”, J. Fluid Mech. **572**, 87–110 (2007).

[18] L. van Wijngaarden, “The mean rise velocity of pairwise-interacting bubbles in liquid”, J. Fluid Mech. **251**, 55–78 (1993).

[19] L. van Wijngaarden, “Bubble velocities induced by trailing vortices behind neighbours”, J. Fluid Mech. **541**, 203–229 (2005).

[20] J. Kok, “Dynamics of a pair of bubbles moving through liquid. Part 1. Theory”, Eur. J. Mech. B **12**, 515–540 (1993).

[21] B. Bunner and G. Tryggvason, “Dynamics of homogeneous bubbly flows. Part 1. Rise velocity and microstructure of the bubbles”, J. Fluid Mech. **466**, 17–52 (2002).

[22] B. Bunner and G. Tryggvason, “Effect of bubble deformation on the properties of bubbly flows”, J. Fluid Mech. **495**, 77–118 (2003).

[23] A. Esmaeeli and G. Tryggvason, “A direct numerical simulation study of the buoyant rise of bubbles at O(100) Reynolds number”, Phys. Fluids **17**, 093303 (2005).

[24] J. Martínez Mercado, C. Palacios Morales, and R. Zenit, “Measurements of pseudoturbulence intensity in monodispersed bubbly liquids for $10<\mathrm{Re}<500$”, Phys. Fluids **19**, 103302 (2007).

[25] B. Bunner and G. Tryggvason, “Dynamics of homogeneous bubbly flows. Part 2. Velocity fluctuations”, J. Fluid Mech. **466**, 53–84 (2002).

[26] J. Rensen, S. Luther, and D. Lohse, “The effects of bubbles on developed turbulence”, J. Fluid Mech. **538**, 153–187 (2005).

[27] G. Riboux, F. Risso, and D. Legendre, “Experimental characterization of the agitation generated by bubbles rising at high Reynolds number”, J. Fluid Mech. **643**, 509–539 (2010).

[28] R. Mudde, J. Groen, and H. van der Akker, “Liquid velocity field in a bubble column: LDA experiments”, Chem. Eng. Sci. **52**, 4217 (1997).

[29] Z. Cui and L. Fan, “Turbulence energy distributions in bubbling gas-liquid and gas-liquid-solid flow systems”, Chem. Eng. Sci. **59**, 1755–1766 (2004).

[30] N. Mordant, E. Leveque, and J.-F. Pinton, “Experimental and numerical study of the lagrangian dynamics of high Reynolds turbulence”, New J. Phys. **6** (2004).

[31] M. Guala, A. Liberzon, B. Lüthi, A. Tsinober, and W. Kinzelbach, “On the evolution of material lines and vorticity in homogeneous turbulence”, Phys. Rev. E **533**, 339–359 (2005).

[32] M. Bourgoin, N. Ouellette, H. Xu, T. Berg, and E. Bodenschatz, “The role of pair dispersion in turbulent flow”, Science **311**, 835–838 (2006).

[33] J. Berg, B. Lüthi, J. Mann, and S. Ott, “Backwards and forwards relative dispersion in turbulent flow: An experimental investigation”, Phys. Rev. E **74**, 016304 (2006).

[34] R. Volk, E. Calzavarini, G. Verhille, D. Lohse, N. Mordant, J.-F. Pinton, and F. Toschi, “Acceleration of heavy and light particles in turbulence: Comparison between experiments and direct numerical simulations”, Physica D **237**, 2084 – 2089 (2008).

[35] K. Hoyer, M. Holzner, B. Lüthi, M. Guala, A. Liberzon, and W. Kinzelbach, “3D Scanning Particle Tracking velocimetry”, Exp. in Fluids **39**, 923–934 (2005).

[36] J. Bec, L. Biferale, G. Boffetta, M. Cencini, S. Musacchio, and F. Toschi, “Lyapunov exponents of heavy particles in turbulence”, Phys. Fluids **18**, 091702 (2006).

[37] H. Bruun, *Hot Wire Anemometry: Principles and Signal Analysis* (Oxford Univesity Press) (1995).

[38] S. Luther, J. Rensen, T. van den Berg, and D. Lohse, “Data analysis for hot-film anemometry in turbulent bubbly flow”, Exp. Therm. Fluid Sci. **29**, 821 (2005).

[39] A. Cartellier and E. Barrau, “Monofiber optical probes for gas detection and gas velocity measurements: conical probes”, Int. J. Multiphase Flows **24**, 1265–1294 (2001).

[40] J. Juliá, W. Harteveld, R. Mudde, and H. van der Akker, “On the accuracy of the void fraction measurements using optical probes in bubbly flows”, Rev. Sci. Ins. **76**, 035103 (2005).

[41] T. van den Berg, W. D. Wormgoor, S. Luther, and L. D., “Phase sensitive constant temperature anemometry”, Macromol. Mater. Eng. accepted **296** (2011).

[42] G. K. Batchelor, *An introduction of fluid dynamics* (Cambridge Univesity Press) (1967).

[43] I. Mazzitelli, D. Lohse, and F. Toschi, “On the relevance of the lift force in bubbly turbulence”, J. Fluid Mech. **488**, 283–313 (2003).

[44] E. Ervin and G. Tryggvason, “The rise of bubbles in a vertical shear flow”, J. Fluid Engng. **119**, 443–449 (1997).

[45] A. Tomiyama, H. Tamai, I. Zun, and S. Hosokawa, “Transverse migration of single bubbles in simple shear flows”, Chem. Eng. Sci. **57**, 1849 – 1858 (2002).

[46] S. Takagi, T. Ogasawara, and Y. Matsumoto, “The effects of surfactant on the multiscale structure of bubbly flows”, Phil. Trans. R. Soc. A **366**, 2117–2129 (2008).

[47] G. K. Batchelor, “Sedimentation in a dilute dispersion of spheres”, J. Fluid Mech. **52**, 245–268 (1972).

[48] M. Brenner, “Screening mechanisms in sedimentation”, Phys. Fluids **11**, 754–772 (1999).

[49] E. Climent and J. Magnaudet, “Large-scale simulations of bubble-induced convection in a liquid layer”, Phys. Rev. Lett. **82**, 4827–4830 (1999).

[50] G. Ahlers, S. Grossmann, and D. Lohse, “Heat transfer and large scale dynamics in turbulent Rayleigh-Bénard convection”, Rev. Mod. Phys. **81**, 503–537 (2009).

[51] Z. Daya and R. Ecke, “Does turbulent convection feel the shape of the container?”, Phys. Rev. Lett. **87**, 184501 (2001).

[52] X. Qiu and P. Tong, “Large-scale velocity structures in turbulent thermal convection”, Phys. Rev. E **64**, 036304 (2001).

[53] C. Sun and K. Xia, “Scaling of the Reynolds number in turbulent thermal convection”, Phys. Rev. E **72**, 067302 (2005).

[54] F. Risso, V. Roig, Z. Amoura, G. Riboux, and A. Billet, “Wake attenuation in large Reynolds number dispersed two-phase flows”, Phil. Trans. R. Soc. A **366**, 2177–2190 (2008).

3

Energy spectra and bubble velocity distributions in pseudo-turbulence: numerical simulations vs. experiments [*] [†]

Direct numerical simulations (DNS) are performed to study the behavior of a swarm of rising air bubbles in water, employing the front tracking method, which allows to handle finite-size bubbles. The swarms consist of monodisperse deformable 4 mm bubbles with a gas fraction of 5% and 15%. This chapter focuses on the comparison of the liquid energy spectra and bubble velocity probability density functions (PDFs) with experimental data obtained with phase-sensitive constant-temperature anemometry (CTA) and three-dimensional particle tracking velocimetry (PTV), respectively. The numerical simulations confirm that the spectra of the velocity fluctuations driven by the rising bubbles follow a power law with slope close to -3*, supporting the idea that the dissipation of the bubble wake is the origin of this spectral scaling, as previously proposed in [1]. The computed PDFs of the bubble velocity show non-Gaussian features, as is also observed in the experiments. The agreement with experimental measurements is especially good in the peak region, whereas the tails of the experimental PDFs show more intermittency in comparison to the numerical results. This*

---

[*] Submitted as: I. Roghair, J. Martínez Mercado, M. van Sint Annaland, H. Kuipers, C. Sun and D. Lohse, Energy spectra and bubble velocity distributions in pseudo-turbulence: numerical simulations vs. experiments, Int. J. Mult. Flow

[†] The experimental results in this chapter are part of the present thesis. The numerical work is due to Ivo Roghair. Both authors contributed equally in the analysis.

can be explained by the lack of large-scale flow structures in the simulations, and by the large difference in measurement time.

3.1 Introduction

Bubble columns are gas-liquid contacting devices frequently used in the (bio)chemical, and metallurgical industries. Detailed knowledge on the behavior and interaction of both phases is essential for a proper design and optimization, in which numerical modeling at different scales can play a crucial role [2]. As bubbles rise through the liquid column, they induce liquid fluctuations which are referred to as pseudo-turbulence. A correct understanding of the pseudo-turbulence is critical for the simulation of bubbly flows, since it influences momentum, heat, and mass transfer rates. The characteristics of these turbulent fluctuations in the liquid are reflected in the energy spectrum. It has been shown that the energy cascade of pseudo-turbulence behaves differently from homogeneous single-phase turbulence, and hence deserves special attention in large-scale models. Lance *et al.* [1] studied bubbles rising through an imposed turbulent flow. They measured the energy spectrum of the fluctuations and found a power law scaling with a slope of about $-8/3$, in contrast to the classical $-5/3$ for homogeneous single-phase turbulence. They explained the change of the slope as a wake dissipation effect. Their scaling argument gives an exponent of -3, close to the experimentally found value. The value -3 is also obtained by Risso [3], arguing that the signals from the wake of the rising bubbles would be viewed as a sum of localized random bursts, with statistically independent strength and size.

In contrast, in the numerical work on pseudo-turbulence by Mazzitelli *et al.* [4] a slope of $-5/3$ of the energy spectrum was observed together with a stable inverse energy cascade, where the energy input occurs on the small scales (i.e. rising bubbles). Energy is then transferred to large scales, building up large-scale motion. However, in those simulations bubbles were approximated as point-like particles, thus disregarding finite-size effects and capillary phenomena. As Mazzitelli *et al.* [4] mentioned in their paper, the “wrong” $-5/3$ scaling cannot be the signature of real (experimental) bubble columns.

Indeed in our experiments presented in chapter 2, we found a scaling of the energy spectrum close to -3 for various gas fractions in the very dilute regime. These results were obtained by single-point measurements in flows with gas fractions ranging from $\alpha = 0.8$ to 2.2%, using a phase-sensitive CTA probe. Furthermore, in the work by Riboux *et al.* [5] energy spectra were measured with particle image velocimetry (PIV) in the wake of a bubble swarm (because PIV measurements could *not* be done *within* the swarm due to the light reflection at the bubbles’ interface). Their results confirmed a scaling close to -3 for length scales larger than the bubble diameter. For smaller length scales their measurements recovered the $-5/3$ slope. The scaling was independent of bubble diameter and bubble concentration. Numerically, Bunner *et al.* [6] computed the power spectrum for a swarm of ellipsoidal bubbles employing the front tracking method and found a slope of -3.6. They also observed a strong anisotropic flow, in contrast to Lance *et al.* [1]. They explained the difference by arguing that a large-scale convection pattern, induced by the bubbles, was present in the experiments.

The PDF of bubble velocities provide useful information for modeling force correlations used in bubbly flow simulations. Several numerical works [6–8], have obtained PDFs of the bubble velocity for non-deformable and deformable bubbles. For the case of non-deformable spherical bubbles, the PDFs have a Gaussian distribution whereas for ellipsoidal deformable bubbles the PDFs deviated from Gaussian at low void fractions, recovering Gaussianity only as the bubble density increases. Experimentally, PDFs of bubble velocity have been measured by Zenit *et al.* [9] and by Martínez *et al.* [10]. Their measurements were carried out using an intrusive technique and the number of data points used for the PDFs was not sufficient to determine a well defined distribution.

In this work, in an attempt to improve on the point-bubble simulations of Mazzitelli *et al.* [4], we carry out DNS of bubble swarms with a Front Tracking model aiming at resolving the bubbles' wake. With this approach both finite-size and shape deformations (by tracking the bubbles' interface) can be taken into account. In this manner it will be possible to quantify whether bubble wake phenomena influence the energy spectrum scaling. We will provide a direct comparison of our numerical energy spectra and other statistical properties like PDFs of the bubble velocity with the experimental results mentioned in chapter 2 and discuss the differences. Of particular interest are air bubbles in water. That implies that we use a density ratio of $\rho_g/\rho_l = O(1000)$ and a viscosity ratio of $\mu_g/\mu_l = O(100)$.

One of the strongest advantages of numerics is the non-intrusive access to velocities and velocity-derived quantities in the whole numerical domain. Besides that, the void fraction can be considerably larger as compared to experiments which rely on optical techniques, which are restricted to very dilute bubbly flows, such as PTV or laser doppler anemometry (LDA) [11, 12]. On the other hand, due to computational restrictions, the simulated domain sizes and times are much smaller than those typically used in experiments, leading to poor statistics in the simulations.

This chapter starts with a short description of the Front Tracking model, including details on the data sampling by our numerical probes. Then results of energy spectra of the liquid fluctuations and bubble velocity distributions are presented and compared to experimental results. The last section summarizes and discusses the present work.

3.2 Numerical method

3.2.1 Front tracking

Direct numerical simulations are performed using a full three-dimensional Front Tracking model (based on [13, 14]). Details on the actual implementation are given in [15], while validation with experiments using single rising bubbles is given in [16, 17]. Furthermore, we have favorably compared the velocity of a single rising bubble, with the results presented in [18].

The model solves the incompressible Navier-Stokes equations (3.1) using a one-fluid formulation on a Eulerian grid using a source-term $\mathbf{F}_\sigma$ to account for the surface tension force at the interface:

$$\rho \frac{\partial \mathbf{u}}{\partial t} + \rho \nabla \cdot (\mathbf{u}\mathbf{u}) = -\nabla p - \nabla \cdot \boldsymbol{\tau} + \rho \mathbf{g} + \mathbf{F}_\sigma, \tag{3.1}$$

$$\nabla \cdot \mathbf{u} = 0. \tag{3.2}$$

The equations are solved using a two-step projection-correction method, firstly resolving the momentum equations with semi-implicit shear stress terms (projection), followed by a pressure-correction step. Both iterative approaches use an incomplete Cholesky conjugate gradient (ICCG) matrix solver on a single CPU.

The interface between the phases is tracked using Lagrangian marker points (control points). These control points are interconnected, forming a triangular mesh, from which the surface tension force $\mathbf{F}_\sigma$ can be calculated. This force is mapped back to the Eulerian grid at the location of the interface, using mass-weighing. After calculation of the flow field, the marker points are moved with the interpolated fluid flow, which eventually may result in edges of the triangular mesh varying in size. A remeshing procedure assures that the size of these edges is kept within predefined limits, e.g. by removing or adding marker points.

The flow field has periodic boundaries in all three directions. In order to prevent the system from energetically diverging due to the buoyancy force (see e.g. [19]), the net average fluid flow velocity is subtracted from each velocity vector every time step.

3.2.2 Typical conditions

The bubbles are initially spherically shaped and placed randomly throughout the cubic uniform computational domain. The fluid flow velocity is set to zero. Our base-case is air-water (with a Morton number $\mathrm{Mo} = g\mu_l^4(\rho_l - \rho_g)/(\rho_l^2\sigma^3) = 2.5 \cdot 10^{-11}$). Table 3.1 shows the physical parameters for the air-water case. We adjust the size of the computational domain to obtain the desired void fraction. Using 20 Eulerian cells in a bubble diameter d_b ensures accurate results while keeping the computation time as short as possible—using $d_b = 4$ mm, the grid cell size is $2{\cdot}10^{-4}$ m. A number

Table 3.1: Physical properties for the air-water simulations.

Viscosity (gas phase)	μ_g	$1.8 \cdot 10^{-5}$	$\mathrm{m\,Pa\,s}$
Density (gas phase)	ρ_g	1.25	$\mathrm{kg\,m^{-3}}$
Viscosity (liquid phase)	μ_l	0.001	$\mathrm{m\,Pa\,s}$
Density (liquid phase)	ρ_l	1000	$\mathrm{kg\,m^{-3}}$
Surface tension coefficient	σ	0.073	$\mathrm{N\,m^{-1}}$
Gas fraction	α	0.05—0.15	–

of $N_b = 16$ bubbles are used. With this choice of N_b, our results are independent of the number of bubbles. This was checked by comparing bubble rise velocities in simulations varying N_b between 4 and 32. Moreover, [18] mentioned that at least 12 bubbles should be used. The bubble Reynolds number $\mathrm{Re_b} = \rho_l u_b d_b / \mu_l$ is of order O(1000). The Eötvös number is $\mathrm{Eo} = g d_b^2 (\rho_l - \rho_g)/\sigma = 2.15$.

The simulation time is 4 s and we use a time step of $5 \cdot 10^{-5}$ s. In [17], it was shown that using a time step of 10^{-4} s provides same averaged results as a time step of 10^{-5} s for a single rising bubble. Reducing the time step is done for stability purposes and not for accuracy.

3.2.3 Data acquisition

To exclude transient effects of the initially quiescent liquid and bubbles, the interval of 0.0 s — 0.2 s is discarded for the analysis. The bubble velocities are sampled each $1 \cdot 10^{-4}$ s, as the velocity of the center-of-mass of the bubble, which is determined from the location of the marker points on the interface mesh.

For the energy spectra calculations numerical probes were used. These probes register the phase fraction and the fluid velocity vector in the computational cell at each time step (typically $5 \cdot 10^{-5}$ s), providing a signal very similar to the signal from the experiments. Also, the size of the computational cells is comparable to the experimental probe. Hence, these probes are the numerical equivalent to the phase-sensitive CTA as described in [20, 21]. An array of $3 \times 3 \times 3$ probes was located throughout the computational domain.

Due to the staggered discretization of the velocity field, a linear interpolation from the cell edges was performed for the phase fraction and velocity at the cell center. Figure 3.1 shows both a typical signal for the phase fraction and velocity from numerics and those obtained with a phase-sensitive CTA.

There are some slight differences with the experimental probes, however. Because the velocity of both phases is defined on a single velocity field, the signal is continuous even when an interface crosses the probe. In addition, the phase is represented

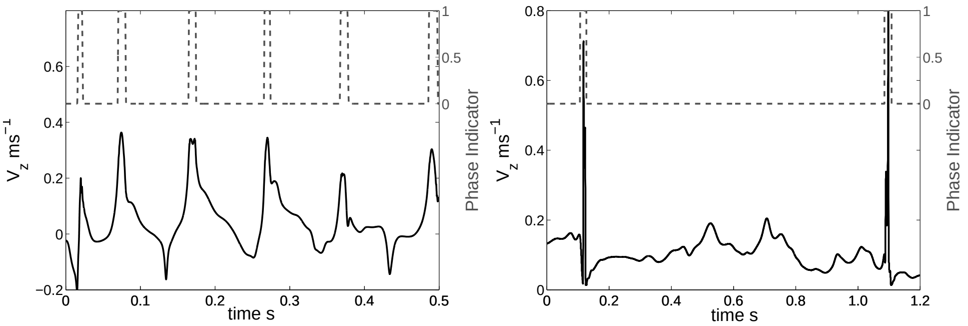

Figure 3.1: Typical velocity and indicator function signals. The solid line shows the vertical fluid velocity, the dashed line the phase fraction (0: liquid, 1: bubble). Left: single numerical probe for a low void fraction simulation. Right: experimental phase-sensitive CTA probe. Note that the phase fraction of the simulation is twice as high as in the experiments.

as a fraction (i.e. the gas fraction in the computational cell) instead of a binary phase indicator.

3.3 Energy spectra

For the calculation of the energy spectra of liquid fluctuations we follow the method described in chapter 2. Since the numerical phase indicator is not binary as in the experimental data, we set it to zero if the cell contains only liquid. Therefore, we have a collection of segmented velocity signals in time for each numerical probe. For each probe we calculate the power spectrum density of the segments larger than 256 data points and average over all segments. Finally, an ensemble average over all the 27 probes is done to obtain the final power spectrum. Experimentally, the liquid velocity fluctuations were measured with a cylindrical hot-film probe with its axis oriented along the (horizontal) x direction. Hence, their spectra accounted for fluctuations in the y and z directions. For this reason, we also report the energy spectrum considering the fluctuations of these components of the velocity (E_{yz}), which give the same result as compared to E_{xz} as can be seen in Figure 3.2. We stress the key role that the simulation time plays to achieve statistical convergence of the spectrum for all the numerical probes. If the simulation time is not long enough, each spectrum obtained from the numerical probes will depend strongly on its location.

Figure 3.3a shows the spectrum of the 27 individual probes in the air-water simulation with 16 bubbles (4mm). This is our longest simulation of all air-water cases (4 s), but it has the lowest bubble concentration (α=5%). We observed that all the

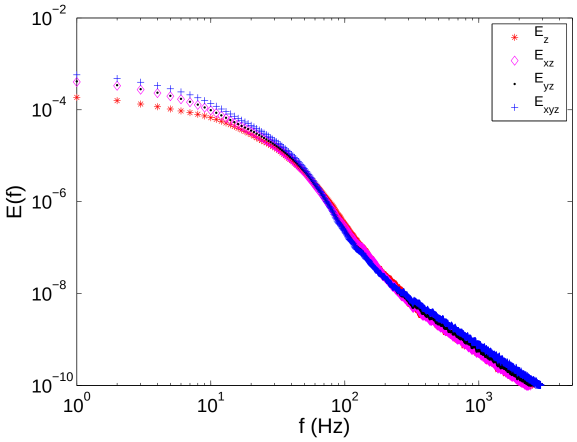

Figure 3.2: The energy spectra calculated considering different components of the fluctuations are similar. Higher energies are obtained when more velocity components are taken into account.

probes show a similar behavior and that averaging them is reasonable and will give a well-converged spectrum. This result can be compared with another air-water simulation with α=5% and 32 bubbles (4mm), but with a shorter simulation time (1.2 s). These results are shown in figure 3.3b. It is clearly seen from that figure that full convergence on the large scales has not yet been achieved. For this short simulation time, the spectra of the probes show considerably deviations from each other – simply averaging them does not guarantee convergence. Similar results are obtained for other air-water simulations which run only 2 s or less.

We therefore focus on the fully converged case of the air-water simulation with α=5%. Figure 3.4 shows the averaged spectrum of all 27 numerical probes together with the experimental data. The simulation shows a good agreement, having a slope close to -3 in the frequency range of 20—200 Hz. The scaling frequency range for the numerics is shorter as compared to the experimental case due to the difference in simulation and measurement time. Risso *et al.* [11] pointed out that the power spectra are not influenced by α, based on their experimental findings. In spite of a shorter simulation time and the above discussed convergence problems, in figure 3.4 we also show the spectra for a case with α=15%. Due to the smaller signal segments, caused by the smaller distance between the bubbles at higher gas loadings, the -3 scaling range shrinks to less than a decade.

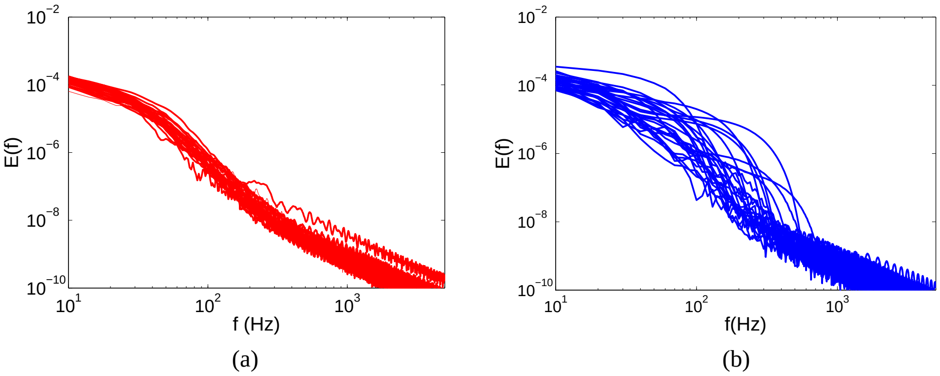

(a)

(b)

Figure 3.3: The energy spectra of each of the 27 numerical probes. (a) 4 s air-water 16-bubble simulation with α=5%, (b) 1.2 s air-water 32-bubble simulation withα=5%. In figure 3.3a, all the spectra show a well-converged similar behavior that is independent of the probe location. The spectra of half as long simulations or less (see 3.3b) do not show this good convergence yet, neither do simulations with enhanced viscosity.

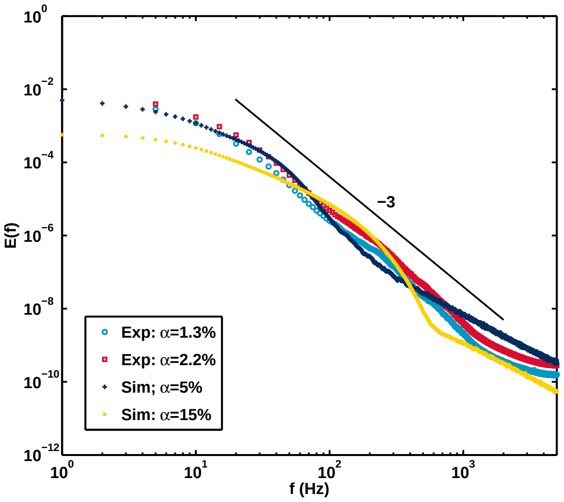

Figure 3.4: The energy spectra of the simulation is compared to experimental results. For the simulation with α=5%, a power law close to -3 is observed for nearly one decade starting for frequencies of about 20Hz till 200 Hz. We also show the simulation case with α=15% and with 2 s simulation time, which is not yet fully converged.

3.4 Bubble velocity distribution

Figure 3.5 shows the (logarithm of the) PDFs of the bubble velocity normalized by their standard deviation. As it is very difficult either in numerics to reduce α without exponentially increasing the required computation time or to increase α in experiments due to the optical restriction that PTV imposes for detecting single particles, for the experimental case we picked the most concentrated flow which could be measured using three-dimensional PTV, namely $\alpha = 0.74\%$. For the numerical simulations we picked $\alpha = 5\%$ instead, where (i) we have the best statistics and (ii) which still can be considered as dilute.

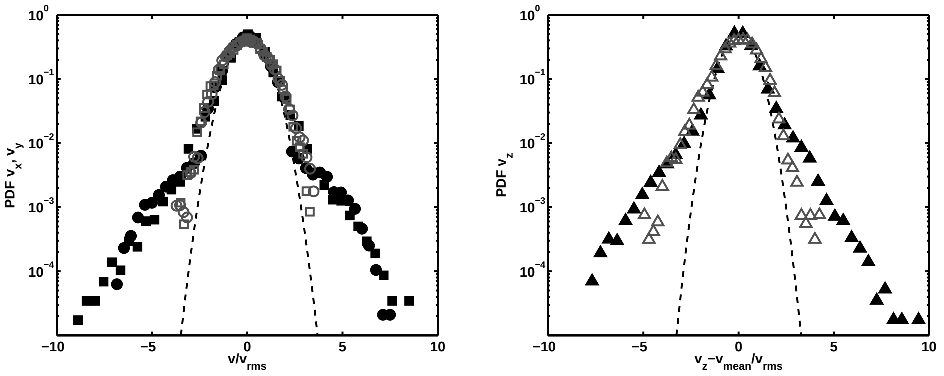

Figure 3.5: Probability Density Functions of bubble velocity. Solid symbols represent simulations ($\alpha = 5\%$), open symbols experiments ($\alpha = 0.74\%$), dashed line represents a Gaussian distribution with the same mean and width as in experiments. On the left, the figure shows the horizontal velocity components. ○: v_x and □: v_y. The figure on the right shows v_z.

Figure 3.5 shows the results for the horizontal and for the vertical components. In spite of the difference in bubble concentration, the PDFs agree reasonably well in the velocity range where we can numerically determine it. We point out that the central part of the PDFs are on top of each other and have a probability 1000 times higher than the events in the tails. Note that the measuring time in experiments is longer, so there is a larger chance of detecting the rare events leading to the pronounced tails of the PDFs. It is not possible to detect them numerically, due to CPU time limitations. In addition, large-scale structures do occur in the flow in the experimental water channel, which are not seen in our simulations due to the different boundary conditions. The deviation from Gaussianity can be observed in both cases, even in the central region, as the dashed line in figure 3.5 suggests. For a fair comparison of the flatness value, from the experimental results we have only selected velocities which are in the central part of the PDF, i.e. $-4 < (\mathrm{v} - \mathrm{v}_{\mathrm{mean}})/\mathrm{v}_{\mathrm{rms}} < 4$, which results in a flatness of around $4-5$ for the horizontal components and flatness around 5.5 for the vertical velocity. From numerics, at $\alpha = 5\%$ we get values around 3 for the horizontal components and 3.8 for the vertical component.

An investigation of the flatness as a function of the gas fraction using the numerical data shows that also for larger gas fractions $\alpha > 5\%$ the flatness of the z-component is higher than that of the horizontal components, which remain to be consistent with the Gaussian case with flatness equals to 3.

3.5 Discussion and conclusions

Results from Front Tracking DNS of a swarm of deformable air bubbles in water have been analyzed. We have compared the power spectrum of bubble induced turbulence (pseudo-turbulence) and bubble velocity distributions with experimental data of a bubble column.

We have shown that the liquid energy spectrum follows a power law with a slope close to -3, which agrees with the experimental results in the frequency range 20–200 Hz. Our finding gives additional support to the idea that this particular power law scaling in pseudo-turbulence is related to the wake dissipation of the bubbles. Mazzitelli *et al.* [4] performed pseudo-turbulence simulations with point-particle bubbles, they found the classical Kolmogorov $-5/3$ power law, as the point-particle approach cannot resolve the wakes of the bubbles. Experimental works [22, 23], and theoretical investigations [1, 3] have also indicated the importance of bubbles' wake phenomena. Hence, the finite-size leading to wake formation accounts for the pseudo-turbulence -3 spectrum.

The bubble velocity PDFs show a good agreement with experiments. Both experimental and numerical data deviate from a Gaussian distribution. Experimental data show larger tails than the numerical results due to the relatively short simulation time (because of the computational cost), but also because of the periodic boundary conditions used in the model. When using periodic boundary conditions, the possibility of occurrence of large scale patterns and rare velocity events is reduced. We do however observe a similar trend concerning the flatness of the PDFs: the vertical velocity distributions have a higher flatness than the horizontal components. We expect that if modifying the boundary conditions and longer simulation times were possible, the incidental high velocities in the tails of the distributions will also occur in the numerical simulations.

Another consequence of the periodic boundary conditions in the numerics is that the microstructure of the bubbly flow cannot be correctly captured. We have analyzed

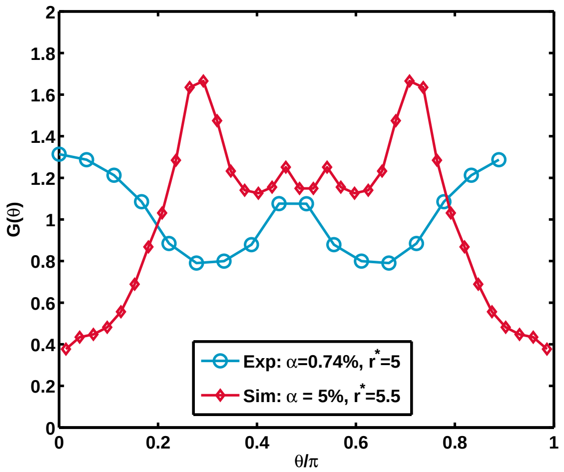

Figure 3.6: The angular pair correlation function $G(\theta)$ does not show a good agreement between simulations and experiments especially on the vertical clustering, which is due to the domain boundary conditions.

clustering effects on the numerical data by calculating the angular pair correlation function $G(\theta)$, the probability density function of the angle between the vertical axis and the vector connecting the centroids of two bubbles. In figure 3.6 numerical and experimental results are shown (details on $G(\theta)$ can be found in chapter 2), where the numerical simulation contains a gas fraction of 5% which is the closest to the gas hold-ups used in experiments. However, the radius used in the simulations (normalized by the bubble diameter) is slightly larger due to the domain size. The preferential vertical clustering as found in the experiments (see chapter 2) was not observed in the numerical results. We attribute this to the lack of large-scale flow circulations due to the limited size of the computational domain and absence of walls in the domain. Instead, strong diagonal clustering effects are observed. More numerical work on larger domains *with* walls will be required to further elucidate this issue.

References

[1] M. Lance and J. Bataille, “Turbulence in the liquid phase of a uniform bubbly air–water flow”, J. Fluid Mech. **222**, 95–118 (1991).

[2] N. Deen, M. Van Sint Annaland, and J. Kuipers, “Multi-scale modeling of dispersed gas-liquid two-phase flow”, Chem. Eng. Sci. **59**, 1853–1861 (2004).

[3] F. Risso, “Theoretical model for k^{-3} spectra in dispersed multiphase flows”, Phys. Fluids **23**, 011701 (2011).

[4] I. Mazzitelli and D. Lohse, “Evolution of energy in flow driven by rising bubbles”, Phys. Rev. E **79**, 066317 (2009).

[5] G. Riboux, F. Risso, and D. Legendre, “Experimental characterization of the agitation generated by bubbles rising at high Reynolds number”, J. Fluid Mech. **643**, 509–539 (2010).

[6] B. Bunner and G. Tryggvason, “Dynamics of homogeneous bubbly flows. Part 2. Velocity fluctuations”, J. Fluid Mech. **466**, 53–84 (2002).

[7] B. Bunner and G. Tryggvason, “Effect of bubble deformation on the properties of bubbly flows”, J. Fluid Mech. **495**, 77–118 (2003).

[8] A. Esmaeeli and G. Tryggvason, “A direct numerical simulation study of the buoyant rise of bubbles at O(100) Reynolds number”, Phys. Fluids **17**, 093303 (2005).

[9] R. Zenit, D. Koch, and A. Sangani, “Measurements of the average properties of a suspension of bubbles rising in a vertical channel”, J. Fluid Mech. **429**, 307–342 (2001).

[10] J. Martínez Mercado, C. Palacios Morales, and R. Zenit, “Measurements of pseudoturbulence intensity in monodispersed bubbly liquids for $10<\mathrm{Re}<500$”, Phys. Fluids **19**, 103302 (2007).

[11] F. Risso and K. Ellingsen, “Velocity fluctuations in a homogeneous dilute dispersion of high-Reynolds-number rising bubbles”, J. Fluid Mech. **453**, 395–410 (2002).

[12] R. Mudde, J. Groen, and H. van der Akker, “Liquid velocity field in a bubble column: LDA experiments”, Chem. Eng. Sci. **52**, 4217 (1997).

[13] S. Unverdi and G. Tryggvason, “A front-tracking method for viscous, incompressible, multi-fluid flows”, J. Comput. Phys. **100**, 25 – 37 (1992).

[14] G. Tryggvason, B. Bunner, A. Esmaeeli, D. Juric, N. Al-Rawahi, W. Tauber, J. Han, S. Nas, and Y. Jan, “A Front-Tracking method for the computations of multiphase flow”, J. Comput. Phys. **169**, 708 – 759 (2001).

[15] W. Dijkhuizen, I. Roghair, M. Van Sint Annaland, and J. Kuipers, “DNS of gas bubbles behaviour using an improved 3D front tracking model–model development”, Chem. Eng. Sci. **65**, 1427–1437 (2010).

[16] M. van Sint Annaland, W. Dijkhuizen, N. Deen, and J. Kuipers, “Numerical simulation of behavior of gas bubbles using a 3-D front-tracking method”, AIChE J. **52**, 99–110 (2006).

[17] W. Dijkhuizen, I. Roghair, M. Van Sint Annaland, and J. Kuipers, “DNS of gas bubbles behaviour using an improved 3D front tracking model–drag force on isolated bubbles and comparison with experiments”, Chem. Eng. Sci. **65**, 1415–1426 (2010).

[18] B. Bunner and G. Tryggvason, “Dynamics of homogeneous bubbly flows. Part 1. Rise velocity and microstructure of the bubbles”, J. Fluid Mech. **466**, 17–52 (2002).

[19] E. Calzavarini, C. R. Doering, J. D. Gibbon, D. Lohse, A. Tanabe, and F. Toschi, “Exponentially growing solutions in homogeneous Rayleigh-Bénard convection”, Phys. Rev. E **73**, 035301 (2006).

[20] T. van den Berg, W. D. Wormgoor, S. Luther, and L. D., “Phase sensitive constant temperature anemometry”, Macromol. Mater. Eng. accepted **296** (2011).

[21] J. Martínez Mercado, D. Chehata Gómez, D. van Gils, C. Sun, and D. Lohse, “On bubble clustering and energy spectra in pseudo-turbulence”, J. Fluid Mech. **650**, 287–306 (2010).

[22] V. Roig and L. de Tournemine, “Measurement of interstitial velocity of homogeneous bubbly flows at low to moderate void fraction”, J. Fluid Mech. **572**, 87–110 (2007).

[23] F. Risso, V. Roig, Z. Amoura, G. Riboux, and A. Billet, “Wake attenuation in large Reynolds number dispersed two-phase flows”, Phil. Trans. R. Soc. A **366**, 2177–2190 (2008).

4

Lagrangian statistics of micro-bubbles in turbulence[*]

We study Lagrangian velocity and acceleration statistics of light particles (micro-bubbles) in homogeneous isotropic turbulence. Micro-bubbles with diameter $d_b = 340\ \mu m$ *and Stokes number O(0.01) are dispersed in a turbulent water tunnel. We reconstruct their trajectories by employing three-dimensional particle tracking velocimetry (PTV) at different* Re_λ*. We compare two smoothing methods— i.e. Gaussian kernel and polynomial fitting— and show that both methods reproduce the intermittent characteristics along the micro-bubbles' trajectories. Our findings show that the micro-bubbles' acceleration probability density functions (PDFs) are highly intermittent with a flatness value of around 35. The experimental PDFs are better fitted by a stretched exponential functional rather than a log-normal distribution. In addition, the acceleration autocorrelation function decorrelate much faster compared to experiments in different type of turbulent flows (e.g. von Kármán flow), and its decorrelation time increases with higher* Re_λ*. The velocity PDFs follow closely a Gaussian distribution with no dependence on* Re_λ *for all the three components with a flatness very close to 3.*

---

[*] To be submitted in modified form to J. Fluid Mech as: J. Martínez Mercado, V. N. Prakash, Y. Tagawa, C. Sun, and D. Lohse. Lagrangian statistics of micro-bubbles in turbulence.

4.1 Introduction

Multi-phase flows where the carrier fluid transports particles under turbulent conditions are ubiquitous. A thorough understanding of the dynamics of particles (light, neutral, or heavy) in turbulent flows is therefore crucial. In these types of flows, the particles have a finite size and their density is different from that of the carrier fluid. Thus, the particle's dynamic behavior is expected to be different compared to neutral fluid tracers. The two relevant dimensionless parameters are the density ratio $\beta = 3\rho_f/(\rho_f + 2\rho_p)$, where ρ_f and ρ_p are the fluid and particle density, and the Stokes number, which is the ratio of the particle's response time τ_p to the typical time scale of the smallest eddies in a turbulent flow τ_η, defined as St$= \tau_p/\tau_\eta = a^2/3\beta\nu\tau_\eta$, where a is the particle radius and ν the kinematic viscosity of the fluid.
The Lagrangian approach is naturally suited to study particles in turbulence. It has recently attracted much attention [see 1]. The first Lagrangian investigations studied the dynamics of tracer particles in fully developed turbulence. Pioneering Lagrangian particle tracking experiments used silicon strip detectors to measure three-dimensional trajectories of tracer particles (β=1) with high spatial and temporal resolution in a von Kármán flow at high Re$_\lambda$ up to 970 [2–4]. They reported that the particle acceleration PDFs are highly intermittent with flatness values around 55 at Re$_\lambda = 690$. Although the flatness decreased at lower Re$_\lambda$, the shape of the acceleration PDFs did not show a clear dependence on Re$_\lambda$, and could be fitted with either stretched exponentials or log-normal distributions. In numerical simulations [see 5–7], the high intermittency of the fluid particle acceleration PDFs was also observed, and it was related to trapping events by vortex filaments [7].
Recent experimental efforts have been directed towards studying the effect of particle size on the acceleration. Qureshi *et al.* [8] conducted experiments in grid-generated turbulence in a wind tunnel, and tracked buoyant particles (soap bubbles) using acoustic Doppler velocimetry to measure one component of the particle velocity. Their finding was that the normalized acceleration PDF does not depend on particle size, and the particle's acceleration variance decreases with increasing particle size. These results were confirmed in [9] , where a broader range of particle sizes at different Re$_\lambda$ in a von Kármán flow were investigated. However, very recent experiments [10] reported that the normalized acceleration PDFs of inertial buoyant particles become narrower with a decrease of the flatness with increasing particle size.

To study heavy particles (β=0), Ayyalasomayajula *et al.* [11] used water droplets in wind tunnel experiments at Re$_\lambda$=250. By following the particle motion with a moving camera, they obtained their trajectories in two-dimensions. It was observed that the normalized acceleration PDF was less intermittent than for tracers, with narrower tails. Qureshi *et al.* [12] extended their previous experiments [8] to study heavy particles with different sizes, and found that the shape of the normalized acceleration PDF is independent of particle size and density. Also, the acceleration variance decreased with increasing particle size, consistent with the experimental results of [11, 13], and with the numerical work of [14].

Also the dynamics of light particles (β=3) have been investigated both numerically [see e.g. 6, 15] and experimentally [see e.g. 16, 17]. Mazzitelli and Lohse [6] found intermittency in the PDFs of the individual forces acting on bubbles, reflected in flatness values up to 175 for the PDF of the lift force. A direct comparison of the statistics of light, neutral, and heavy particles was done in [16, 17], by using data from both experiments and point-particle direct numerical simulations (DNS). Their experiments used an extended laser Doppler velocimetry technique (extended LDV) for measuring one component of the particle velocity in a von Kármán flow at high Re_λ=850. The normalized acceleration PDFs from the experiments for light, neutral and heavy particles had the same shape up to values of the acceleration $\mathrm{a} < 15\,\mathrm{a}_{rms}$, where a_{rms} is the standard deviation of the particle acceleration. In contrast, the numerical simulations in [16, 17] showed a substantial difference: the acceleration PDFs of light particles was more intermittent than that of tracers, whereas that of heavy particles was less. These authors also investigated the particle's acceleration autocorrelation, and found that the light particles' acceleration decorrelates faster than that of heavy particles. The same trend was found with numerics, though with a larger decorrelation time. However, they noticed that their numerical simulations could not completely capture the real particle dynamics as spatial filtering of turbulent fluctuations cannot occur with point-like particles. Calzavarini *et al.* [15] implemented Faxen force corrections to account for finite size effects in numerics, and indeed found a decrease of the particle acceleration variance with increasing particle size.

In the present work, we study three-dimensional Lagrangian velocity and acceleration statistics of micro-bubble at moderate Re_λ in the range 140—237. There is a wealth of information available from previous Lagrangian particle tracking experiments which mainly studied tracers in fully developed turbulence. Additionally, grid-generated turbulence experiments in wind tunnels have been only carried out with heavy particles [11, 12] or with neutral buoyant particles [8] where the authors used helium gas bubbles in a wind tunnel. Previous experimental work on particles with β=3 [16, 17] measured only one component of velocity and acceleration in a von Kármán flow. Here, we measure all three components of the particle's velocity and acceleration employing particle tracking velocimetry for micro-bubbles (β=3) of size similar to the Kolmogorov turbulent length scale in homogeneous isotropic turbulence in a water tunnel. We are interested in studying the velocity and acceleration PDFs and their autocorrelation functions. The structure of this chapter is as follows: in section 4.2 we describe the experimental facility, and analysis techniques. The results are presented in section 4.3, followed by a conclusion and summary in section 4.4.

4.2 Experiments

We conduct experiments in the Twente Water Tunnel, an 8 m long vertical water tunnel designed for studying two-phase flows. By means of an active grid, nearly homogeneous and isotropic turbulence with Re_λ up to 300 is achieved [see 18, 19]. A measurement section with dimensions $2\times0.45\times0.45$ m^3 with three glass walls provides optical access for the three-dimensional PTV system. Micro-bubbles with a mean diameter $d_b = 340$ μm are generated by blowing pressurized air through a ceramic porous plate that is located in the upper part of the water tunnel. These micro-bubbles are advected downwards by the flow passing through the measurement section.

Our three-dimensional PTV system consists of 4 Photron PCI-1024 high-speed cameras that are synchronized with a high-energy (100 W), high-repetition rate Litron laser (LDY303HE). The four cameras are focused at the center of the test section on a $40 \times 40 \times 40$ mm^3 measurement volume that is illuminated by expanding the laser beam with volume optics. The arrangement of the cameras and laser is such that the 4 cameras receive forward scattered light from the micro-bubbles. We acquire images at 10 kHz with a resolution of 256×256 pixels, resulting in a spatial resolution of about 156 μm/ pixel,

The Re_λ is varied by changing the mean flow speed in the tunnel. Table 4.1 summarizes the flow properties for the various cases considered. The flow was characterized by measurements using a cylindrical hot-film probe (Dantec R11) placed in the center of the imaged measurement volume with a sampling rate of 10 kHz.

For the three-dimensional particle tracking, we use the open source code developed at the IfU-ETH group [20]. The error in the determination of the particle's position is within sub-pixel accuracy of 60 μm, corresponding to the tolerance of epipolar matching in three dimensions. The particles' trajectories are obtained by smoothing the raw trajectory either with a Gaussian kernel or a polynomial fitting. Due to this experimental error in the position determination, the particle trajectory has to be filtered out using smoothing methods (see section 4.2.1). Velocities and accelerations are obtained by differentiating the filtered trajectory. For the Lagrangian statistics shown in the results, the number of data points used are larger than 1×10^6, with the exception of the case at Re_λ=237 with Gaussian smoothing, for which we have $\approx 8.5 \times 10^5$ data points. Table 4.2 show the exact values for each mean flow.

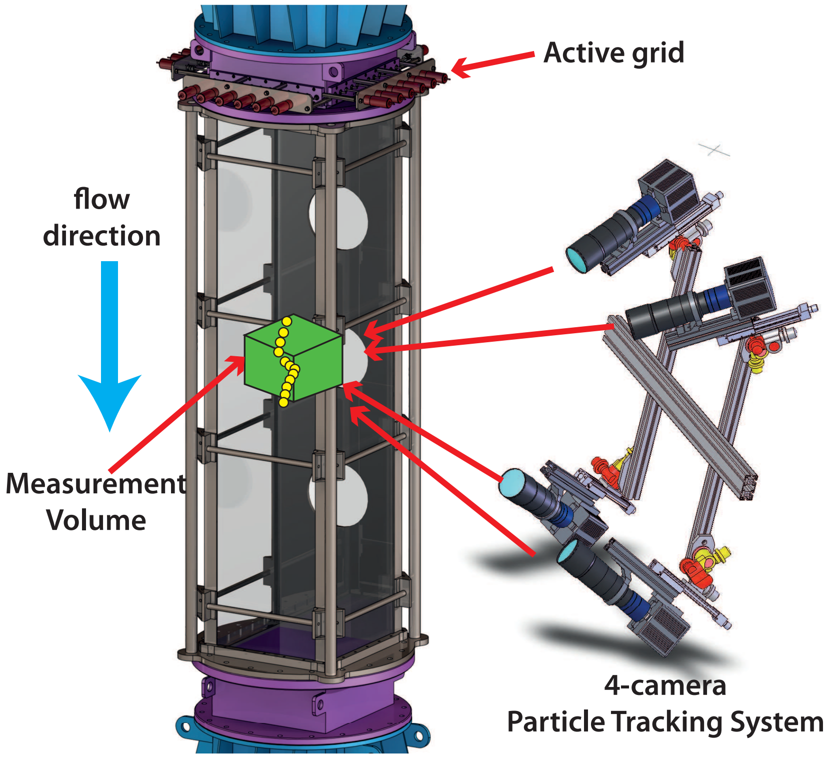

Figure 4.1: The Twente Water Tunnel: an experimental facility for studying two-phase turbulent flows. The picture shows the measurement section, on top of it the active grid which allows homogeneous and isotropic turbulent flows up to $\mathrm{Re}_\lambda = 300$, and the 4-camera particle tracking velocimetry (PTV) system to detect the positions of particles in three-dimensions. For illumination we use a high energy, high-repetition rate laser. Micro-bubbles with a diameter $\approx 340\ \mu$m are generated above the active grid, a ceramic porous plate. They are advected downwards into the measurement volume.

Table 4.1: Summary of the flow parameters. V_{mean}: the mean flow velocity, $\mathrm{Re}_\lambda = u_{rms}\lambda/\nu$, u_{rms}: mean velocity fluctuation, $\eta = (\nu^3/\varepsilon)^4$ and $\tau_\eta = (\nu/\varepsilon)^2$ are the Kolmogorov's lengthscale and timescale respectively, L: integral length scale, $\varepsilon = 15\nu u_{rms}^2/\lambda^2$: mean energy dissipation rate, and $St = \tau_p/\tau_\eta$.

V_{mean} $\mathrm{m\,s^{-1}}$	Re_λ	u_{rms} $\mathrm{m\,s^{-1}}$	η $\mu\mathrm{m}$	τ_η ms	L m	λ m	ε $\mathrm{m^2\,s^{-3}}$	St
0.22	140	0.0161	373	139.5	0.064	8.5e-3	51.4e-6	0.023
0.33	162	0.022	288	83.1	0.054	7.1e-3	144.7e-6	0.039
0.45	174	0.028	242	58.7	0.056	6.3e-3	290.6e-6	0.055
0.57	201	0.035	205	42.1	0.058	5.7e-3	563.3e-6	0.076
0.65	237	0.044	180	32.2	0.07	5.4e-3	961.9e-6	0.1

Table 4.2: Number of data points used to calculate the Lagrangian statistics using a polynomial and Gaussian kernel smoothing for the different Re_λ.

Re_λ	Number of data points	
	Polynomial	Gaussian
140	5.5×10^6	3.4×10^6
162	9.4×10^6	4.7×10^6
174	8.3×10^6	3.1×10^6
201	6.5×10^6	2.4×10^6
237	4.5×10^6	0.85×10^6

4.2.1 Smoothing methods for particle trajectories

In this section, we conduct an extensive study on the methods usually used for smoothing particles' trajectories obtained with PTV in turbulence. Experimental errors in the determination of the particle position are unavoidable, and obtaining the particle velocity and acceleration through a time differentiation of its position is very sensitive to these errors. Hence, a smoothing of the particle trajectory has to be carried out. This smoothing process is a trade-off between filtering out the experimental noise while still being able to keep the inherent turbulent features of the particle motion. Therefore, the smoothing parameters must be very carefully selected.

Historically, there have been two methods for smoothing particle trajectories in turbulent flows. One method consists of fitting the trajectory to a polynomial of second order or higher. Voth *et al.* [2] used a second-order polynomial, Lüthi *et al.* [21] used a third-order polynomial. Some other groups instead have used a Gaussian kernel for smoothing [3, 10, 11]. Our goal is to compare these two completely different methods in detail, a task which surprisingly has not been reported before in the literature. If both methods deliver the same kind of Lagrangian statistics of the micro-bubbles, that would mean that what we are measuring is most likely the true feature of the signal and not an artifact of the smoothing method.

Poynomial fitting: cubic spline

The entire signal of the trajectory $x(t)$ is low-pass filtered by fitting a third-order polynomial, using a fitting window with the particle positions from $t - N\mathrm{d}t$ until $t + N\mathrm{d}t$:

$$x_{i,f}(t) = c_{i,0} + c_{i,1}t + c_{i,2}t^2 + c_{i,3}t^3. \tag{4.1}$$

The Lagrangian velocity and acceleration are obtained by differentiating the particle trajectory:

$$u_{i,f}(t) = c_{i,1} + 2c_{i,2}t + 3c_{i,3}t^2, \tag{4.2}$$

$$a_{i,f}(t) = 2c_{i,2} + 6c_{i,3}t. \tag{4.3}$$

The time window ($t - N\mathrm{d}t$, $t + N\mathrm{d}t$) has to be chosen properly so that the cut-off frequency is larger than that of the typical turbulent time scale.

Gaussian kernel

In this case, a filter using a weight average by considering several points is used to reduce the noise. A Gaussian kernel gives the weighing, and it is given by:

$$k_x(\tau) = \frac{1}{\sqrt{\pi}w}\exp\left(\frac{-\tau^2}{w^2}\right), \tag{4.4}$$

where w is the width or standard deviation of the kernel. The filtered trajectory is obtained by convoluting the kernel with the raw trajectory as:

$$x_f = k_x(\tau) \star x, \tag{4.5}$$

where $\star$ denotes the convolution $k_x \star x = \int_{-\infty}^{\infty} x(t-\tau) k_x(\tau) \mathrm{d}\tau$. If the Gaussian kernel is derived once, then the velocity kernel is obtained,

$$k_v(\tau) = \frac{\tau}{\sqrt{\pi} w} \exp\left(\frac{-\tau^2}{w^2}\right) + B_v. \tag{4.6}$$

With a second differentiation, the acceleration kernel is available,

$$k_a(\tau) = A_a \left(\frac{2\tau^2}{w^2} - 1\right) \exp\left(\frac{-\tau^2}{w^2}\right) + B_a. \tag{4.7}$$

The constants B_v, A_a and B_a are calculated by imposing the following conditions,

$$k_a \star 1 = 0 \qquad k_a \star \tau^2 = 2, \tag{4.8}$$

where the first and the second conditions require the second derivative of a constant to be zero and that of a parabola to be 2, respectively.

Since the experimental particle trajectories are finite, the convolution is restricted to $\int_{-T}^{T}$ instead of $\int_{-\infty}^{\infty}$. In this case, the time window $(-T\ ,\ T)$ used for the filtering should also be smaller than the typical time scale of the flow. Contrarily to the polynomial fitting, the Gaussian kernel method requires two parameters, the time window $(-T\ ,\ T)$ and the width of the kernel w. Ouellete [22] suggested values for these two parameters. He carried out experiments in a von Kármán type of flow, and used following criteria : $(2T+1) \approx \tau_\eta$ and $w = T/1.5$.

Choice of the smoothing parameters

The choice of the time window for smoothing of the polynomial and Gaussian methods determine the statistics of the trajectories. Therefore, it is necessary to explore the effect of this parameter on the statistics of the micro-bubble velocity and acceleration. In this section, we present results corresponding to the dataset at Re_λ=162.

We study firstly the effect of the length of the fitting window on the velocity statistics. As explained above, the polynomial fitting has only one parameter, the length of the fitting window N_{points}, while the Gaussian smoothing has two, the length of the fitting window T and the width of the Gaussian kernel w. For the analysis presented below and for the Gaussian smoothing, we show only the effect of varying w for a fixed window length T=130 points, which when normalized with the time scale τ_η=83.1 ms at Re_λ=162 , gives T/τ_η=0.156. With this value, we ensure to

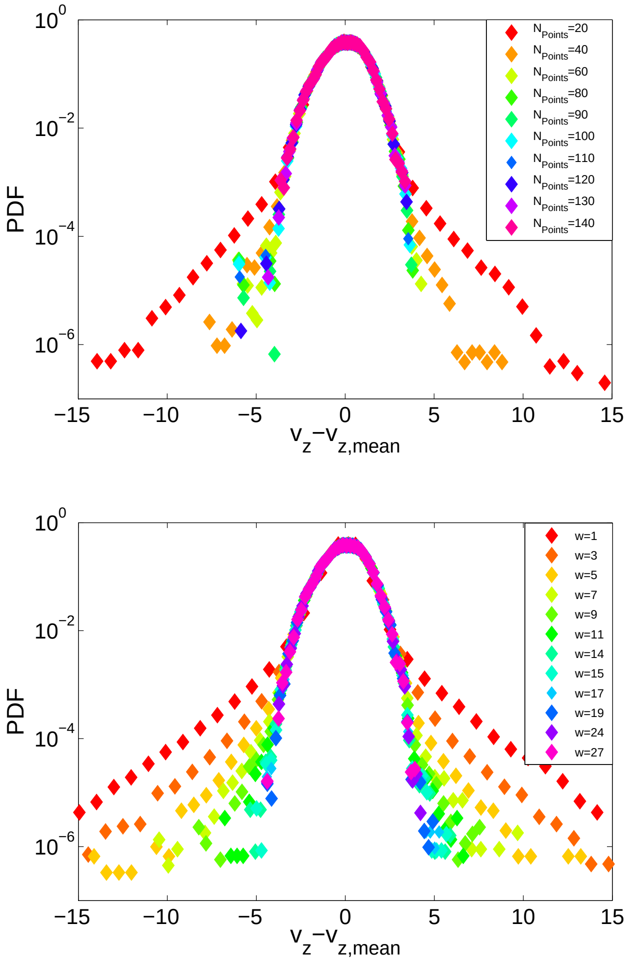

Figure 4.2: PDF of the vertical component of the micro-bubble velocity as a function of the smoothing parameter for Re_λ=162. (a) Polynomial fitting: varying the length of the time window N_{points} from 20 to 140 points, (b) Gaussian kernel for a fixed time window $T = 130$ points, while varying the width of the kernel w from 1 to 27 points. A similar effect for both methods can be observed. For small values of the parameters, the smoothing methods fails and the experimental noise is not removed resulting in a non-Gaussian distribution, whereas for large values there is an over-smoothing, though a Gaussian distribution is recovered.

resolve the smallest time scale in the flow. If we consider the suggestion that $(2T + 1) \approx \tau_\eta$ in [22], this will require for the present work T=430 points, which is rather a large value for our case and would lead to the selection of very long trajectories, thus biasing the results to the dynamics of slow events. We have realized that the above suggestion is flow dependent, i.e. suitable for zero mean flows but not the optimal for turbulence with strong mean flows as in grid-generated turbulence. We selected the value of T=130 points based on a study of the effect of this parameter on the Lagrangian statistics and found it optimal for our experimental conditions. For the following analysis we focus only on the effect of varying w.

Figure 4.2a shows the effect of the length of the time window on the PDF of the vertical component of the micro-bubble velocity for polynomial smoothing. One can observe that for a small number of points $N_{points} < 30$, the distribution has non-Gaussian features. The method thus fails and the experimental error in the position determination cannot be filtered out. By increasing the length of this time window, the PDF recovers a Gaussian distribution as it should on large scales. This shape is maintained up to the largest values of the time window, but with a cost of over-smoothing. For these values of N_{points} the tails of the distribution have shrunk. Figure 4.2b shows the PDF of the vertical component of the micro-bubble velocity obtained with a Gaussian kernel. Similar behavior is observed as for the polynomial smoothing. For small values of w the distribution is noisy and far from having a Gaussian distribution. When increasing the width of the kernel the distribution becomes Gaussian, but over-smoothed for the largest values of w.

The correct selection of the smoothing parameters can be more easily determined by looking at the statistics of the micro-bubble acceleration. The ideal case would be that the statistics along the particle trajectories are independent of the choice of the parameter. We have already seen that it is not the case for the velocity. If we calculate the standard deviation a_{rms} of the micro-bubble acceleration PDFs, we can observe that this value strongly depends on the choice of the fit interval and on the width of the Gaussian kernel. The dependence of a_{rms} on the fitting interval for polynomial and Gaussian smoothings is shown in figures 4.3a and 4.3b at Re_λ=162. For values of $N_{points} < 20$, the standard deviation increases in an exponential manner. For values of $N_{points} > 150$ the a_{rms} reduces considerably as an effect of the over-smoothing. Figure 4.3b shows the a_{rms} as a function of the width of the kernel for a fixed time window of $T = 130$ points. The small values of a_{rms} are also observed for values larger than $w > 35$ while the exponential increment of the standard deviation occurs for values $w < 10$.

As many authors have reported [2, 3], there is not a well defined criteria for the choice of this parameter. Though, the selection of the value must ensure that the time fitting window is smaller than the smallest time scale of the flow, and that it does not fail in averaging the noise (e.g. selecting small values of N_{Points} or w) or that it does

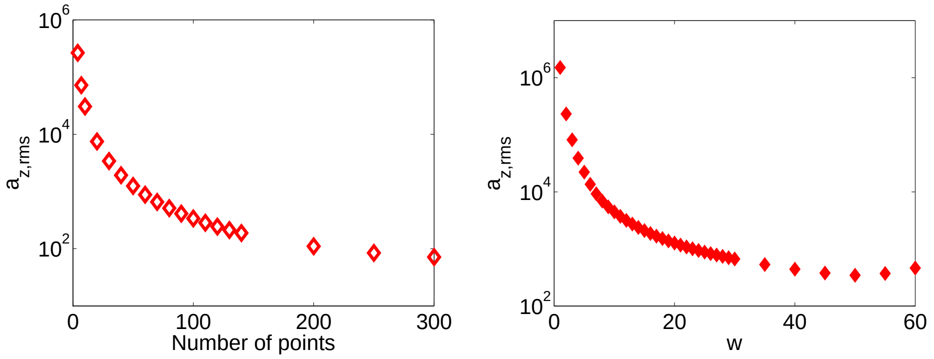

Figure 4.3: Root mean square (r.m.s.) values of the vertical component of the micro-bubble acceleration PDF at Re_λ=162 as a function of (a) the time window for polynomial smoothing N_{points} (◇), (b) the width of the Gaussian kernel w (♦).

not suppress and filters out the turbulent features of the signal (e.g. selecting too large values of N_{Points} or w). For the data presented in this work we have chosen a value of $N_{points} = 45$ for the polynomial fitting. Normalized with the turbulent time scale τ_η=83.1 ms at Re_λ=162, this gives N_{points}/τ_η=0.055. For the Gaussian smoothing, the choice of the width is $w = 22$ with w/T=0.17. We observed that for the largest Re_λ=174, 201 and 237, the optimal fitting window for polynomial smoothing was $N_{points} = 50$, which gives closer values of the standard deviation of the acceleration only. It tis important to point out that the shape and intermittency of the acceleration PDFs for these two values of N_{points} are very similar.

The final test is to compare the results with this choice of the parameters for both smoothing methods among each other. If we obtain similar statistics of the micro-bubble velocity and acceleration with both methods, which are very different in nature, we are likely to reproduce the true statistics of the trajectories.

Comparison of both methods

The comparison of the micro-bubble velocity and acceleration PDFs obtained with both smoothing methods is illustrated in figures 4.4a and 4.4b for Re_λ=162, respectively. For the velocity PDF, one can observe that both the polynomial and the Gaussian kernel method result in a Gaussian distribution for the velocity. On the other hand, the acceleration PDF is extremely non-Gaussian. The shape and intermittency of the acceleration PDF are very well reproduced. This result is worthwhile to be pointed out as both smoothing algorithms are mathematically different. Furthermore, not only the shape of the PDF is similar, but also the values of the standard deviation of the micro-bubble acceleration is very close to each other: for the Gaussian

Table 4.3: Comparison of the standard deviation of the micro-bubble velocity and acceleration for all Re_λ with both smoothing methods. A value of $T = 130$ and $w = 22$ points for the fitting window and width of the Gaussian kernel was used. For the polynomial fitting the fitting window has $N_{points} = 45$ for Re_λ= 140 and 162, and $N_{points} = 50$ for Re_λ= 174, 201 and 237. In the table the column are labeled with G for Gaussian and P for polynomial.

Re_λ	$\mathrm{v}_x\,\mathrm{mms}^{-1}$		$\mathrm{v}_y\,\mathrm{mms}^{-1}$		$\mathrm{v}_z\,\mathrm{mms}^{-1}$		$\mathrm{a}_x\,\mathrm{ms}^{-2}$		$\mathrm{a}_y\,\mathrm{ms}^{-2}$		$\mathrm{a}_z\,\mathrm{ms}^{-2}$	
	G	P	G	P	G	P	G	P	G	P	G	P
140	11.9	12.4	12	12.2	14.6	14.9	1.44	1.26	1.25	1.05	0.85	0.83
162	17	17.7	17.6	17.7	18.5	18.9	1.63	1.51	1.35	1.21	1.08	1.18
174	23	23.8	23.1	23.4	27.3	27.9	1.92	1.64	1.44	1.22	1.39	1.38
201	30.9	31.7	28	28.1	33.9	34	2.12	1.97	1.44	1.45	1.58	1.69
237	33.9	34.6	31.4	31.5	38.2	38.5	2.52	2.16	1.56	1.46	1.84	1.73

smoothing one gets 1.083 m s^{-2}, while for the polynomial the value is 1.185 m s^{-2}. Table 4.3 shows the comparison of the standard deviation of the micro-bubble velocity and acceleration obtained with the two methods. One can see that for both the velocity and acceleration and for all components these values are very close. To our knowledge, such a detailed comparison of the two methods has never been reported before.

4.3 Results

4.3.1 Probability density functions of micro-bubble velocity

In this section we present results on the PDFs of micro-bubble velocity obtained by smoothing raw micro-bubble trajectories with a third-order polynomial and with a Gaussian kernel. Figure 4.5 shows the PDF of the three components of micro-bubble velocity for both filtering methods at $\mathrm{Re}_\lambda = 162$. One can observe that the velocities distributions of the three components are Gaussian and that the results are independent of the smoothing method.

The next step is to investigate the effect of the turbulence intensity on the PDF of micro-bubble velocity. We present the result of the vertical component v_z as it was shown above that the other two horizontal components have similar shape. Figure 4.6a shows the PDFs for all Re_λ obtained by a Gaussian smoothing, whereas figure 4.6b shows the results of a polynomial fitting. For all cases the distributions are nearly Gaussian. Only for one experimental dataset ($\mathrm{Re}_\lambda = 201$) there is a slight deviation from Gaussianity as observed in the tails of the distribution and also re-

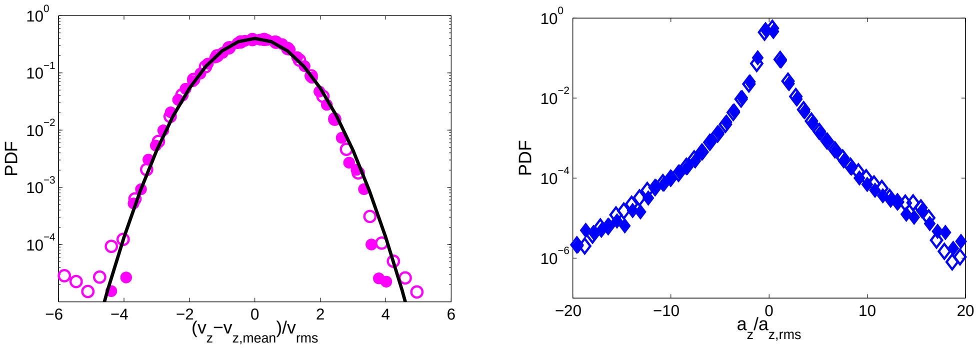

Figure 4.4: Comparison of the smoothing methods for data measured at $\mathrm{Re}_\lambda = 162$. Filled symbols show the results of a Gaussian smoothing, whereas opened symbols result from third-order polynomial fitting. (a) PDF of the vertical component of micro-bubble velocity. The PDFs are nearly Gaussian as it can be compared with the solid line representing a Gaussian distribution. An even better comparison of the smoothing methods can be achieved with the acceleration PDF, as it is a second-order derived quantity and more sensitive to the choice of the parameter, here shown in (b). Remarkably, both methods predict similar shape and intermittency level of the micro-bubble acceleration.

flected in table 4.4.

A calculation of the flatness F of these PDFs gives values very close to that of a Gaussian distribution F=3. The flatness of the vertical component of the velocity shows a sub-Gaussian distribution for all mean flows and for both smoothing methods, again with the only exception of the case at $\mathrm{Re}_\lambda = 201$, for which the flatness has a value above 4. We have double checked the analysis on this specific data set and we even recalculated the results with no difference. We do not have further clue on the origin of this difference, though.

Gaussian-type flatness values have also been reported in experiments with turbulent von Kármán flows. Voth *et al.* [2] measured velocity distributions close to Gaussian with flatness values in the range 2.8−3.2, and Volk *et al.* [10] obtained even sub-Gaussian distributions with flatness around 2.4−2.6.

4.3.2 Probability density functions of micro-bubble acceleration

Contrary to the velocity case, the PDFs of the micro-bubble acceleration, normalized with its standard deviation (a/a_{rms}),exhibit a strong non-Gaussian behavior. Figure 4.7 shows the PDFs for all the components of the micro-bubble acceleration obtained with the two filtering methods for $\mathrm{Re}_\lambda = 174$. We can observe from the figure, that

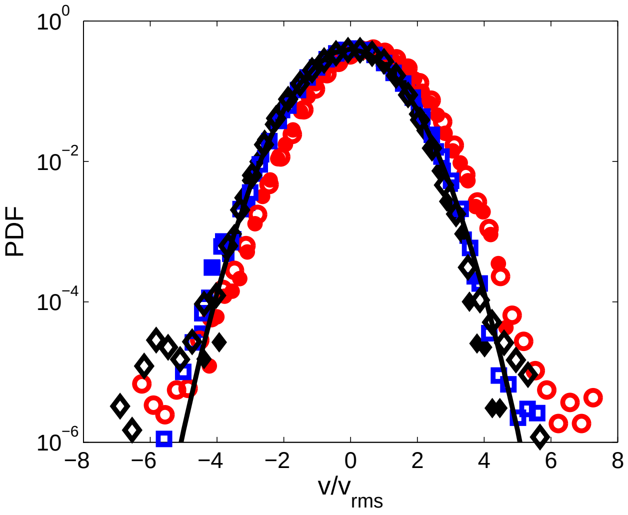

Figure 4.5: PDFs of the three components of micro-bubble velocity at $\mathrm{Re}_\lambda = 162$: v_x (●), v_y (■), v_z (◆). The data obtained by a Gaussian kernel smoothing is shown with filled symbols, opened symbols represent data filtered with a polynomial fitting. The distributions of the three components are nearly Gaussians as compared with the solid line that represents a Gaussian distribution. The shape of the distribution is independent on the method.

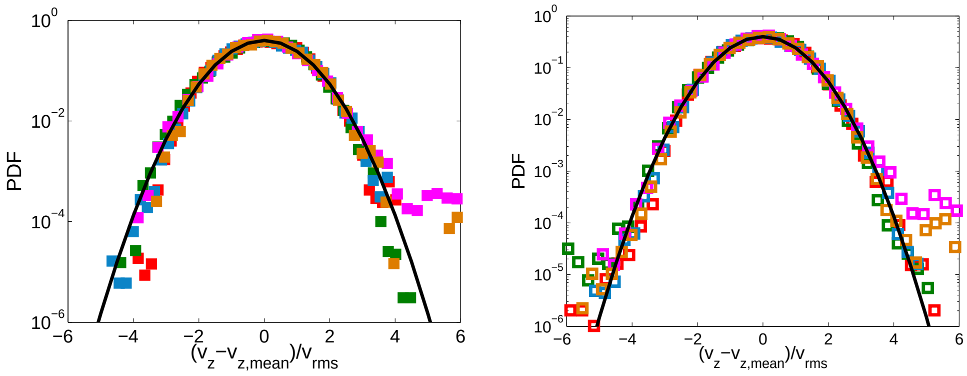

Figure 4.6: PDFs of the vertical component of the micro-bubble velocity for different Re_λ, (a) Gaussian kernel, (b) polynomial fitting. For all turbulent intensities the distributions are nearly Gaussian independent on the method. The color represents different turbulence intensities: Re_λ=140 (🟥), Re_λ=162 (🟩), Re_λ=174 (🟦), Re_λ=201 (🟪), Re_λ=237 (🟧).

Table 4.4: Flatness values of the distribution of micro-bubble velocities for both smoothing methods. G and P denote results obtained either with Gaussian kernel or with polynomial fitting.

Re_λ	v_x		v_y		v_z	
	G	P	G	P	G	P
140	3.03	3.19	3.15	3.19	2.7	2.79
162	3.01	3.09	2.99	3.08	2.9	2.96
174	3	3.13	3.01	3.07	2.75	2.87
201	2.9	3.04	2.95	3.03	4.82	4.3
237	2.85	2.96	3	3.01	3.06	2.94

the acceleration PDFs are highly intermittent as the probability of rare non-Gaussian events is much higher than a normal distribution, i.e. the tails of the PDFs extend beyond $15\,a_{rms}$. We also show that both filtering methods give similar distributions of the acceleration, thus reflecting the true statistics along the micro-bubble trajectories. At this Re_λ the acceleration is quite isotropic as the PDFs of the three components match. We have observed this trend for the higher Re_λ, whereas for smaller ones the horizontal components of the acceleration (a_x, a_y) are not yet isotropic. The tails of the PDFs for these components of the acceleration are slightly narrower and less intermittent than the vertical component.

We also investigate the effect of the turbulence intensity on the shape and intermittency of the acceleration PDFs. In figure 4.8, the PDFs of all components of the micro-bubble acceleration at different Re_λ are shown for the Gaussian and polynomial smoothing. One major feature is that the shape of the PDFs is nearly independent on Re_λ. This independence is clearer for the vertical component a_z (see figures 4.8c and 4.8e) for which all the curves collapse. For the case of the x and y components, this collapse is less prominent at the smallest values of $Re_\lambda = 140, 162$ due to the anisotropy of the acceleration at these “slow” mean flows. From the two horizontal components, the PDFs of a_y show the larger difference of shapes and intermittency with Re_λ. This can be explained as the effect of the error in the determination of the position along this component. The y-component is in fact the in-depth component referenced to the camera coordinates. The error along this direction is for every PTV system larger compared to the in-plane directions. Both smoothing methods reproduce satisfactorily the statistics of the acceleration and give comparable results:

- the PDFs of a_z coincide for all Re_λ
- the PDFs of the horizontal components of the acceleration are less intermittent for $Re_\lambda = 140$ and162. The largest difference can be observed for a_y.

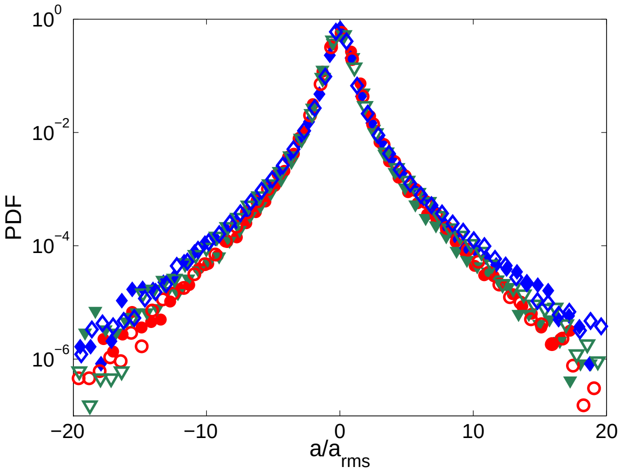

Figure 4.7: PDFs of the three components of the normalized micro-bubble acceleration at $\mathrm{Re}_\lambda = 174$: a_x (●), a_y (▼), a_z (♦). The data obtained by a Gaussian kernel smoothing is shown with filled symbols, opened symbols represent data filtered with a polynomial fitting. The three components of the acceleration show strong non-Gaussian effects, i.e. the tails of the distribution are highly intermittent. At this Re_λ the isotropy of the flow is well observed, for smaller Re_λ the distribution of the horizontal components (a_x, a_y) is a bit less intermittent and their tails are narrower. It is worthwhile to notice that both methods give similar distributions and values of the standard deviation of the acceleration.

Finally, we present jointly in figure 4.9 the PDFs of the vertical component of the acceleration for all the studied mean flows and for both smoothing algorithms. Remarkably, the shape of all the PDFs coincide, proving that the micro-bubble acceleration is highly intermittent.

4.3.3 Acceleration PDFs: comparison with numerics and experiments

The next step is to compare our experimental acceleration PDFs with numerical simulations and with experiments. In figure 4.10, the comparison between our work and other numerical simulations and experiments is presented. Figure 4.10a compares our experimental results with numerical ones. We have used data from [23] for bubble and fluid tracers simulations at a similar Re_λ=180. We observe that the intermittency of the PDF of the experimental micro-bubbles is in between the behavior of numerical bubbles and tracers. We understand this as an effect of the size of the particle, i.e. of the Stokes number in the experiments the St is one order of magnitude smaller than that of the numerical bubbles.

Figure 4.10b shows the comparison with experiments. We have used the data of Ayyalasomajayula *et al.* [11], who did experiments with heavy particles in a wind tunnel with St=0.15 and similar Reynolds number of Re_λ=250, and the data of Voth *et al.* [2] who used neutral bouyant particles in a von Kármán flow at Re_λ=200. We observe that indeed the experimental acceleration PDF of micro-bubbles is more intermittent with wider tails than for heavy particles with similar Re_λ. However, the present results for micro-bubbles have similar intermittency compared to the tracer data of Voth *et al.*, reflecting the small St of our bubbles. More experiments with fluid tracers in the actual experimental setup are needed to give a definite conclusion.

4.3.4 Intermittency of the micro-bubble acceleration

In order to quantify the intermittency of the acceleration PDFs, statistical convergence of the distributions is necessary. The number of data points needed for this convergence is crucial, and previous studies have shown that at least it should be of order 10^6 [2, 8, 9, 11]. As shown in table 4.2, our datasets consist of at least 10^6 points, with the exception of the case with Re_λ=234 filtered with a Gaussian kernel, for which we only have $\approx 8.5\times10^5$. In figure 4.11, we plot the fourth order moment $a^4 PDF(a)$ for the three components of the acceleration at Re_λ=162. At large values of the normalized acceleration —i.e. tails of the distribution— convergence of this moment is achieved. The fourth order moment goes down to zero independent of the smoothing algorithm used, as shown in figure 4.11. The same behavior is also observed for the other measurements at different Re_λ.

To quantify the intermittency of the PDFs of the micro-bubble acceleration, we

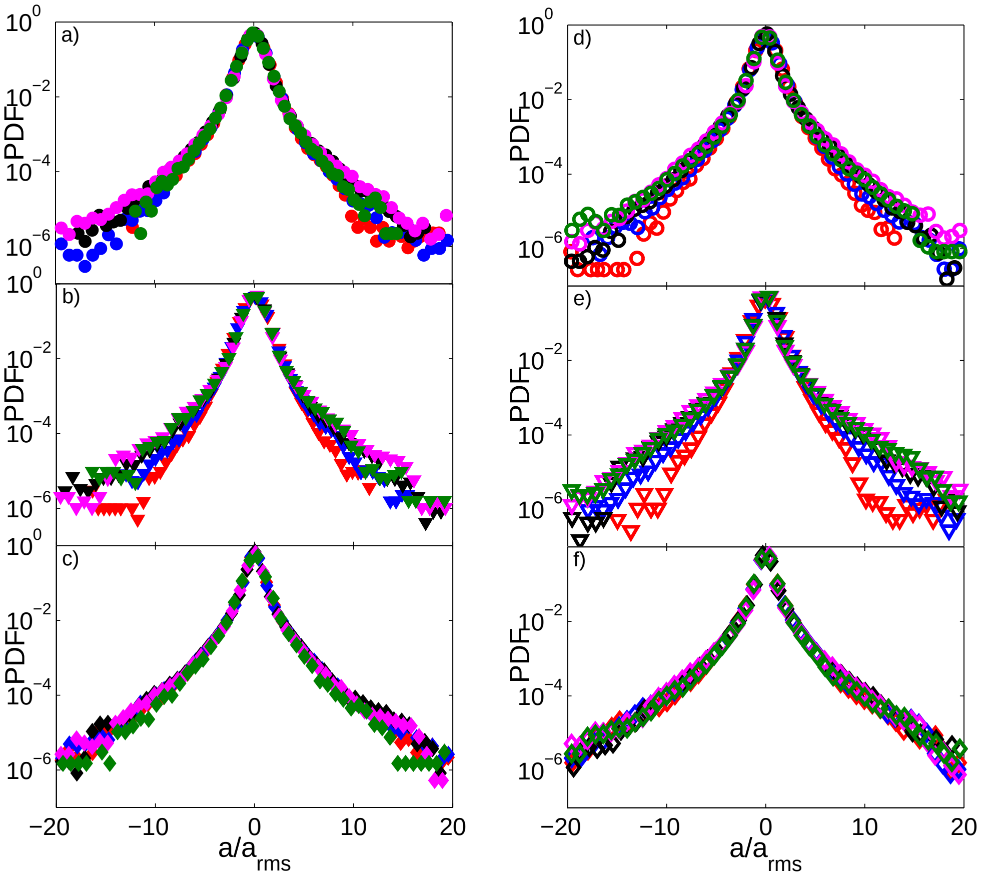

Figure 4.8: PDFs of the three components of the normalized micro-bubble acceleration for all Re_λ. Filled symbols correspond to data filtered with a Gaussian kernel (figures a,b,c), opened symbols to that obtained by a polynomial fitting (figures d,e,f). The components of the acceleration are represented by: $a_x \circ$, $a_y \bigtriangledown$, $a_z \diamondsuit$. The color represents different turbulence intensities: Re_λ=140 (●), Re_λ=162 (●), Re_λ=174 (●), Re_λ=201 (●), Re_λ=237 (●).

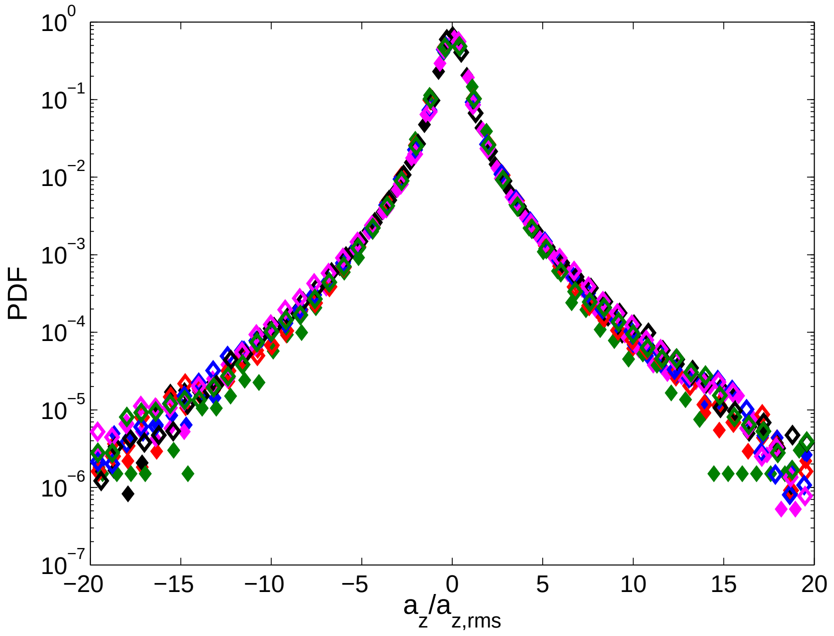

Figure 4.9: PDFs of the vertical component of the micro-bubble acceleration for all Re$_\lambda$ obtained with the two smoothing methods. Filled symbols correspond to a Gaussian smoothing, opened symbols to a polynomial fitting. All curves collapse reflecting the intermittency of the micro-bubble's acceleration. The color represents different turbulence intensities: Re$_\lambda$=140 (♦), Re$_\lambda$=162 (♦), Re$_\lambda$=174 (♦), Re$_\lambda$=201 (♦), Re$_\lambda$=237 (♦).

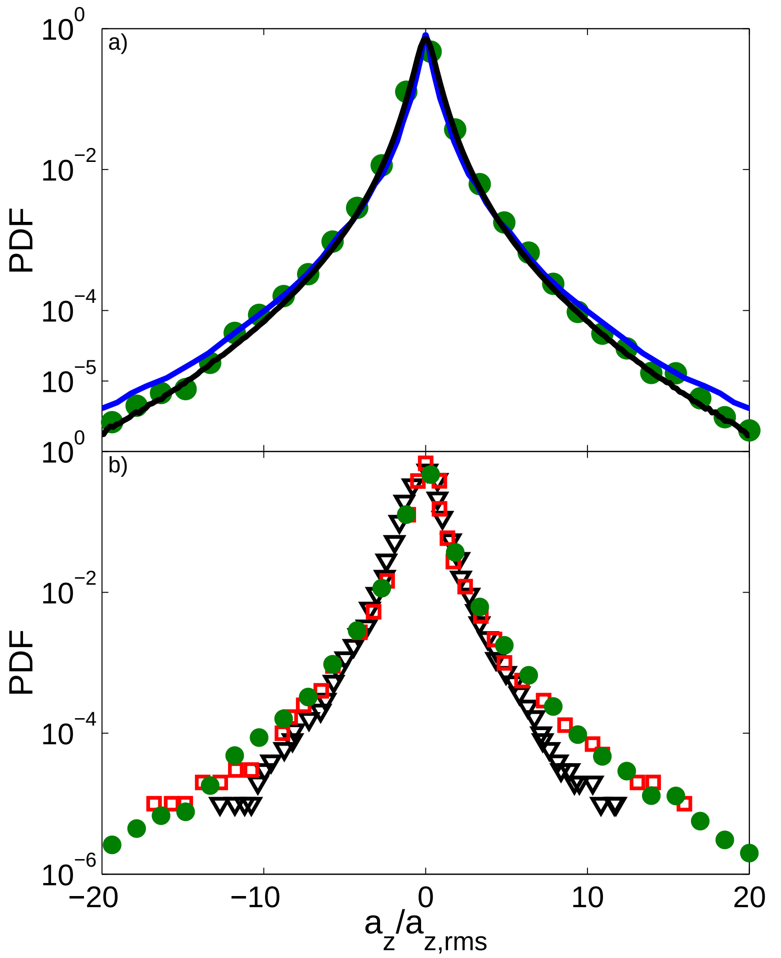

Figure 4.10: Comparison of the PDF of the vertical component of the micro-bubble acceleration at Re_λ=162 with: (a) point-particle DNS [23] and (b) with experiments. Only the result of the Gaussian smoothing is shown. In the upper figure: (●) experimental data, blue solid line corresponds to DNS of bubbles whereas the black solid line to DNS of fluid tracers. The simulations were performed at Re_λ=180. The central part of the experimental PDF agrees well with the numerical bubbles. The tails match slightly better that of DNS point-like tracers. In the lower figure: micro-bubbles of the present work (●), heavy particles in a wind-tunnel at Re_λ=250 [11] (▽) and fluid tracers in a von Kármán flow at Re_λ=200 [2] (□). The PDF of heavy particles is less intermittent than for the micro-bubbles. The PDF of fluid tracers show a similar intermittency than micro-bubbles, reflecting the small St O(0.01) of our bubbles.

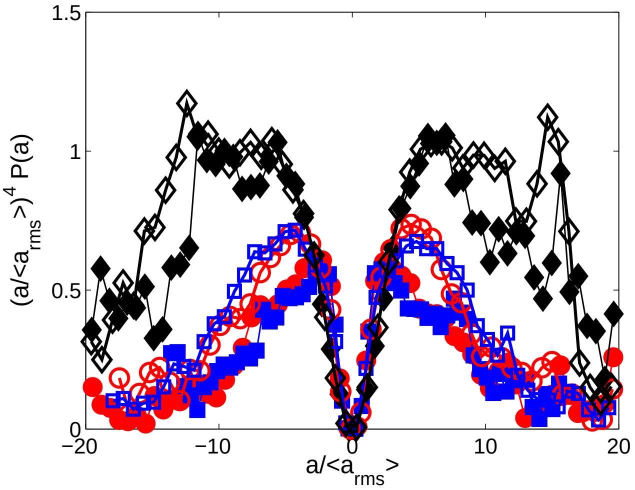

Figure 4.11: Convergence of the fourth order moment of the acceleration at Re$_\lambda$=162. The different components of the acceleration are: a$_x$ (●), a$_y$ (■) and a$_z$ (♦). Results obtained by a Gaussian smoothing are shown with filled symbols, for polynomial smoothing opened symbols are used.

carry out a study of their flatness F:

$$\mathrm{F} = \mu_4/\sigma^4, \tag{4.9}$$

where μ_4 is the fourth moment and σ the standard deviation of the distribution. Since the flatness is a fourth order moment, it is strongly determined by the tails of the distribution, hence convergence of the PDFs is required. Even though the number of data points used to calculate the PDFs in the present work is larger than O(10^6), full convergence has not yet been achieved to calculate directly the flatness from the distribution itself (the largest experimental datasets consists of 10^8 points [3], whereas for numerics this value can go up to 10^9 [5]). Our approach is in consequence to fit the experimental PDF to two different functions: a stretched exponential distribution proposed in [3, 24] and a log-normal distribution proposed in [4], whose definitions are as follows:

$$f_{se}(a) = C\exp\left(\frac{-a^2}{2\sigma^2(1+|\frac{\beta a}{\sigma}|^\gamma)}\right), \tag{4.10}$$

$$f_{ln}(a) = \frac{\exp(3s^2/2)}{4\sqrt{3}}\left(1-\mathrm{erf}\left(\frac{\ln|x/\sqrt{3}|+2s^2}{s\sqrt{2}}\right)\right). \tag{4.11}$$

In equation 4.10, the fitting parameters are σ, β and γ and C is a normalization constant, while in equation 4.11 only s has to be fitted. As suggested in [10], we also choose the distance to minimize as: $a^2\mathrm{PDF}_{exp} - a^2 f(a)$, where $a = \mathrm{a}/\mathrm{a}_{rms}$ is the normalized micro-bubble acceleration, PDF_{exp} the experimental measured PDF and $f(a)$ is either the stretched exponential or log-normal functionals. For this fitting procedure and in order to improve the convergence at the tails, we have taken the absolute value of the acceleration vector. Thus, considering only a symmetrical positive part of the PDF. Figure 4.12 shows the results of the fitting for the PDFs of the vertical component of the micro-bubble acceleration obtained by a Gaussian and polynomial smoothing at Re_λ=162. The solid lines in the figure correspond to the fitting using equation 4.10, the curves fit the experimental PDFs for both smoothing algorithms quite well. Oppositely, when using a log-normal functional (equation 4.11) the fits do not resemble the experimental PDFs as shown with the dashed lines in that figure. Here one must consider that the log-normal functional has only one fitting parameter. Small normalized accelerations close to zero are more probable, and thus have a higher weighing than the tails. A functional such as the stretched exponential in equation 4.10, can very nicely fit the experiments as there are three parameters for adjusting. Due to its better performance, we calculate the flatness values of the acceleration PDFs by fitting the measured distributions using only the stretched exponential model.

In figure 4.3, it has been shown that the standard deviations of the acceleration PDFs depend strongly on the smoothing parameters: for large values of the filtering window the signal is heavily smoothed out, while for small values the experimental noise is kept. As a consequence, to estimate correctly the flatness values of the PDFs it is necessary to calculate the flatness of the PDFs for all values of the smoothing parameter. The value of the flatness will be the extrapolated value at zero number of points of the fitting window (as for polynomial smoothing) or at zero-width of the Gaussian kernel (see the discussion in [2]). This extrapolation to zero-width can be understood as follows: for a small fitting window the smoothing algorithms fail, thus the experimental noise in the position detection can not be filtered out. However, for larger yet moderate fitting windows the smoothing indeed is able to reduce the noise level preserving still the features of the acceleration. In such a way, if there were no experimental noise and the smoothing algorithm performed well with small fitting windows, the flatness value extrapolated to the zero-width would be the flatness of the distribution.

In figures 4.13a and 4.13b, the flatness value as a function of the fitting window length is shown for the Gaussian and polynomial smoothing at Re_λ=162, respectively. As mentioned above the flatness is calculated for the stretched exponential distributions fitted to the experimental PDFs. One can clearly see a non-monotonic increasing trend of the flatness for a decreasing fitting window. At very small values of the smoothing window, the flatness drops down as a result of the known bad performance of the method in these region. By extrapolating the value of the flatness to

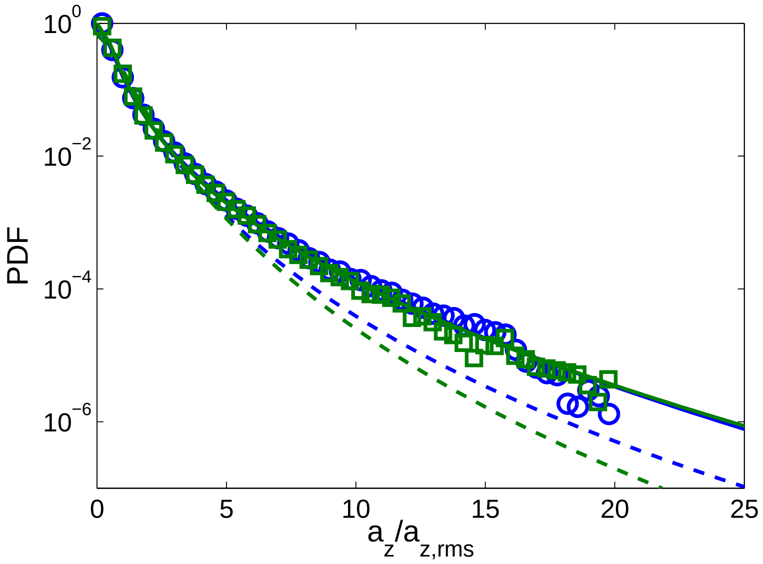

Figure 4.12: Fitting curves of the PDFs of the vertical component of the micro-bubble acceleration at Re_λ=162 for Gaussian and polynomial smoothing. Experimental PDFs: Gaussian (○), polynomial (□). The solid lines are the fit using a stretched exponential function. The dashed lines are the fits obtained using a log-normal distribution. The color of the lines correspond to fits considering data smoothed either with a Gaussian or polynomial algorithm, as for the experimental PDFs.

zero width, both methods give remarkably similar values. For a Gaussian smoothing the flatness is F=35.59 while for the polynomial fitting the value is F=34.27. We can conclude that the PDFs of our experimental micro-bubbles are highly intermittent with an estimated flatness of about 35.

Is the estimated value of the flatness independent of the turbulence intensity? Ideally, we would need to carry out the calculation of the flatness as a function of the fitting window for all Reynolds numbers. Unfortunately we could not carry out extensively such investigation, but in order to have an idea about this behavior, we calculate the flatness for all Re_λ at a fixed value of the fitting parameter: $w = 22$ for Gaussian kernel and $N_{points} = 45$ for the polynomial fitting. These values were the optimal ones used to calculate the velocity and acceleration PDFs (see section 4.2.1) and are shown in figures 4.13a and 4.13b by the arrows. In figure 4.13c we present the flatness for all Reynolds numbers at these fixed values of the smoothing parameter. We can see that the flatness values are nearly constant in these range of Reynolds numbers. Both smoothing methods yield the same behavior. Therefore, we expect that the flatness value should be close to F=35 for all the Re_λ measured.

4.3.5 Autocorrelation functions

We now present the Lagrangian autocorrelation functions of the micro-bubble acceleration. First we compare the autocorrelation for the three components of the acceleration in figure 4.14 at Re_λ=162 and using a dimensionless time lag normalized with the turbulent Kolmogorov time scale τ_η. We show results of both smoothing methods. For the case of a polynomial smoothing, the correlation persists for longer times than for a Gaussian smoothing. It is also important to notice that the three components correlate similarly. This nearly isotropic behavior of the acceleration autocorrelation was also found in the other measurements at different Re_λ.

Figure 4.15 shows the autocorrelation of a_z for different Re_λ and for both smoothing methods. It is clear that the particle's acceleration correlates longer with increasing Re_λ, as a result of the smaller time scales with increasing turbulence. For the polynomial fitting, the trend of longer correlations than for Gaussian smoothing is maintained. The difference between the two methods become bigger with increasing Reynolds number.

The acceleration autocorrelation functions drops off to zero very rapidly. The zero-crossing point occurs before a small value of $0.1\tau_\eta$. Voth *et al.* [2] and Mordant *et al.* [4] reported values of around $2.2\tau_\eta$ in their experiments with tracers, whereas Volk *et al.* [16] reported a zero-crossing point for bubbles around $0.5\tau_\eta$. Those experiments were carried out at higher turbulence intensities ($\mathrm{Re}_\lambda > 690$) and in von Kármán flows.

We study in detail the time at which the autocorrelation functions drop off to zero,

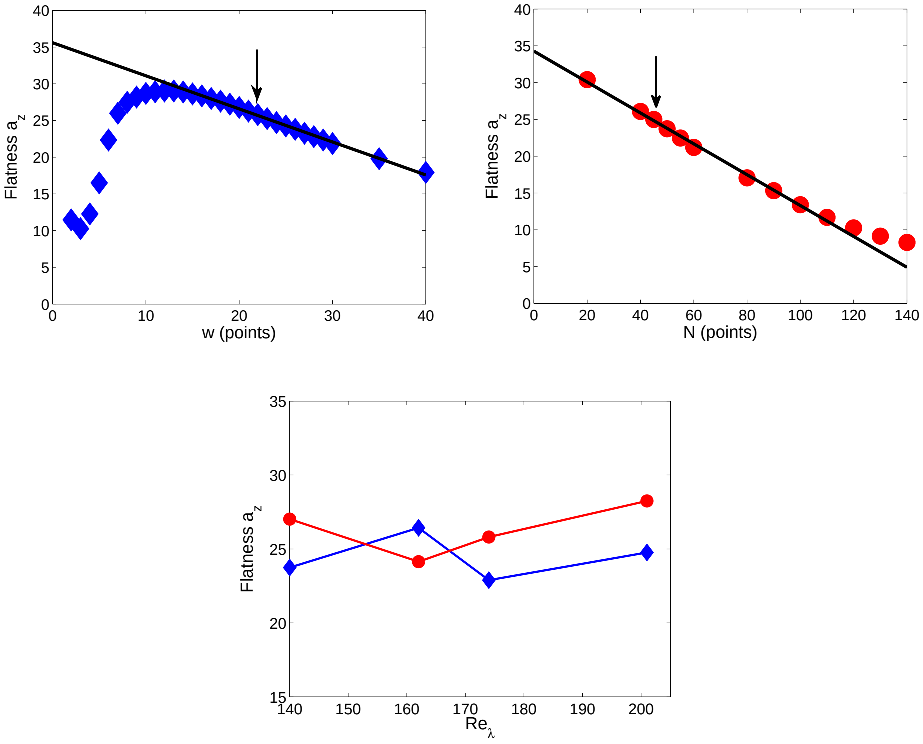

Figure 4.13: Flatness values dependance on the width and number of points considered for smoothing for the a$_z$ PDF at Re$_\lambda$=162 using a stretched exponential functional. Upper figures: Gaussian smoothing (◆) and polynomial smoothing (●). The solid black line shows the extra-polation of the flatness to zero-width or zero-length of the window, respectively. The flatness values are F$_G$=35.59 and F$_p$=34.27. The arrows in the figures correspond to the value of the smoothing parameter used to investigate the Reynolds dependence of the flatness shown in the lower figure. Lower figure: flatness value as a function of Re$_\lambda$ for the a$_z$ PDF at fixed value of the smoothing parameter $w = 22$ and $N = 45$ for Gaussian (◆) and polynomial (●) smoothing, respectively. As we can see from this figure, the flatness value is nearly independent of the turbulence intensity for the range of Reynolds numbers covered.

and define a decorrelation time as:

$$T_D = \int_0^{\tau_0} R_{aa}(\tau) d\tau, \quad \text{with} \quad R_{aa}(\tau_0) = 0,$$

where R_{aa} is the acceleration autocorrelation. Figure 4.16 shows T_D as a function of Re_λ for the three components of the micro-bubble acceleration and for both smoothing methods. We observe that T_D increases with increasing Re_λ, and that the autocorrelation functions are nearly isotropic independent of the turbulence intensity. Furthermore, the polynomial smoothing correlates slightly longer than the Gaussian method. We think that this is an effect of the nature of the method which has a constant weighing for all the points belonging to the fitting window as compared to the weighing obtained if a Gaussian kernel is considered. The maximum variation between the method is of around 28% at Re_λ=237. In spite of this difference at large Reynolds numbers, our results can still give a reasonable estimate of the decorrelation time.

We also compare our experiments with some other experimental work. In the inset of figure 4.16, the decorrelation time T_D as obtained in [16] at Re_λ=850 is shown. That result agrees well with our increasing trend of the decorrelation time with Re_λ. We fit our experimental data of the decorrelation time of a_z to a linear relation for both Gaussian and polynomial smoothing, resulting in: $T_D/\tau_\eta = 0.00036\mathrm{Re}_\lambda - 0.041$ and $T_D/\tau_\eta = 0.00046\mathrm{Re}_\lambda - 0.054$, respectively. These fits are also shown in the inset of figure 4.16 as a solid line for the Gaussian smoothing, and as a dashed line for the polynomial case. Evaluating these relations at Re_λ=850 gives $T_D/\tau_\eta = 0.26$ and $T_D/\tau_\eta = 0.33$ for the Gaussian and polynomial smoothing, which is consistent with their experimental value of $T_D/\tau_\eta = 0.258$. Though more experiments in the unexplored experimental region are needed to study further the real scaling.

Very recently, Volk *et al.* [10] measured T_D for inertial buoyant particles as a function of their normalized size D/η. They found an increasing linear dependence on the particle size. They carried out experiments with different particle sizes and Re_λ. For a fixed size, the increase of T_D with increasing Re_λ was noted, just as we find in our micro-bubble experiments.

4.4 Conclusion

We have presented results on the Lagrangian statistics of micro-bubble velocity and acceleration in homogeneous isotropic turbulence. Three-dimensional PTV was employed to determine the micro-bubble trajectories. For the first time, we report the comparison of two smoothing methods used for filtering out the inherent experimental inaccuracy of the position determination, and show that the these methods yield to similar results and are able to reproduce the turbulent features of the micro-bubbles'

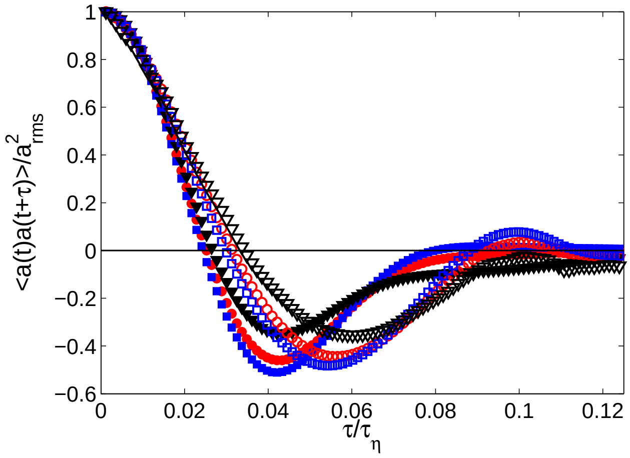

Figure 4.14: Autocorrelation function of the three components of the micro-bubble acceleration at Re$_\lambda$=162. The filled symbols correspond to data obtained by a Gaussian smoothing, opened symbols correspond to that obtained by a polynomial fitting: a$_x$ (●), a$_x$ (■) and a$_x$ (▼). The acceleration autocorrelation of the micro-bubbles is quasi-isotropic. The acceleration vectors obtained by a polynomial smoothing show a slightly longer correlation. The time lag is normalized with the typical turbulent time scale.

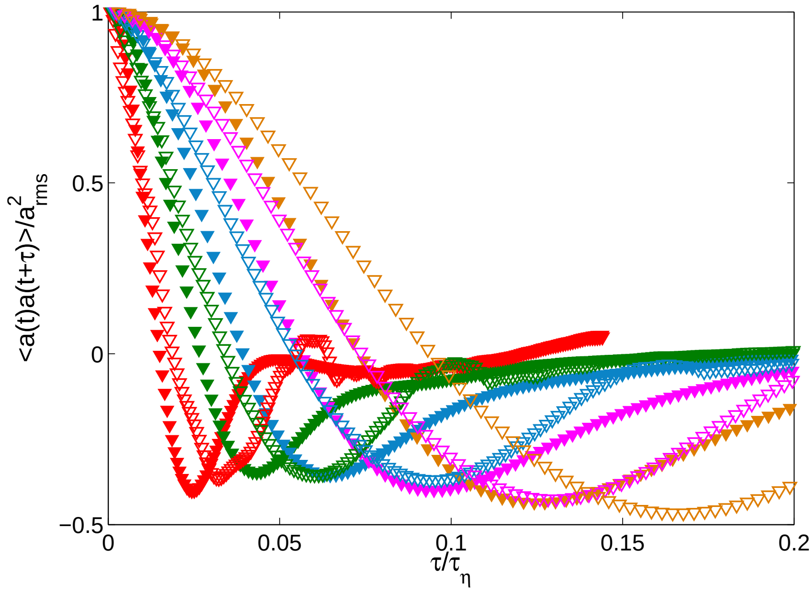

Figure 4.15: Autocorrelation function of the vertical component of the micro-bubble acceleration for the different Re_λ measured. The correlation of the micro-bubble acceleration persists longer with increasing Reynolds number. The data obtained by a polynomial filtering correlates longer as for the Gaussian smoothing. Filled symbols represent data obtained by a Gaussian smoothing and opened symbols that by a polynomial smoothing. Re_λ=140 (▼), Re_λ=162 (▼), Re_λ=174 (▼), Re_λ=201 (▼), Re_λ=237 (▼).

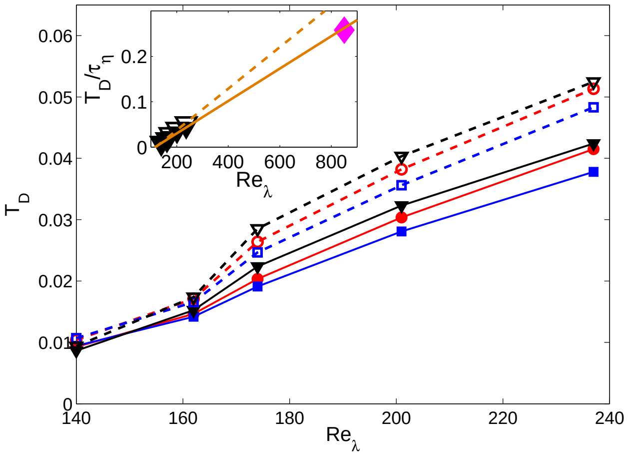

Figure 4.16: The decorrelation time T_D/τ_η of the autocorrelation function for the three components of the micro-bubble acceleration as a function of Re_λ. The decorrelation time increases with the turbulent intensity. The micro-bubble acceleration is nearly isotropic as the three components have very similar decorrelation times. The polynomial filtering gives acceleration signals which correlate longer than those obtained by a Gaussian smoothing: a_x (●), a_y (■) and a_z (▼). A linear fit considering the experimental data of a_z for both Gaussian and polynomial smoothing give: $T_D/\tau_\eta = 0.00036\mathrm{Re}_\lambda - 0.041$ and $T_D/\tau_\eta = 0.00046\mathrm{Re}_\lambda - 0.054$, respectively. In the inset, we show also the result of Volk *et al.* [16] at a very high Re_λ=850 (♦), their experimental point agrees with the trend of increasing decorrelation time with turbulent intensity. The linear fits obtained with our experimental data predict a value of $T_D/\tau_\eta = 0.26$ and $T_D/\tau_\eta = 0.33$ at Re_λ=850 for the Gaussian (solid line in the inset) and polynomial smoothing (dashed line in the inset) respectively, which is comparable to their experimental value of $T_D/\tau_\eta = 0.258$.

trajectories. The PDFs of micro-bubble velocity follow a Gaussian distribution independent of Re_λ with flatness very close to 3. On the other hand, intermittency effects can be clearly seen in the PDFs of micro-bubble acceleration. Their shape is independent of Re_λ, and can be well approximated to a stretched exponential distribution.

Compared to point-particle bubbly DNS simulations, the experimental PDFs of micro-bubble acceleration show slightly less intermittency, the tails of the experimental PDFs match better those of numerical tracers at similar Reynolds numbers. We understand this difference as a St effect, the different intermittency arises from the difference in St. In our case the St are O(0.01), whereas in numerics the St was a factor 10 greater. Indeed, the tails of the PDFs can be very sensitive to the particle size. The flatness of the acceleration PDF calculated from the fitted distributions is around 35, and agrees well with the expected trend of particle's density as other wind tunnel experiments of heavy particles at comparable Re_λ reported $F \approx 8$ [11, 12].

We also calculate the autocorrelation functions of the micro-bubble acceleration. The acceleration decorrelates slower with increasing Re_λ, i.e. the decorrelation time increases with increasing turbulent intensity. This finding is consistent with other experimental investigations [10, 16], but more experimental work is needed to fill the gap of Re_λ for which no data is available and in order to obtain the a scaling relation.

References

[1] F. Toschi and E. Bodenschatz, "Lagrangian properties of particles in turbulence", Annu. Rev. Fluid Mech. **41**, 375–404 (2009).

[2] G. Voth, A. La Porta, A. M. Crawford, J. Alexander, and E. Bodenschatz, "Measurement of particle accelerations in fully developed turbulence", J. Fluid Mech. **469**, 121–160 (2002).

[3] N. Mordant, A. M. Crawford, and E. Bodenschatz, "Experimental lagrangian acceleration probability density function measurement", Physica D **193**, 245–251 (2004).

[4] N. Mordant, A. M. Crawford, and E. Bodenschatz, "Three-dimensional structure of the lagrangian acceleration in turbulent flows", Phys. Rev. Lett. **93**, 214501 (2004).

[5] L. Biferale, G. Boffetta, A. Celani, B. J. Devenish, A. Lanotte, and F. Toschi, "Multifractal statistics of lagrangian velocity and acceleration in turbulence", Phys. Rev. Lett. **93**, 064502 (2004).

[6] I. Mazzitelli and D. Lohse, "Lagrangian statistics for fluid particles and bubbles in turbulence", N. J. of Phys. **6**, 203 (2004).

[7] F. Toschi, L. Biferale, G. Boffetta, A. Celani, B. J. Devenish, and A. Lanotte, “Acceleration and vortex filaments in turbulence”, J. Turb. **6**, 15 (2005).

[8] N. M. Qureshi, M. Bourgoin, C. Baudet, A. Cartellier, and Y. Gagne, “Turbulent transport of material particles: An experimental study of finite size effects”, Phys. Rev. Lett. **99**, 184502 (2007).

[9] R. D. Brown, Z. Warhaft, and G. A. Voth, “Acceleration statistics of neutrally buoyant spherical particles in intense turbulence”, Phys. Rev. Lett. **103**, 194501 (2009).

[10] R. Volk, E. Calzavarini, E. Leveque, and J.-F. Pinton, “Dynamics of inertial particles in a turbulent von Kármán flow”, J. Fluid Mech. **668**, 223–235 (2011).

[11] S. Ayyalasomayajula, A. Gylfason, L. R. Collins, E. Bodenschatz, and Z. Warhaft, “Lagrangian measurements of inertial particle accelerations in grid generated wind tunnel turbulence”, Phys. Rev. Lett. **97**, 144507 (2006).

[12] N. M. Qureshi, U. Arrieta, C. Baudet, A. Cartellier, Y. Gagne, and M. Bourgoin, “Acceleration statistics of inertial particles in turbulent flow”, E. P. J. B **66**, 531–536 (2008).

[13] H. Xu and E. Bodenschatz, “Motion of inertial particles with size larger than kolmogorov scale in turbulent flows”, Physica D **237**, 2095 – 2100 (2008).

[14] J. Bec, L. Biferale, G. Boffetta, A. Celani, M. Cencini, A. Lanotte, S. Musacchio, and F. Toschi, “Acceleration statistics of heavy particles in turbulence”, J. Fluid Mech. **550**, 349–358 (2006).

[15] E. Calzavarini, R. Volk, M. Bourgoin, E. Leveque, J.-F. Pinton, and F. Toschi, “Acceleration statistics of finite-sized particles in turbulent flow: the role of Faxèn forces”, J. Fluid Mech. **630**, 179–189 (2009).

[16] R. Volk, E. Calzavarini, G. Verhille, D. Lohse, N. Mordant, J.-F. Pinton, and F. Toschi, “Acceleration of heavy and light particles in turbulence: Comparison between experiments and direct numerical simulations”, Physica D **237**, 2084 – 2089 (2008).

[17] R. Volk, N. Mordant, G. Verhille, and J.-F. Pinton, “Laser doppler measurement of inertial particle and bubble accelerations in turbulence”, EPL **81**, 34002 (2008).

[18] J. Rensen, S. Luther, and D. Lohse, “The effects of bubbles on developed turbulence”, J. Fluid Mech. **538**, 153–187 (2005).

[19] J. Martínez Mercado, D. Chehata Gómez, D. van Gils, C. Sun, and D. Lohse, "On bubble clustering and energy spectra in pseudo-turbulence", J. Fluid Mech. **650**, 287–306 (2010).

[20] K. Hoyer, M. Holzner, B. Lüthi, M. Guala, A. Liberzon, and W. Kinzelbach, "3D Scanning Particle Tracking velocimetry", Exp. in Fluids **39**, 923–934 (2005).

[21] B. Lüthi, A. Tsinober, and W. Kinzelbach, "Lagrangian measurement of vorticity dynamics in turbulent flow", J. Fluid Mech. **528**, 87–118 (2005).

[22] N. Ouellette, *Probing the statistical structure of turbulence with measurements of tracer particle tracks* (PhD thesis, Cornell University) (2006).

[23] E. Calzavarini, M. Kerscher, D. Lohse, and F. Toschi, "Dimensionality and morphology of particle and bubble clusters in turbulent flow", J. Fluid Mech. **607**, 13–24 (2008).

[24] S. Grossman and D. Lohse, "Intermittency exponents", Europhys. Lett. **21**, 201–206 (1993).

5

Three-dimensional Lagrangian Voronoï analysis for clustering of particles and bubbles in turbulence [*]

In the present chapter, three-dimensional Voronoï analysis is used to quantify the clustering of inertial particles in homogeneous isotropic turbulence using data from numerics and experiments. We study the clustering behavior at different density ratios and particle response times (i.e. Stokes numbers St). The probability density functions (PDFs) of the Voronoï cell volumes of light and heavy particles show a different behavior from that of randomly distributed particles —i.e. fluid tracers— implying that clustering is present. The standard deviation of the PDF normalized by that of randomly distributed particles is used to quantify the clustering. Light particles show maximum clustering for St around $1-2$*. The results are consistent with previous investigations employing other approaches to quantify the clustering. We also present the joint PDFs of enstrophy and Voronoï volumes and their Lagrangian autocorrelations. The small Voronoï volumes of light particles correspond to regions of higher enstrophy than those of heavy particles, indicating that light particles cluster in higher vorticity regions. The Lagrangian temporal autocorrelation function of Voronoï volumes shows that the clustering of light particles lasts much longer than that of heavy or neutrally buoyant particles. Due to inertial effects, the Lagrangian*

---

[*] Submitted to J. Fluid Mech. as: Y. Tagawa, J. Martínez Mercado, V.N. Prakash, C. Sun, and D. Lohse. Three-dimensional Lagrangian Voronoï analysis for clustering of particles and bubbles in turbulence, 2011.

autocorrelation time-scale of clustered light particles is even longer than that of the flow structures themselves.

5.1 Introduction

The distribution of particles transported by turbulent flows is a current research topic with implications in diverse fields, such as cloud formation [1], plankton dynamics [2], and pollution dispersion [3]. In most of the cases, the particles have a finite size and a different density than the carrier fluid, i.e. they have inertia. These inertial particles cannot totally follow the fluid motion and distribute inhomogeneously within the turbulent flow, leading to clustering or preferential concentration [4]. The two relevant dimensionless parameters describing the dispersed inertial particles in the fluid are the density ratio $\beta = 3\rho_f/(\rho_f + 2\rho_p)$, where ρ_f and ρ_p are the densities of the carrier fluid and particle respectively, and Stokes number, St= τ_p/τ_η, where $\tau_p = a^2/3\beta\nu$ is the particle relaxation time, τ_η is the typical timescale of the flow, which for a turbulent flow is the Kolmogorov's time scale, a is the particle radius and ν is the kinematic viscosity of the fluid.

In recent years, both numerical and experimental studies have quantified the clustering of particles by employing different approaches like statistical analysis of single-point measurements [5], box-counting method [6, 7], pair correlation functions [8, 9], Kaplan-Yorke dimension [10, 11], Minkowski functionals [11] and segregation indicators [12]. It is not possible to obtain global information on bubble clustering from a single-point analysis [5]. Methods like the box-counting and pair correlation functions, although useful, require the selection of an arbitrary length scale that affects the quantification of the clustering. The Kaplan-Yorke dimension, based on the calculation of the Lyapunov exponents, quantifies the contraction of a dynamical system by considering the separation rates of particle trajectories. Nevertheless, it does not provide global morphological information. Minkowski functionals, originally used to provide complete morphological information of the large-scale distribution of galaxies [13], have been applied to study the clustering of particles in turbulent flows [11]. Calzavarini *et al.* [11] found that light particles cluster in filamentary structures, whereas heavy particles have a wall-like topology around interconnected tunnels, and obviously no clustering was observed for neutrally buoyant tracers. In the above numerical simulations and experiments, the strongest clustering was found for particles with St$\approx$O(1). The problem with Minkowski-type analysis is that it is numerically expensive, and it does not provide information on the Lagrangian evolution of the clusters.

An alternative mathematical tool that can be used to study clustering is the Voronoï tesellation, which has been used in astronomy as a tool to characterize clustering of galaxies [14]. Recently, Monchaux *et al.* [15] applied a Voronoï analysis to quantify the clustering of heavy particles in grid-generated turbulence. This Voronoï approach does not require the selection of an arbitrary length scale for a fixed particle number. Monchaux *et al.* [15] obtained two-dimensional particle positions by imaging a turbulent flow in a wind tunnel seeded with droplets. The Voronoï cells are defined based on the positions of the particles within the measurement domain. One can quantify the clustering by calculating the probability density function (PDF) of the normalized areas of the Voronoï cells. The PDF will have a different shape for inertial particles when compared to the corresponding PDF of randomly distributed particles. The main difference is observed at the small and large values of normalized areas, where the PDF of heavy particles has a higher probability than for randomly distributed particles. There is a central region where there is no significant difference between the PDFs of heavy particles and randomly distributed ones. The values of normalized areas at which the PDF deviates from the randomly distributed particles can be used as thresholds to classify Voronoï cells that belong either to clusters or voids. Monchaux *et al.* [15] reported a maximum preferential concentration for St around unity, in agreement with other methods that have been used to study clustering.

The objective of the present work is to extend the work in [15] to: (i) three-dimensions and (ii) a much larger range of density ratios (including light, heavy, and neutrally buoyant particles) and Stokes numbers, i.e. we quantify particle clustering by applying three-dimensional Voronoï analysis both for numerical and experimental data sets of particles and bubbles. Moreover, we (iii) correlate the clustering behavior of different particles with local turbulent flow quantities and (iv) study for the first time the Lagrangian temporal evolution of the clusters.

5.2 Experimental and numerical datasets and Voronoï analysis

5.2.1 Datasets

The numerical scheme for a dilute suspension (neglecting particle collisions) of point particles in homogeneous and isotropic turbulence is described as follows [11, 16]:

$$\frac{dv}{dt} = \beta \frac{D}{Dt} u(x(t),t) - \frac{1}{\tau_p}(v - u(x(t),t)) \tag{5.1}$$

where $v = dx/dt$ is the particle velocity and $u(x(t),t)$ the velocity field. The dimensionless numbers used to model the particle motion are the density difference between the particle and the fluid β and the Stokes number St. The values of β = 0, 1 and 3 correspond to very heavy particles, neutrally buoyant tracers, and bubbles in water, respectively. When St = 0, the particles perfectly follow the fluid flow behaving as fluid tracers. We explore a parameter space of β = 0, 1, and 3 and St ranging from 0.1 to 4 consisting of 24 values at the Taylor-Reynolds number Re_λ = 75 and the spatial resolution of the simulation for $N = 128^3$ (from iCFDdatabase (http://cfd.cineca.it), [11]).

In our 3D particle tracking velocimetry (PTV) micro-bubble experiments, we use a 4-camera system to get micro-bubble positions in the active-grid-generated turbulence in the Twente Water Tunnel (TWT) (for details, see chapters 2 and 4). For the experimental data, the corresponding values are β = 3 and St = 0.04, the mean number of particles is 1.3×10^3.

5.2.2 Voronoï analysis

The Voronoï diagram is a spatial tesselation where each Voronoï cell is defined at the particle location based on the distance to the neighboring particles [17]. Every point in a Voronoï cell is closest to the particle position compared to the neighboring particles, the exceptions are the vertices, borderlines and facets (see figure 5.1). Therefore, in regions where particles cluster, the volume of the Voronoï cells is smaller compared to that of the cells in neighboring regions. Hence, the volume of the Voronoï cells is inversely proportional to the local particle concentration. The PDF of the Voronoï volumes normalized by the mean volume for randomly distributed particles can be well described by a Γ-distribution [18] (see figure 5.2). In the three-dimensional case, the Γ distribution has the following prefactor and exponent:

$$f(x) = \frac{3125}{24} x^4 \exp(-5x). \tag{5.2}$$

Here x is the Voronoï volume normalized by the mean volume. Particles which are not randomly distributed will have a PDF that deviates from this Γ-distribution, indicating preferential concentration. The Voronoï cells of particles located near the edges of the domain are ill-defined, i.e. they either do not close or close at infinity. These cells at the border of the domain are not considered for the analysis.

5.3 Results

First, we present results on the effect of the density ratio β on the clustering, followed by the effect of the Stokes number. Then, we show how the volume of Voronoï cells and enstrophy are related. Finally, we present results on the Lagrangian autocorrelations of Voronoï volumes and enstrophy.

5.3.1 Density effect

Here we study the clustering behavior for different β at a fixed St. Figure 5.2 shows the PDFs of the normalized Voronoï volumes for heavy, neutrally buoyant, and light

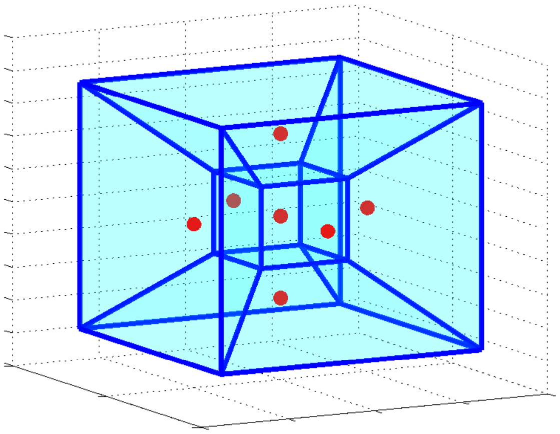

Figure 5.1: An example of a 3D Voronoï tesselation. The dots represent the particle position and lines represent the borders of the Voronoï cells.

particles at St = 0.6. The PDF of neutrally buoyant particles follows the Γ-distribution eq. (5.2) quite well, reflecting that neutrally buoyant particles do not have any preferential concentration. In contrast, the PDFs of light and heavy particles clearly show a different behavior compared to the randomly distributed particles. We observe that the probability of finding either small or large Voronoï volumes is higher for both light and heavy particles. The two regions of small and large volumes can be used to identify clusters and voids. The strongest clustering is observed for light particles, as the probability of finding small Voronoï volumes is the highest. Owing to the density difference, light particles accumulate in vortex filaments due to centrifugal forces [19, 20], while heavy particles concentrate in regions of intense strain [10]. Here, although the heavy particles show clustering, it is less compared to light particles. These results are consistent with the Minkowski analysis in [11].

5.3.2 Stokes number effect

In this section, we study the effect of St on the clustering behavior for each type of particle. Figure 5.3a and figure 5.3b show PDFs of heavy (β=0) and light (β=3) particles for different St, respectively. In both figures, it is seen that there is a non-monotonic dependence of St on the clustering. At increasing St, the probability of finding clusters and voids also increases up to a value of St=2, where it reaches a maximum and then starts to decrease. On the one hand, when St is nearly zero,

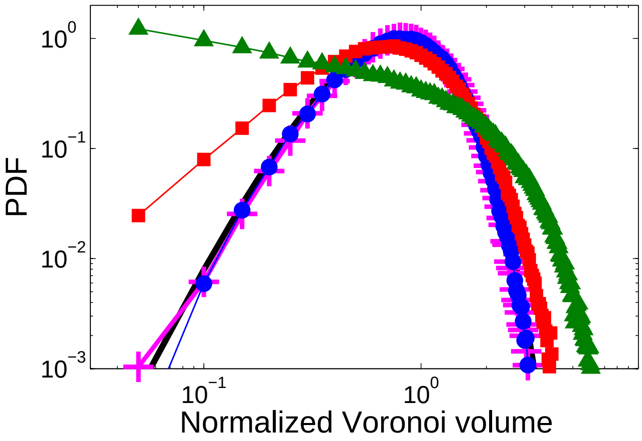

Figure 5.2: The normalized Voronoï volume PDFs for heavy (■), neutrally buoyant(●), and light particles (▲) at St = 0.6 from DNS. The thick line shows the Γ-distribution eq. (5.2) for randomly distributed particles [18], the PDF of the tracers agrees well with the randomly distributed particles (+). Heavy particles show more clustering and light particles show the maximum clustering.

particles follow the small-scale turbulent fluctuations which are homogeneous and isotropic and therefore, clustering is less. On the other hand, at St=4 the particle response time is too large to follow the small-scale turbulent fluctuations resulting in a ballistic behavior. Hence, the optimal St for clustering is in the range St $\approx$ 1-2.

We first discuss light particles in more detail. We note that the experimental result for micro-bubbles with St = 0.04 agrees reasonably well with the trend of the numerical data for light particles, though the PDF seems to be slightly broader. In any case, for these small Stokes numbers, the PDF of the Voronoï volumes is still qualitatively similar to that of tracers. The PDF is different for light particles with higher Stokes numbers. For St in the range of 0.6 to 4, the highest probability occurs at the smallest volume and decreases monotonically with increasing volume. Bubbles in this range of St tend to get trapped in vortex filaments, leaving void regions. Thus, most of the bubbles are concentrated in small regions and there are few bubbles outside these small regions.

However, this monotonic decrease in probability is not observed for heavy particles (see figure 5.3a). The reason is that heavy particles are expelled from the vortex filaments and accumulate in the regions of high strain. As described in [11], the heavy particles accumulate in a wall-like topology with interconnected tunnels. These tunnels fill the regions in-between the smaller vortex filaments and thus occupy larger

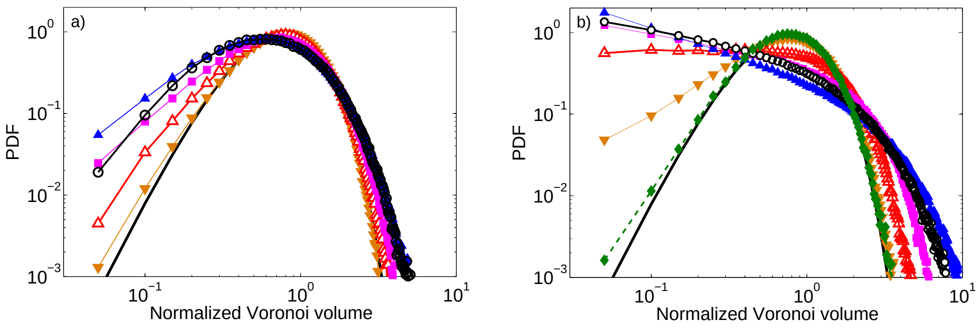

Figure 5.3: The normalized Voronoï volume PDFs for different St ranging from 0.1 to 4 in the numerics for (a) heavy particles β=0, (b) light particles β=3. St = 0.1(▼), 0.3 (△), 0.6 (■), 2 (▲), and 4 (○). The clustering increases till St = 2 and then decreases slightly at St = 4. The optimal St for clustering is St $\approx 1-2$. The diamonds (♦) correspond to the experimental result with St = 0.04.

regions in the flow. This leads to a more even distribution of heavy particles.

The PDFs of the Voronoï volumes provide a quantitative picture of the clustering. In order to quantify the clustering using a single number, we use the standard deviation σ of the normalized Voronoï volume distributions. In figure 5.4, we plot σ normalized by the standard deviation of the Voronoï volumes for randomly distributed particles σ_Γ. The magnitude of the indicator σ/σ_Γ clearly distinguishes the behavior of light, neutrally buoyant, and heavy particles. A higher value of the indicator reflects stronger clustering. For neutrally buoyant particles there is no observed clustering, hence the indicator value is constant at 1. Heavy particles show clustering and the indicator value saturates at St $\approx$ 1-2. The curve corresponding to light particles show the strongest clustering, with a peak at St $\approx$ 1.5. The clustering range has a consistent trend with that of the Kaplan-Yorke dimension [11]. We also added the data point for the standard deviation of the experimental Voronoï volume PDF, which, as already stated above, is broader than those from the numerical simulations of light point particles. At this point we cannot judge whether this is due to the limitations of point-particle simulations or whether the deviation is due to experimental uncertainties. More experimental data at larger Stokes numbers, i.e., larger bubbles or light particles, must be taken to come to a final conclusion on this issue.

5.3.3 Relation between the volume of the Voronoï cell and enstrophy

We relate the Voronoï volumes for the three different type of particles with turbulent flow quantities. A natural property for this comparison would be the enstrophy $\Omega =$

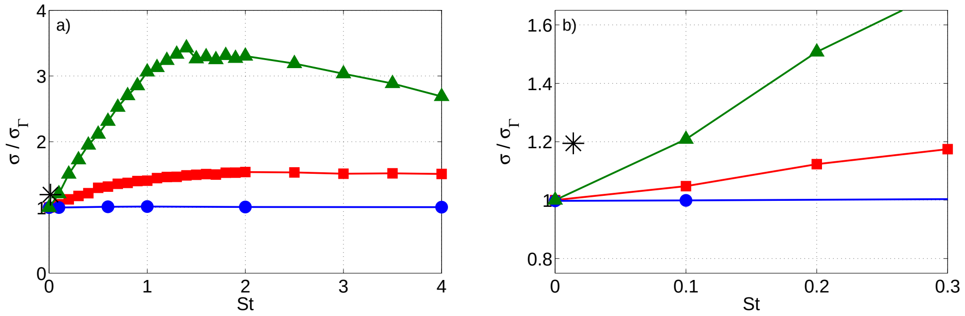

Figure 5.4: Normalized standard deviation (indicator) of the Voronoï volume distributions. The symbols correspond to heavy (■), neutrally buoyant (●), and light particles (▲). The value of the indicator for neutrally buoyant particles remains constant at 1, i.e. clustering is not observed, whereas heavy particles and light particles show more clustering with a peak at St $\approx$ 1.5. The experimental result of microbubbles ($*$) is larger than what is obtained from the numerical simulations of light point-particles with the same Stokes number.

$\omega^2/2$ (where ω is vorticity). Benzi *et al.* [21] have shown that different types of particles react sensitively to the local enstrophy, reflecting their tendency to stay in regions with different vorticity contents. They also find the local energy dissipation rate is too insensitive to show this different behavior. We thus calculate the joint PDF of Voronoï volumes and enstrophy at a fixed St = 0.6. Figure 5.5 shows the joint PDF of normalized Voronoï volumes with the enstrophy $\omega^2/2$, which is normalized by the mean value of the enstrophy of fluid tracers (St = 0, $\beta = 1$) $< \omega_{tr}^2/2 >$, for the three types of particles. We observe a clear difference in the behavior of heavy and light particles. Firstly, the peak of the PDFs shifts to higher enstrophy values as β increases. Secondly, for light particles the small Voronoï volumes are typically found at high values of enstrophy, whereas small Voronoï volumes of heavy particles are typically found at low enstrophy regions. To investigate these differences further, we analyze the relative PDFs of enstrophy. Figure 5.5(d) shows the relative PDF of enstrophy for heavy, neutrally buoyant, and light particles. As we focus on clustering, in the calculation of the PDFs we consider only particles with Voronoï cells 1/2 times smaller than the mean Voronoï volume. The PDFs are normalized with the enstrophy PDF obtained by considering all particles of that type. For neutrally buoyant particles, the relative PDFs have a nearly constant value of 1. For the case of bubbles, the PDFs show that small Voronoï cells have large values of enstrophy. In contrast, the relative PDF of heavy particles shows an opposite behavior to that of light particles. This reflects the clustering of light particles in flow regions with high enstrophy, whereas heavy particles cluster in low enstrophy regions.

5.3.4 Voronoï Lagrangian autocorrelation

Finally, we conduct a Lagrangian analysis on the Voronoï volumes. For each particle we calculate the Lagrangian autocorrelation of its associated Voronoï volume. Figure 5.6a shows a typical temporal evolution of Voronoï volumes for the three types of particles. To compare the behavior of the three different particles, we choose particles with similar Voronoï volume at the starting time and trace their time evolution. While Voronoï volumes of heavy and neutrally buoyant particles change frequently in time, it is clearly seen that light particles tend to have small values for longer times. This suggests that light particles are trapped in vortex filaments for a long time and are suddenly ejected, as seen in figure 5.6a around $\tau/\tau_\eta \approx 95$.

Figure 5.6b shows the autocorrelation function $C_V(\tau)$ for heavy, neutrally buoyant, and light particles at a fixed St = 0.6. We define the decorrelation time τ_V as the time when the autocorrelation function has decreased to 1/2, i.e., $C_V(\tau_V) = 1/2$. As shown in figure 5.6b, the decorrelation time for light particles is around $\tau_V \sim 7-8\tau_\eta$, whereas for heavy and neutrally buoyant particles decorrelation already occurs around $4-5\tau_\eta$. Thus the clustering of light particles lasts for a longer time as compared to heavy and neutrally buoyant particles.

We also compare the autocorrelation time scale of the Voronoï volumes to that of the enstrophy [21]. First, as expected, for neutrally buoyant particles, the Lagrangian decorrelation time for the Voronoï volumes is comparable to that of the enstrophy (τ_Ω), i.e. $\tau_\Omega \sim \tau_V \sim 4-5\tau_\eta$, reflecting that the clustering of neutrally buoyant particles has an instantaneous response to the changing turbulent structures. Also for heavy particles, the Lagrangian decorrelation time of the Voronoï volumes is around that value. However, remarkably, for light particles the decorrelation time of the Voronoï volumes is much larger, $\tau_V \sim 7-8\tau_\eta$, i.e., about nearly twice as large as the autocorrelation time scale $\tau_\Omega \sim 4\tau_\eta$ of the enstrophy itself. So though regions of high enstrophy trap bubbles, which leads to bubble clusters, the life-time of these bubble clusters is nearly twice as long as the life-time of the bubble-trapping flow structures itself. We interpret this finding as an inertial effect.

5.4 Conclusion

We use three-dimensional Voronoï analysis to study particle clustering in homogenous isotropic turbulence in both numerics and experiments. The analysis is applied to inertial particles (light, neutrally buoyant, and heavy) of different density ratios β and St ranging from 0 to 4. In the entire range of parameters covered, the Voronoï volume PDFs of neutrally buoyant particles agree well with the Γ-distribution for

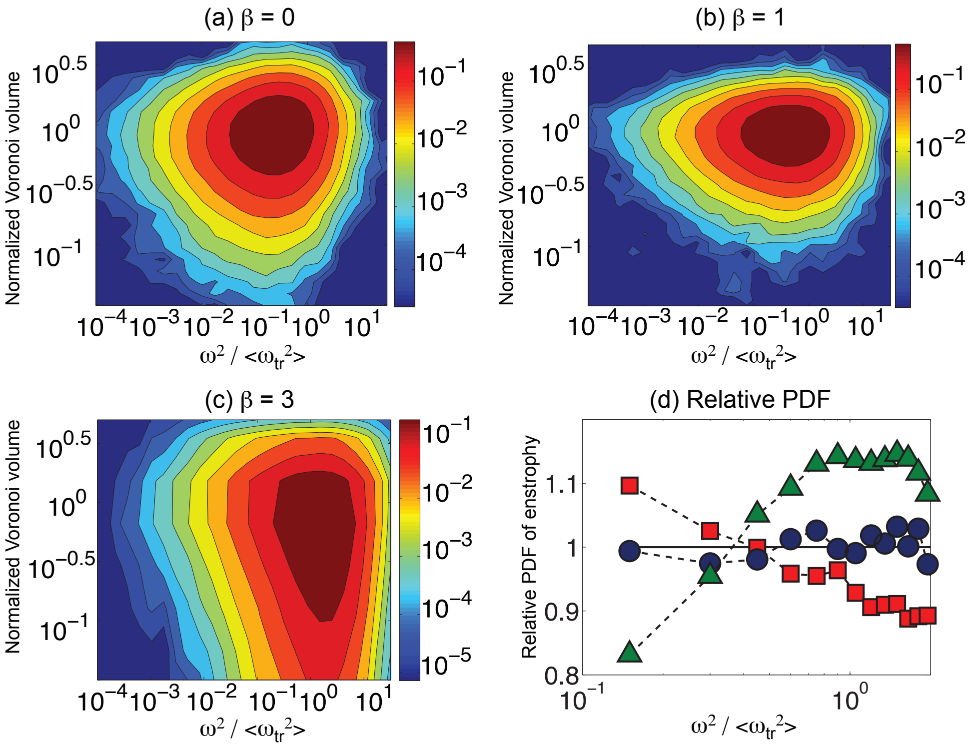

Figure 5.5: Joint PDFs of normalized Voronoï volumes and enstrophy at St = 0.6 . (a) heavy particles, (b) neutrally buoyant particles, and (c) light particles. (d) The relative Probability Density Function of the enstrophy of Voronoï cells 0.5 times smaller than the mean Voronoï volume for heavy (■), neutrally buoyant (●), and light particles (▲) at St = 0.6. The PDF of enstrophy is divided by the PDF considering all Voronoï volumes of a specific particle.

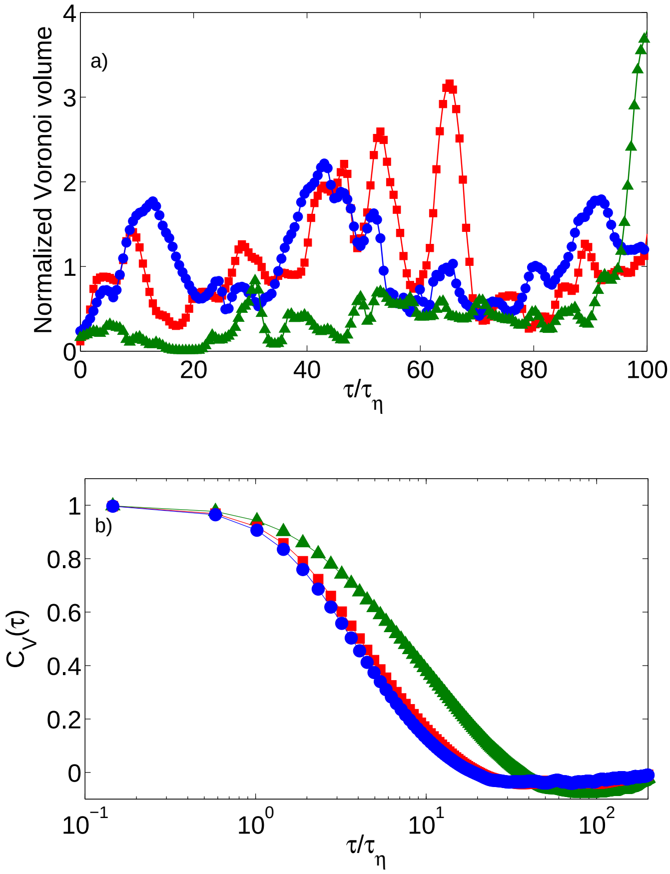

Figure 5.6: Lagrangian Voronoï analysis for heavy (■), neutrally buoyant (●), and light particles (▲) at St = 0.6. (a) Temporal evolution of Voronoï volumes. (b) Temporal autocorrelation functions of Voronoï volumes.

randomly distributed particles. At a fixed value of St, the PDFs of Voronoï volumes of light and heavy particles show higher probability to have small and large Voronoï volumes than randomly distributed particles, reflecting the clustering behavior. For light and heavy particles, the clustering behavior is non-monotonic with increasing St and shows a maximum around unity. In the range $0.6 \leq \mathrm{St} \leq 4$, the light particles show a pronounced monotonic decrease of probability with increasing Voronoï volumes. This indicates that light particles have more tendency to get trapped in vortex filaments, thus leaving void regions in space. The standard deviation of normalized Voronoï volumes σ is used to quantify the clustering. Heavy particles show some clustering, the indicator (σ/σ_Γ) saturates at St $\approx$ 1-2. Light particles show the strongest clustering, peaking around St $\approx$ 1-2. The maximum clustering range has a consistent trend with that of the Kaplan-Yorke dimension.

For one (small) Stokes number St=0.04 we have also extracted the 3D Voronoï volume PDF from experimental data. Though the PDF fits into the general trend – at these small Stokes numbers the PDF nearly follows a Γ-distribution – a quantitative analysis shows that the experimental PDF of 3D Voronoï volumes is slight broader than what is obtained from point-particle simulations. More experiments with larger Stokes numbers will have to be done to judge whether this is a limitation of the point-particle approach, a consequence of the neglectance of two-way and four-way coupling in the numerics, or whether the experimental data are not precise enough. From our point of view, the Voronoï analysis is an excellent means to quantitatively compare clustering effects of particles in experimental and numerical data sets, and should be used for the validation of numerical schemes of turbulent dispersed multiphase flow.

Finally, we show that the Voronoï analysis can be connected to local flow properties like enstrophy. By comparing the joint PDFs of enstrophy and Voronoï volumes and their Lagrangian autocorrelation, the clustering behavior of heavy, neutrally buoyant, and light particles can further be distinguished. From the Lagrangian autocorrelation of Voronoï volumes we conclude that due to inertial effects light particles remain clustered for nearly twice as long as heavy or neutrally buoyant particles or the bubble-trapping flow structures itself.

References

[1] E. Bodenschatz, S. P. Malinowski, R. A. Shaw, and F. Stratmann, “Can we understand clouds without turbulence?”, Science **327**, 970–971 (2010).

[2] F. Schmitt and L. Seuront, “Intermittent turbulence and copepod dynamics: increase in encounter rates through preferential concentration”, J. Mar. Syst. **70**, 263–272 (2008).

[3] J. Weil, R. Sykes, and A. Venkratam, “Evaluating air-quality models: review and outlook”, J. Appl. Meteorol. **31**, 1121–1145 (1992).

[4] F. Toschi and E. Bodenschatz, “Lagrangian properties of particles in turbulence”, Annu. Rev. Fluid Mech. **41**, 375–404 (2009).

[5] E. Calzavarini, T. van der Berg, F. Toschi, and D. Lohse, “Quantifying microbubble clustering in turbulent flow from single-point measurements”, Phys. Fluids **20**, 040702 (2008).

[6] J. Fessler, J. Kulick, and J. Eaton, “Preferential concentration of heavy particles in a turbulent channel flow”, Phys. Fluids **6**, 3742–3749 (1994).

[7] A. Aliseda, A. Cartellier, F. Hainaus, and J. Lasheras, “Effect of preferential concentration on the settling velocity of heavy particles in homogeneous isotropic turbulence”, J. Fluid Mech. **468**, 77–105 (2002).

[8] L. Chen, S. Goto, and J. Vassilicos, “Turbulent clustering of stagnation points and inertial particles”, J. Fluid Mech. **553**, 143–154 (2006).

[9] E. Saw, R. Shaw, S. Ayyalasomayajula, P. Chuang, and A. Gylfason, “Inertial clustering of particles in high-Reynolds-number turbulence”, Phys. Rev. Lett. **100**, 214501 (2008).

[10] J. Bec, L. Biferale, G. Boffetta, A. Celani, M. Cencini, A. Lanotte, S. Musacchio, and F. Toschi, “Acceleration statistics of heavy particles in turbulence”, J. Fluid Mech. **550**, 349–358 (2006).

[11] E. Calzavarini, M. Kerscher, D. Lohse, and F. Toschi, “Dimensionality and morphology of particle and bubble clusters in turbulent flow”, J. Fluid Mech. **607**, 13–24 (2008).

[12] E. Calzavarini, M. Cencini, D. Lohse, and F. Toschi, “Quantifying turbulence-induced segregation of inertial particles”, Phys. Rev. Lett. **101**, 084504 (2008).

[13] M. Kerscher, K. Mecke, J. Schmalzing, C. Beisbart, T. Buchert, and H. Wagner, “Morphological fluctuations of large-scale structure: the PSCz survey”, Astron. Astrophys. **373**, 1–11 (2001).

[14] R. van de Weygaert and V. Icke, “Fragmenting the universe. ii. voronoi vertices as abell clusters”, Astron. Astrophys. **213**, 1–9 (1989).

[15] R. Monchaux, M. Bourgoin, and A. Cartellier, “Preferential concentration of heavy particles: A voronoi analysis”, Phys. Fluids **22**, 103304 (2010).

[16] M. Maxey and J. Riley, “Equation of motion for a small rigid sphere in a nonuniform flow”, Phys. Fluids **26**, 883–889 (1983).

[17] A. Okabe, B. Boots, K. Sugihara, and S. Chiu, *Spatial tesselations*, first edition (John Wiley & Sons) (2000).

[18] J. Ferenc and Z. Néda, “On the size distribution of poisson voronoi cells”, Physica. A **385**, 518–526 (2007).

[19] I. Mazzitelli, D. Lohse, and F. Toschi, “On the relevance of the lift force in bubbly turbulence”, J. Fluid Mech. **488**, 283–313 (2003).

[20] I. Mazzitelli and D. Lohse, “Lagrangian statistics for fluid particles and bubbles in turbulence”, N. J. of Phys. **6**, 203 (2004).

[21] R. Benzi, L. Biferale, E. Calzavarini, D. Lohse, and F. Toschi, “Velocity-gradient statistics along particle trajectories in turbulent flows: The refined similarity hypothesis in the lagrangian frame”, Phys. Rev. E **80**, 066318 (2009).

6

Conclusions and Outlook

In this work we have studied bubbly flows in two different conditions. In the first one, bubbles with typical diameter d_b =4—5 mm rise in still liquid inducing liquid fluctuations that are referred as to pseudo-turbulence. In the second one, micro-bubbles are dispersed in homogeneous isotropic turbulence, and interact with the flow structures.

For the investigation of these bubbly flows, we implemented two novel experimental techniques. On the one hand, we have used phase-sensitive constant temperature anemometry (CTA) to measure the liquid fluctuations in pseudo-turbulence. This technique allows for a direct measurement and removal of bubble collisions with the hot-film probe. In this manner, only liquid information is considered, and a proper scaling of the energy spectrum of liquid fluctuations can be obtained.

On the other hand, we have used three-dimensional particle tracking velocimetry (PTV) to obtain the bubbles positions. Using a tracking algorithm, the bubble trajectories are determined, and by differentiating them, velocity and acceleration are readily available allowing thus the study of the Lagrangian statistics and clustering phenomena in three dimensions.

In chapter 2, we studied the velocity PDFs, clustering and energy spectra of the liquid fluctuations in pseudo-turbulence in very dilute bubbly flows. Due to the non-intrusiveness of PTV, we obtained well-converged PDFs of bubble velocity, and showed that they are non-Gaussian. The vertical component of the velocity is the more intermittent one. The clustering of the bubbles in pseudo-turbulence was investigated by employing the pair correlation function. Pairs of bubbles cluster radially within a distance of around 1 bubble diameter. The preferential alignment is vertical for large and small scales. However, at small scales, the horizontal clustering is also enhanced and comparable to the vertical one. We also calculated the energy spectra of liquid fluctuations in pseudo-turbulence and found that there was not a classical turbulent $-5/3$ scaling but a scaling close to -3. Suggesting the idea that bubble wake phenomena is related to this power law behavior.

Chapter 3 is aimed at comparing results of front-tracking DNS with experiments. Our motivation was to confirm that bubble wake phenomena causes the -3 scaling of the energy spectrum of the liquid fluctuations as front-tracking simulations are able to resolve the bubble's interface with the liquid contrarily to point-particle simulations. We found that indeed the scaling obtained with numerics matches the experimental finding. Due to the short simulation times, the -3 scaling holds in a narrower frequency region though. We also corroborate numerically that the velocity PDFs of bubbles have a non-Gaussian distribution, and that the vertical component present the largest deviation from a Gaussian distribution. The intermittency of the PDFs is less as in the experimental case, as a result of the periodic boundary conditions and small domain size.

The Lagrangian statistics of micro-bubble velocity and acceleration in homogenous isotropic turbulence are studied in chapter 4. Here, we carried out a comparison of the smoothing algorithms used commonly in the experimental research area of particles in turbulence. We showed that both a Gaussian smoothing and a polynomial fitting are able to reproduce the turbulent signature of the micro-bubbles in turbulence. Surprisingly to our knowledge, this is the first time that both methods are compared. Our findings corroborate the PDFs of micro-bubble velocity have a Gaussian distribution, whereas the PDFs of the micro-bubble acceleration are strong intermittent with a flatness value around 35. In the range of Re_λ covered, the shape and intermittency of the acceleration PDFs are independent of the turbulence intensity. The shape of these PDFs can be better fitted to a stretched exponential function rather than a log-normal distribution. When compared to point-particle DNS the intermittency of our PDFs is in between the values of numerical tracers and bubbles. This is a result of the Stokes number in our experiments which is one order of magnitude smaller. We also showed that our experimental results agree with other previous experimental studies. The decorrelation time of the micro-bubble acceleration increases linearly with Re_λ which is also in agreement with measurements in a turbulent von Kármán flow in [1, 2].

Finally, in chapter 5 we studied clustering of bubbles in turbulence using a Voronoï approach. We have extended the work of Monchaux *et al.* [3] to three-dimensions and to light and neutral particles for a range of Stokes numbers (i.e. different particle size). We analyzed data from point-particle DNS but also from experiments of micro-bubbles in the Twente Water Tunnel. We found that the PDFs of normalized Voronoï volumes of heavy and light particles are different than that of randomly distributed particles reflecting the clustering. Considering the density effect, bubbles cluster the most, whereas considering the size effects particles with St$\approx$1 cluster the most. To quantify this clustering, we propose the standard deviation of the PDFs of normalized volumes. Our result is consistent with previous results of the Kaplan-Yorke dimension [4]. The PDF of normalized Voronoï volumes of our experimental dataset agrees reasonably well with the numerical trend though it is a bit broader. Further, we showed that Voronoï analysis can be related to flow quantities like enstrophy. By looking at the joint PDF of Voronoï volumes and enstrophy we found that there is a clear difference in the behavior of heavy and light particles. The small Voronoï volumes of bubbles have a high enstrophy value, i.e. bubbles tend to accumulate in hight vorticity regions. A Lagrangian approach was also carried out, we showed that with the Lagrangian autocorrelation of Voronoï volumes for heavy, neutral and light particles the clustering behavior can be further distinguished. The decorrelation time of the Voronoï volumes of bubbles is much larger than that of neutral or heavy particles. The Lagrangian correlation of Voronoï volumes lasts surprisingly nearly twice as the life-time of the bubble-trapping structures (i.e. enstrophy). We interpret this result as an inertial effect.

In this last part of the thesis, we would like to comment on the future work and possible research directions. We presented in this current work the results of bubbles in two different regimes, one with “big” bubbles without turbulence and the other with micro-bubbles in turbulence. The natural direction to follow is to bridge the gap in bubble sizes and turbulent conditions.

In pseudo-turbulence there is still the question of how do the -3 scaling of the energy spectrum of the liquid fluctuations evolve as a function of the “bubblance” parameter b varying it from the typical turbulent case ($b = 1$) to the pseudo-turbulent case ($b = \infty$). The previous configuration of the Twente Water Tunnel was unstable when a mean flow larger than 0.25 ms^{-1} was set and bubbles were injected as the counterflow will not allow the bubbles to escape creating strong recirculation. Recently, a modification in the Water Tunnel was undertaken and the active grid was placed below the measurement section. With this change in the set up, bubbles can be injected from the capillary islands and the flow can be set upwards avoiding the recirculation patterns but also the risk of flooding. In such a way, b can be varied.

Furthermore, the bubble shape and deformability effect on the clustering can also be studied. By adding a small amount of surfactant, more spherical and rigid bubbles can be generated. It has been shown that even with small quantities of surfactant [5, 6], the bubble behavior changes drastically, from non-slip condition at the bubble interface to a rigid-like condition, accordingly the structure of the wake is also affected. It would be interesting to control these two parameters separately. For instance, the shape of the bubble can be changed using capillaries with different size, though the range of generated sizes is not very wide. Deformability can be modified by using surfactant, additionally the shape of the bubble will become more spherical and its size smaller. In the future experiments either varying these parameters independently or simultaneously are advisable.

Regarding the experimental part with bubbles in turbulent conditions, the main direction to follow is to study the size effect on the Lagrangian statistics and clustering. We have shown with the Voronoï analysis of the DNS data, that the clustering effect is stronger when St is close to unity. In the present case of micro-bubbles, the St was one order of magnitude smaller. An experimental proof of this finding is still necessary. Additionally, the Lagrangian statistics of micro-bubbles have an intermittency that is in between the intermittency of bubbles and tracers. By dispersing bubbles of size 1 mm or a bit smaller, we expect to confirm the numerical results. Also it is quite promising to investigate the Lagrangian statistics as a function of the normalized particle size D/τ_η. This kind of studies have never been done experimentally for the case of bubbles and will allow also a direct comparison with numerical simulations with corrections that account the size effects [7].

Apart to the size effect, a major achievement would also be to study the density effect. Experiments with neutral tracer and heavy particles will result in a complete study of particles in turbulence. Though, the implementation of such idea is not straightforward, and further modification of the Twente Water Tunnel is needed. Especially for the case of heavy particles as they must not flow through the pump to avoid damage.

References

[1] R. Volk, E. Calzavarini, G. Verhille, D. Lohse, N. Mordant, J.-F. Pinton, and F. Toschi, “Acceleration of heavy and light particles in turbulence: Comparison between experiments and direct numerical simulations”, Physica D **237**, 2084 – 2089 (2008).

[2] R. Volk, E. Calzavarini, E. Leveque, and J.-F. Pinton, “Dynamics of inertial particles in a turbulent von Kármán flow”, J. Fluid Mech. **668**, 223–235 (2011).

[3] R. Monchaux, M. Bourgoin, and A. Cartellier, “Preferential concentration of heavy particles: A voronoi analysis”, Phys. Fluids **22**, 103304 (2010).

[4] E. Calzavarini, M. Kerscher, D. Lohse, and F. Toschi, “Dimensionality and morphology of particle and bubble clusters in turbulent flow”, J. Fluid Mech. **607**, 13–24 (2008).

[5] S. Takagi, T. Ogasawara, and Y. Matsumoto, “The effects of surfactant on the multiscale structure of bubbly flows”, Phil. Trans. R. Soc. A **366**, 2117–2129 (2008).

[6] S. Takagi and Y. Matsumoto, “Surfactant effects on bubble motion and bubbly flows”, Annu. Rev. Fluid Mech. **43**, 615–636 (2011).

[7] E. Calzavarini, R. Volk, M. Bourgoin, E. Leveque, J.-F. Pinton, and F. Toschi, “Acceleration statistics of finite-sized particles in turbulent flow: the role of Faxèn forces”, J. Fluid Mech. **630**, 179–189 (2009).

Summary

Due to their relevance and occurrence in both natural phenomena and in industrial applications, the study and understanding of bubbly flows is currently an important topic for fluid dynamicists. Bubble columns are commonly used in bio- and petrochemical industries to enhance mixing, mass and heat transfer. In these systems, the bubbles are the only energy input as there is no flow a priori. Bubble columns are also referred to as pseudo-turbulence because the bubbles induce liquid fluctuations in the originally quiescent liquid. These disturbances are the result of the hydrodynamic interactions among the bubbles and their heterogenous distribution.

Turbulent flows transporting particles are ubiquitous in nature, being of such relevance in diverse fields ranging from atmospheric physics to oceanography. Usually the convected particles have a different density and size than the transporting fluid, turbulent bubbly flows are a particular case of them. In recent years, Lagrangian studies—i.e. studies following the particle motion—of particles in turbulence have gained considerable attention because this approach is closer to the inherent mixing and transport characteristic of turbulence. Yet there is still the challenge and interest to comprehend more the Lagrangian statistics of particles in turbulence.

This work studies bubbly flows in two different flow conditions. In the first part, we study the pseudo-turbulence induced by rising bubbles in quiescent liquid. In the second part, we study the Lagrangian statistics and clustering of micro-bubbles in homogeneous isotropic turbulence.

Part one presents experimental and numerical results on pseudo-turbulence. In chapter 2, experiments using three-dimensional particle tracking velocimetry (PTV) and phase-sensitive constant-temperature anemometry (CTA) are carried out to study bubble clustering, mean bubble velocity, bubble velocity probability density functions (PDFs) and liquid energy spectrum in pseudo-turbulence at very dilute gas concentrations ($\alpha < 2.2\%$). Bubbles with mean diameter of 4–5 mm are injected in still water. By employing three-dimensional PTV, the bubble position is determined and bubble clustering is studied. For this purpose, we use the pair correlation function $G(r, \theta)$. We find that bubbles cluster within few bubble radii as shown by the radial pair correlation $G(r)$. The angular pair correlation $G(\theta)$ reveals a robust vertical alignment at both small and large scales for all bubbles concentrations studied. However at small scales, horizontal alignment is also observed. The PDFs of bubble

velocity show that all components of bubble velocity behave differently from Gaussian. The implementation of PTV assures enough data points to obtain convergence in the PDFs. The non-Gaussianity can be a result of the cluster formation mechanism, where the rise velocity of single bubbles is affected by the faster collective motion of clusters. By employing phase-sensitive CTA , it is possible to measure the power spectrum in pseudo-turbulence. We find that the energy of the liquid fluctuations decays exponentially with a slope near -3 which is consistent with the theoretical scaling that Lance *et al.* derived. We also study pseudo-turbulence numerically, the results are presented in chapter 3, where we perform front-tracking direct numerical simulations (DNS). The numerical swarm of bubbles consist of monodisperse deformable 4 mm bubbles with a gas fraction of 5% and 15%. Within this chapter, our focus is to compare the liquid energy spectrum and bubble velocity PDFs with the experimental data. The numerical simulations confirm that the spectra of the velocity fluctuations driven by the rising bubbles follow a power law with slope close to -3. The computed PDFs of the bubble velocity show non-Gaussian features, as is also observed in the experiments. The agreement with experimental measurements is especially good in the peak region, whereas the tails of the experimental PDFs show more intermittency in comparison to the numerical results. We understand this disagreement as a the lack of large-scale flow structures in the simulations, mainly due to the imposed periodic boundary conditions and the domain size.

In the second part of this thesis, we study Lagrangian statistics and clustering of bubbles in homogeneous and isotropic turbulence. In chapter 4, the Lagrangian velocity and acceleration statistics of micro-bubbles (light particles) in turbulence are presented. For this purpose, micro-bubbles with diameter $d_b = 340\ \mu$m and Stokes number O(0.01) are dispersed in the Twente turbulent water tunnel. The micro-bubbles trajectories are obtained by employing PTV at different Re_λ. We compare thoroughly two smoothing methods— i.e. Gaussian kernel and polynomial fitting— and show that both give the intermittent characteristics along the micro-bubbles' trajectories. Our results show that the micro-bubbles' acceleration PDFs are highly intermittent with a flatness value of around 35. The experimental acceleration PDFs showed more intermittency than previous measurements of heavy particles, and are better fitted by a stretched exponential functional rather than a log-normal distribution. In addition, the acceleration autocorrelation function decorrelates much faster compared to experiments in different type of turbulent flows (e.g. von Kármán flow), and its decorrelation time increases with higher Re_λ. The velocity PDFs follow closely a Gaussian distribution with no dependence on Re_λ for all the three components with a flatness very close to 3.

The clustering of light, neutrally buoyant and heavy particles in homogenous isotropic turbulence is studied in chapter 5. Three-dimensional Voronoï analysis is used to quantify the clustering of inertial particles using data from numerics and experiments. We study the clustering behavior at different density ratios and particle response times (i.e. Stokes numbers St). Our findings show that the PDFs of the Voronoï cell volumes of light and heavy particles have a different behavior from that of randomly distributed particles —i.e. fluid tracers—implying that clustering is present. We use to quantify the clustering the standard deviation of the PDF normalized by that of randomly distributed particles. Light particles show maximum clustering for St around $1-2$. The results are consistent with previous investigations employing other approaches to quantify the clustering. We also present the joint PDFs of enstrophy and Voronoï volumes and their Lagrangian autocorrelations, and observe different cluster behavior between the three kind of particles . The small Voronoï volumes of light particles correspond to regions of higher enstrophy than those of heavy particles, indicating that light particles cluster in higher vorticity regions. The Lagrangian temporal autocorrelation function of Voronoï volumes shows that the clustering of light particles lasts much longer than that of heavy or neutrally buoyant particles. Due to inertial effects, the Lagrangian decorrelation time-scale of clustered light and heavy particles is longer than that of the flow structures themselves.

Samenvatting

Vanwege hun relevantie en voorkomen in zowel natuurlijke fenomenen als in industriële toepassingen is de studie en het begrip van stromingen met bellen momenteel een belangrijk onderwerp in de vloeistofdynamica. Bellen-kolommen worden vaak gebruikt in de bio- en petrochemische industrie om het mengen, en massa- en warmteoverdracht te verbeteren. In deze systemen zijn de bellen de enige energie-input, omdat er geen doorstroming a priori is, en ze worden ook wel aangeduid als pseudo-turbulentie omdat de bellen fluctuaties veroorzaken in de oorspronkelijk stilstaande vloeistof. Deze verstoringen zijn het gevolg van de hydrodynamische interacties tussen de bellen en hun heterogene distributie.

Turbulente stromingen waarin deeltjes worden vervoerd zijn alomtegenwoordig in de natuur, en zijn van groot belang in diverse gebieden variërend van atmosferische fysica tot oceanografie. Meestal hebben de vervoerde deeltjes een verschillende dichtheid en grootte dan de vloeistof, bellen in turbulente stromen zijn hier een voorbeeld van. In de afgelopen jaren hebben Lagrangiaanse studies—studies die de beweging van de deeltje volgen—in turbulentie veel aandacht gewonnen omdat deze aanpak is dichter ligt bij de inherente meng- en transportkenmerken van turbulentie. Maar er is nog steeds de uitdaging en interesse om meer te begrijpen van de Lagrangiaanse statistieken van deeltjes in turbulentie.

Dit werk bestudeert bellen in twee verschillende stromingscondities. In het eerste deel bestuderen wij de pseudo-turbulentie veroorzaakt door de stijgende luchtbellen in een stilstaande vloeistof. In het tweede deel bestuderen wij de Lagrangiaanse statistieken en het clusteren van micro-bellen in homogene isotrope turbulentie.

Deel één presenteert experimentele en numerieke resultaten op pseudo-turbulentie. In hoofdstuk 2 worden experimenten met behulp van driedimensionale particle tracking velocimetry (PTV) en phase-sensitive constant-temperature anemometry (CTA) uitgevoerd om het clusteren van bellen, de belsnelheid, de belsnelheids-kansdichtheidsfuncties (PDF) en vloeistof-energie-spectrum in pseudo-turbulentie op zeer lage gasconcentraties ($\alpha < 2,2\%$) te bestuderen. Bellen met een gemiddelde diameter van 4 - 5 mm worden geïnjecteerd in stilstaand water. Door het gebruik van driedimensionale PTV, is de belpositie bepaald en wordt het clusteren van bellen bestudeerd. Hiervoor maken wij gebruik van de paar-correlatiefunctie $G(r,\theta)$. Wij vinden dat bellen binnen enkele belstralen clusteren, zoals blijkt uit de radiale paar-correlatie

$G(r)$. De hoekafhankelijke paar-correlatie $G(\theta)$ vertoont een robuuste verticale uitlijning bij zowel kleine als grote schalen voor alle bestudeerde belconcentraties. Maar op kleine schaal, is horizontale uitlijning ook aanwezig. De belsnelheids-PDFs laten zien dat alle componenten van de belsnelheid zich anders gedragen dan Gaussiaanse. De implementatie van PTV zorgt voor voldoende datapunten, die convergentie in the PDFs verzekert. De niet-Gaussianiteit kan een gevolg zijn van het clustervormingsmechanisme, waar de stijg-snelheid van enkele bellen wordt beïnvloed door de snellere collectieve beweging van clusters. Door het gebruik van phase-sensitive CTA, is het mogelijk het energiespectrum in de pseudo-turbulentie te meten. Wij vinden dat de energie van de vloeistof-fluctuaties exponentieel vervalt met een helling dicht bij -3, die in overeenstemming is met de theoretische schaling dat Lance *et al.* heeft afgeleid.

Wij hebben ook pseudo-turbulentie met numerieke simulaties onderzocht. De resultaten worden in hoofdstuk 3 gepresenteerd, waar wij front-tracking directe numerieke simulaties (DNS) uitvoeren. De numerieke bellenzwerm bestaat uit monodisperse vervormbare 4 mm bellen met een gas-fractie van 5 % en 15 %. Binnen dit hoofdstuk is onze focus het energie-spectrum en de belsnelheids PDF te vergelijken met de experimentele data. De numerieke simulaties bevestigen dat de spectra van de snelheidsfluctuaties gedreven door de stijgende luchtbellen een machtswet volgt met een helling dicht bij -3. De berekende belsnelheids-PDFs vertoont niet-Gaussiaanse kenmerken, zoals ook waargenomen in de experimenten. De overeenkomst met experimentele metingen is vooral goed in de piek-regio, terwijl de staarten van de experimentele PDFs meer intermittentie vertonen in vergelijking met de numerieke resultaten. Wij begrijpen dit verschil, als een gebrek aan grootschalige stroom-structuren in de simulaties, voornamelijk als gevolg van de opgelegde periodieke randvoorwaarden en de domeingrootte.

In het tweede deel van dit proefschrift bestuderen wij Lagrangiaanse statistieken en het clusteren van bellen in homogene en isotrope turbulentie. In hoofdstuk 4 worden de Lagrangiaanse snelheid en versnellings-statistieken van micro-bellen (lichtdeeltjes) in turbulentie gepresenteerd. Voor dit doel zijn microbellen met een diameter van $d_b = 340$ μm en Stokes nummer O (0,01) verspreid in de Twente turbulente water tunnel. De trajecten van de microbellen worden verkregen door het gebruik van PTV bij verschillende Re_λ. Wij vergelijken grondig twee smoothing methoden —dat wil zeggen Gaussian kernel en polynomiale fitting— en laten zien dat beide de intermittente kenmerken langs de trajecten van de microbellen reproduceren. Onze resultaten tonen aan dat de versnellings-PDFs van de microbellen zeer intermittent zijn met een platheidswaarde van ongeveer 35. De experimentele versnellings-PDFs vertonen meer intermittentie dan vorige metingen van zware deeltjes, en worden beter gefit door een uitgestrekt exponentiële functie dan door een log-normale verdeling. Daarnaast decorreleert de versnellings-autocorrelatiefunctie veel sneller in vergelijking met experimenten in verschillende soorten van turbulente stromingen (bijv. von Kármán flow), en de decorrelatie-tijd neem toe met hogere Re_λ. De snelheids-PDFs liggen dichtbij een Gaussiaanse verdeling, zonder afhankelijkheid van Re_λ voor alle drie componenten met een platheid heel dicht bij 3.

Het clusteren van lichte, neutrale en zware deeltjes in homogene isotrope turbulentie wordt bestudeerd in hoofdstuk 5. Driedimensionale Voronoï-analyse wordt gebruikt om de clustering van inertiale deeltjes te kwantificeren. Wij gebruiken zowel numerieke als experimentele data en bestuderen het cluster-gedrag voor verschillende dichtheids-ratio's en deeltjes-responstijden (dat wil zeggen Stokes nummers St). Onze bevindingen tonen aan dat de PDFs van de Voronoï-cel-volumes van lichte en zware deeltjes een ander gedrag dan dat van willekeurig verspreide deeltjes hebben — vloeistof tracers — dus clustering aanwezig is. Om de clustering te kwantificeren gebruiken wij de standaardafwijking van de PDF genormaliseerd door die van willekeurig verspreide deeltjes. Lichte deeltjes laten maximale clustering zien voor St ongeveer $1-2$. De resultaten komen goed overeen met eerdere onderzoeken, die andere analyze-methoden voor de clustering hebben gebruikt. Wij presenteren ook de gezamenlijke PDFs van enstrophy en Voronoï volumes en hun Lagrangiaanse autocorrelations, en observeren verschillend clustergedrag tussen de drie soorten deeltjes. De kleine Voronoï volumes van lichte deeltjes komen overeen met de gebieden van hogere enstrophy dan die van zware deeltjes, wat aangeeft dat lichte deeltjes in het hoger vorticiteitsgebied clusteren. De Lagrangiaanse temporele autocorrelatiefunctie van Voronoï-volumes laat zien dat de clustering van lichte deeltjes veel langer duurt dan die van zware of neutraal drijvende deeltjes. Vanwege de inertie is de Lagrangiaanse autocorrelatie-tijdschaal van geclusterde lichte deeltjes zelfs nog langer dan die van de stroomstructuren zelf.

Acknowledgements

In this section, the author shows that the results presented above are the natural consequence of a collective effort. The crystallization process of such a thesis is enhanced when energy inputs at various different scales and of different natures interact closely with the system. The author starts the chapter acknowledging people and summarizes it exactly the same way.

The bubbles in the Meander

The turbulent particles

First of all, I want to thank deeply my promotor Prof. Detlef Lohse. To you all my recognition for the tremendous work you do supervising several PhD projects among many other activities. Your scientific curiosity has always been inspiring and encouraging. I have learned so many things from all our discussions and meetings, which most of the times inevitably started late due to your incredible busy agenda. Without surprise they also finish late because all of us were philosophizing with plots and symbols. It has been a great pleasure to work in your research team, giving me the opportunity to develop myself within a competitive but overall friendly group.

A very special thank goes to my daily supervisor Dr. Chao Sun. Without your guidance the path leading to the goal would have been a bit more sinuous. I remember when you first arrived to the group in September 2007. That day you entered the lab, extended your arm for handshaking and said: *Hello, my name is Sun, Chao Sun*. It was clear that you were a funny, energetic and nice guy. Later on, you took over naturally the daily guidance of the turbulent investigations in our group. Your experimental and turbulence expertise was always very helpful for us in the Water Tunnel lab. Thank you for being available at any time to discuss results or to comment merely on life. Especially, I enjoyed the way you call for informal but quite beneficial meetings. You entered the lab saying: *Hey guys, Julián, Vivek, Yoshi come here, let's discuss!*, regardless of what we were doing or being busy with.

To Yoshi and Vivek, my actual officemates and close collaborators. Yoshi, thanks also for co-supervising me as well. Guys, your advises, suggestions and critics to the work were always helpful and improved it further. Thank you for all the fun we have had working together in this project. I really appreciate the team work with you, discussing ideas, sorting out practical problems in our research or simply the many times we had lunch inside the lab because a meeting or deadline was approaching for which we were not completely done.

Chao, Yoshi, Vivek, thank you also for your friendship. Guys, I will always be grateful with your and Detlef's support when I lost the data. Fortunately and thanks to all of you, things worked out smoothly!

To Daniel Chehata with whom I worked for two years in the early period of setting up the PTV system. Thank you for your practical help, ideas and suggestions to get the PTV to work, it was crucial. It was fun to listen to *Los Tigres del Norte* while working in the lab. Gracias por tu amistad y por compartir tu filosfía itinerante de pata de perro.

To Dennis van Gils for helping me in the very beginning of my project. Toen de groep verplaatste, was jou werk echt belangrik om de Water kanaal Lab klaar te krijgen. In het begin was ik liever jou helper en tegelijk heb ik de systemen geleerd.

To the rest of the turbulent particles: Sander, Daniela and Richard. Sander thanks for helping me out with my Mathematica ignorance. For all the exchange of ideas and tips when it came to common equipment and for the free-trade agreement we have for borrowing tools/equipment between the two labs.

The IPP-FOM

I would like to thank FOM and the industrial partners (Shell, AkzoNobel, Tata Steel, DSM) for funding my project within the frame of the Industrial Partnership Programme: *Fundamentals of heterogenous bubbly flows*. Thanks to Pieter de Witte, Prof. Kuipers, Prof. Martin van Sint Annaland, Niels Deen, and the people in the industry. Special thanks to Ivo, Yuk Man and Raja whose projects were also part of this big research programme. In the beginning of the programme we had a bit stress with the first progress meetings, but later on, we enjoyed them and getting to know each other's project helped to interact more closely. To Ivo Roghair for the fruitful collaboration we had and which resulted in a joint paper between our groups. Het was leuk samen de belletjes van beide kanten (numeriek en experimenteel) te onderzoeken.

The fluid particles

Experimental works involve most of the time contribution from many people. Big experimental facilities like the Twente Water Tunnel are by no means the exception. I am totally indebted with our unique technicians: Gert-Wim and Martin. Thanks a lot for your priceless help when fixing "small" problems in the Water Tunnel. Whenever a modification was necessary in the Water Tunnel for a new experiment, we thought about possible solutions, and then we went to you to discuss our "brilliant" ideas. Quite often you suggested a cleverer and neater solution.

I also thank Bas for arranging new PCs for the lab when needed and for taking care of the PTV-PIV cluster in the Teehuis, which many times gave us troubles.

Joanita thank you for the immense help you always provide to the group. Especially for PhD students coming from abroad, because you make our initial phase in The Netherlands much easier by arranging paperwork, appointments and even housing. Vox populi: without the four of you the group could not work at all!

To the scientific staff: Devaraj, Michel, Leen, Jacco. Finally, to all (ex)POF members: my old officemates (Francisco, Arjan, Jos) and the virtual ones (Dennis, Sander, Richard). To Aaldert, Álvaro, Bram, Ceyda, Claas, Christian, Daniela, Dennis Bakhuis, Elena, Erik, James, Jeroun, Joost, Koen, Kristjan, Laura, Hanneke, Hrudya, Ivo, Marine, Marlies, Mark-Jan, Oleks, Oscar, Rajaram, Rocío, Rodolfo, Rory, Siddharta, Stefan, Stephan, Tak, Tess, Theo, Tim, Tuan, Vincent, Wim, and all master, and bachelor students. It has been very grateful to work with all of you, to have lunch together, to chat about everything (science included!) and for the many events outside Meander in which we participate!

Casita

To live in Enschede has been wonderful. But to have lived at Usselerweg 116 (a.k.a. the Russian-Indian-Taiwanese-Mexican consulate), it has just been the best!! And this is because of the incredible human beings with whom I have lived: Peichun, Lizita and our-weekend-visitor Roman, and Shilpi.

Peichun thanks for offering refuge to Liza and to me, and will to share the house you got in December 2007. The first months were quite busy until we manage to get it *gezellig*. Thanks also for being a funny and relaxed girl, and for encouraging me to practice yoga. In your last year, most of our talks biased towards the inevitable *what's next?* question. Luckily, you took a good decision. I'll always remember your yummy-yammy muffins.

Lizita, I am proud of you my pupil! Because I introduced you into the art of hot-spicy-salsas, and surprisingly for a Russian you even exceeded my limits in a short time. I promise that every time I visit you, I will bring a bottle of green salsa habanera for your delight. I am also proud about our major decoration achievement at home: the walls at the living room, blank-white-wallpaper minimalism to the maximum!!

After Peichun left, there was a transition period, when our house received a great Japanese couple: Kaoru and Yoshi with whom we also had a good time learning a lot about their country of the rising sun.

Then, Shilpi knocked at the door and everything changed: a happy new spirit at home. Your freshness of a first year PhD student and your vibrating energy helped us (old-third-year-agonizing-students) a lot to relax. Not to forget your Indian input to broaden our culinary taste, flavorful dishes every time you cook. Fortunately, Lizita discovered your secret: *just add coriander!!*

Shilpi, Lizita, Roman, many people agree that the last year of the PhD is the toughest. Indeed, it was for me. But you made me feel as it was not. I have enjoyed to the fullest my time living with you. I will miss you a lot and I will always remember with joy your support, your laughter that make home vivid, our fantastic dinners and parties, our serious or non-sense talks. It will be hard to replace such a family like you!!

Los cuadernos de doble raya

Along these four years I have been lucky enough to meet amazing people. The best part is that I am privileged to count them amongst my friends.

I would like to thank the international community in Meander that I met when I arrived to Rainschede and which made my adaptation process easier: Gabo and Yas, Enrico, Florent and Sandie, Valeria, Benji, Hermano (a.k.a Burak) and Annemirl, Micheline, Rocío, Tío (a.k.a. Álvaro), Helmut and Sylvain. I will remember especially Gabo and Yas wedding in México, where many of you could be present. We had lots of fun together!

Para ese entonces también conocí a jóvenes ilustres latinoamericanos quienes se convertirían en mis mejores amigos: la Eminencia, el Camarada (a.k.a. David), Nayeli y Eduardo, Dani y Oscar. Estimadísimos, gracias por haber estado conmigo en las buenas y en las malas. Gracias por su sólida y franca amistad que ha permanecido a pesar de mis errores. Muchas gracias también a Maylín y a Gaby quienes junto con el Comandante nos alojaron gentilmente en Ciudad Atardeceres (a.k.a. Habana). El tiempo con ustedes en su país fue simplemente inmejorable!!! Y habrá que regresar o ir a México a disfrutar también otra parte de lo mero bueno!! También muchas gracias a toda la banda latina que conocí después: Dana(rezo), Fede, Kike, Chola (a.k.a. Diana), Ricardo, Jealemy, Arturo, Daniel Cara, Jorge, Mayte, Juan Manuel, Diru, Vicky, Lorenzo, Reyes, Nikolay, Laura, Maciek, Kasia, Arturo B. A la bandera en Alemania: Marcos, Efra y Sofi, Karen, Martha, Ernesto, Chamaquita (a.k.a Moni) y a Paty. A todos ustedes gracias por su amistad, por ser parte de mi familia en el exilio, por la diversión conjunta y mejorada, por todas las monumentales y deliciosas cenas, por las rumbas y pachangas, faltaba más!

E agora é tempo de agradecer a uma pessoa muito legal. Garofa, obrigado por ter aparecido no momento certo em Enschede. Obrigado pelo seu grande sorriso de baleia tropical e anjo carioca que faz feliz a gente. Por compartilhar comigo o seu país, ♫ *abençoado por deus e bonito por natureza, mas que beleza* ♫. E tambEm, por ter-me apresentado ou pour a redescoberta do seus amigões: Elis, Cartola, Tim, Vinicius, Antônio, Gilberto, Marisa, Seu Jorge, Maria Bethânia, Jorge Ben, Cassia, mais sobretudo Roberto Carlos.

L.A. Voz

To the proactive and enthusiastic people with whom it was possible to create a Latin American student Association at the UT. Starting this amazing project demanded time and work, but it was rewarding. I enjoyed working and having fun with all of you. To L.A. Voz founders: Andrea, Laura, Nayeli, Jealemy, Dani, Coen, Mario, Joni, Oscar, David, and to the second board for continuing the project: Vicky, Juan Manuel, John, Edson, Ileana.

Chilangos Habaneros

To the members of the most famous latin american band of East Holland. To el Comandante, Oscar, Dani, Mr. Bongo, Kasia, Mauro, Bob, el Tío, Doctor Pana, Edit, Marine, Matteo, the Chilangos Habaneros. It was tons of fun to participate in such a great musical adventure!!!!!

Los de siempre

A mis carnales putativos (a.k.a. Los Ratas). Esa cofradía roedora que se formó en los ya lejanos noventas y que ha ido creciendo con la llegada de las medias naranjas y de los chilpayates. A los gemelos Brenan (a.k.a. Los Amezcua, Rodris y Adris) y a sus respectivas. A Adris, a Hélène, a la peque Agathe y al que viene en camino. A Rodris y a Catia. A Lencho (a.k.a Juan Carlos) y a Christine. Al Capitangas (a.k.a Mauricio) y a Georgia y al peque Stratios. Al Rata mayor (a.k.a. Rogelio) y a Eli. Al Prado (a.k.a Gustavo). Carnales! Gracias por estar siempre ahí, al pie del cañón, disponibles y al tanto a pesar de las distancias. Por todos los Ratatours, hayan sido en las Europas o en Mexicalpan. Arrieros somos y en el camino andamos!!

A Polita, por todo tu apoyo y las terapias gratuitas vía Skype. Por tus libros-regalo que alegremente me acompañaban cada vez que regresaba de Ciudad Monstruo. A Itandehui, por esa rebeldía incólume que tanto te admiro y te respeto.

A Roberto. Por tu amistad, apoyo moral y académico que brindas a todos los estudiantes que tienen o han tenido el privilegio de trabajar contigo. Por tu contribución y tu granote de arena al hacer ciencia en México (mientras conquistamos otros territorios).

Finalmente, quisiera agradecer infinitamente a mi gran familia en México, todos mis tíos, primos, sobrinos. Especialmente a papá, a mamá, a Gaby, a Edgar y al fantástico sobrino que tengo: Matías Dientes-de-leche! Gracias por todo el apoyo que me brindan en cada decisión que tomo. Ustedes son una gran fuerza y energía para mí. Sin ustedes a mi lado este trabajo no hubiera sido posible.

Appendix J...
or the non trustable information

In this appendix, the narcissist author psychoanalyzes himself and narrates past events directly linked to the materialization of this book.

The author was born in 1979 in Ciudad Ombligo de Luna (a.k.a. La Gran Tenochtitlan, Ciudad Monstruo). His first experience with school was shocking, and disappointing, and he cried his first day at the Kindergarten. Thanks to a successful brain wash by his parents he decided to give a second chance to school. After happier experiences in primary and high-school, he enrolled in the National Autonomous University of México (UNAM) where he studied Mechanical Engineering. He did his bachelor research project under the supervision of Prof. Roberto Zenit Camacho and graduated in 2003.

At that time, he thought that going abroad would help him to overcome his Kindergarten shocking experience. In 2004, he obtained a Conacyt-DAAD scholarship, and started a Master in Mechanical Engineering at the Technische Universität München. Again he had a pretty harsh shock. This time culinary. He realized that tacos, hot-spicy salsas and tortillas were not at hand anymore. Nevertheless, he encountered rapidly refuge in Bratwurst, wunderbare Kuchen und durstlöschendes Bier. But this was not enough for a voracious eater like him. Moreover, mama's food could not be easily replaced. Thus in order to cure his sorrows, he undertook an enjoyable onion-chopping-garlic-peeling therapy in the kitchen. For his master project he worked on numerical simulations of high-speed trains at the Deutsche Bahn AG.

In 2007, he started the PhD at the Physics of Fluids Group of Prof. Detlef Lohse in the University of Twente. Besides the great project he would start working on, one further motivation for moving to Enschede was to experience new "confinement" conditions. Having lived in Ciudad Monstruo with a population of $\approx 2.5\times10^7$ people (comparable to a heterogenous out of equilibrium system, with high particle interaction and collision rates), and in München with its $\approx 1.3\times10^6$ people (comparable to a homogeneous middle dense system), he thought that the next logical step would be to move to a city with a factor 10 less people than München. Enschede with its $\approx 1.5\times10^5$ people fit quite well within this trend! Indeed, Enschede, as a very di-

a) Those Kindergarten days; b) Auteur met een belegde broodje; c) The voracious eater in the eighties; d) The voracious eater 26 years later working in a Lab in Drienerlo, Nederland.

lute system, has the optimal tracking conditions for detecting single individuals at the Oude Markt!!

In the Netherlands besides the gastronomical surprises, the North Sea's weather offered him more: long periods of days in which the only thing one can see in the sky are grayish clouds or the fact that spring, summer, fall and winter can be experienced all at once in the same day!! As a consequence, he developed the lizard symptom of sunbathing whenever sun rays made it through the clouds and hit the ground surface, which usually occurs at most 60 days within a year.

After having enjoyed to the maximum his stay in Enschede, the author will continue doing experiments at the Laboratory of Non-linear Daily Research. Finally thanks to all this peregrination, he has overcome the Kindergarten shock ⌣̈!!